Applied Computational Electromagnetics Society

Journal

February 2013

Vol. 28 No. 2

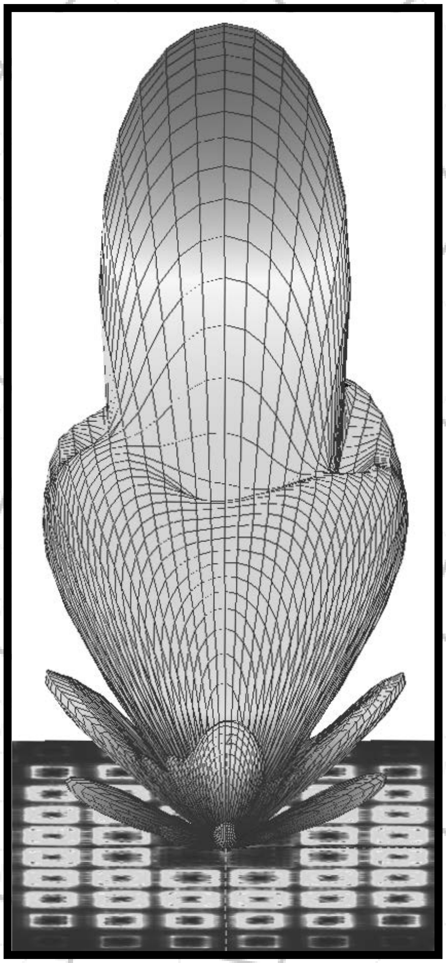

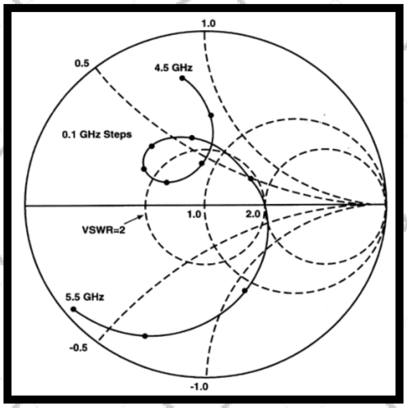

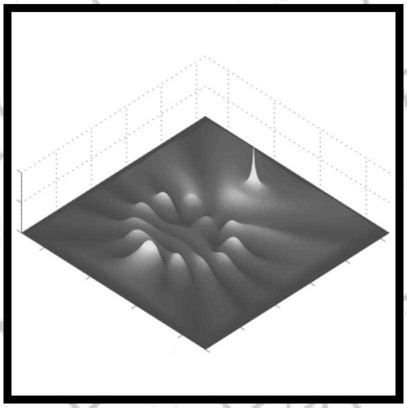

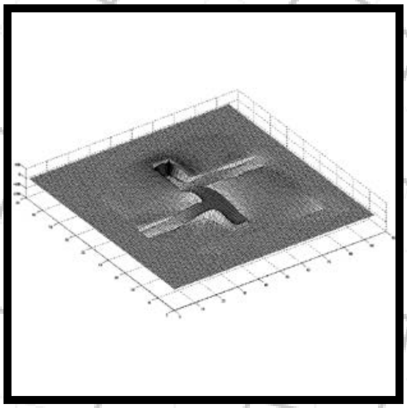

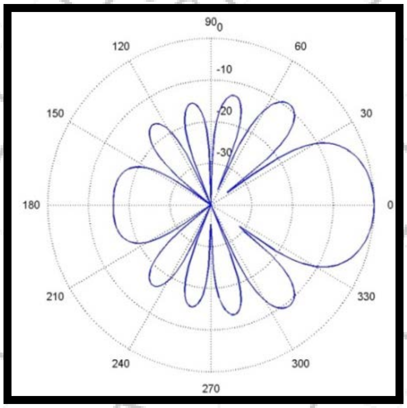

ISSN 1054-4887

GENERAL PURPOSE AND SCOPE: The Applied Computational Electromagnetics Society ***(ACES)*** Journal hereinafter known as the ***ACES Journal*** is devoted to the exchange of information in computational electromagnetics, to the advancement of the state-of-the art, and the promotion of related technical activities. The primary objective of the information exchange is to inform the scientific community on the developments of new computational electromagnetics tools and their use in electrical engineering, physics, or related areas. The technical activities promoted by this publication include code validation, performance analysis, and input/output standardization; code or technique optimization and error minimization; innovations in solution technique or in data input/output; identification of new applications for electromagnetics modeling codes and techniques; integration of computational electromagnetics techniques with new computer architectures; and correlation of computational parameters with physical mechanisms.

SUBMISSIONS: The ***ACES Journal*** welcomes original, previously unpublished papers, relating to applied computational electromagnetics. Typical papers will represent the computational electromagnetics aspects of research in electrical engineering, physics, or related disciplines. However, papers which represent research in applied computational electromagnetics itself are equally acceptable.

Manuscripts are to be submitted through the upload system of ***ACES*** web site http://www.aces-society.org See "Information for Authors" on inside of back cover and at ***ACES*** web site. For additional information contact the Editor-in-Chief:

Dr. Atef Elsherbeni
Department of Electrical Engineering
The University of Mississippi
University, MS 386377 USA
Phone: 662-915-5382
Email: atef@olemiss.edu

SUBSCRIPTIONS: All members of the Applied Computational Electromagnetics Society are entitled to access and download the ***ACES Journal*** any published journal article available at http://aces.ee.olemiss.edu. Printed issues of the ***ACES Journal*** are delivered to institutional members. Each author of published papers receives a printed issue of the ***ACES Journal*** in which the paper is published.

Back issues, when available, are $50 each. Subscription to ***ACES*** is through the web site. Orders for back issues of the ***ACES Journal*** and change of address requests should be sent directly to ***ACES*** office at:

Department of Electrical Engineering
The University of Mississippi
University, MS 386377 USA
Phone: 662-915-7231
Email: aglisson@olemiss.edu

Allow four weeks advance notice for change of address. Claims for missing issues will not be honored because of insufficient notice, or address change, or loss in the mail unless the ***ACES*** office is notified within 60 days for USA and Canadian subscribers, or 90 days for subscribers in other countries, from the last day of the month of publication. For information regarding reprints of individual papers or other materials, see "Information for Authors".

LIABILITY. Neither ***ACES***, nor the ***ACES Journal*** editors, are responsible for any consequence of misinformation or claims, express or implied, in any published material in an ***ACES Journal*** issue. This also applies to advertising, for which only camera-ready copies are accepted. Authors are responsible for information contained in their papers. If any material submitted for publication includes material which has already been published elsewhere, it is the author's responsibility to obtain written permission to reproduce such material.

APPLIED COMPUTATIONAL ELECTROMAGNETICS SOCIETY JOURNAL

February 2013
Vol. 28 No. 2
ISSN 1054-4887

The ACES Journal is abstracted in INSPEC, in Engineering Index, DTIC, Science Citation Index Expanded, the Research Alert, and to Current Contents/Engineering, Computing & Technology.

The illustrations on the front cover have been obtained from the research groups at the Department of Electrical Engineering, The University of Mississippi.

THE APPLIED COMPUTATIONAL ELECTROMAGNETICS SOCIETY
http://aces.ee.olemiss.edu

EDITOR-IN-CHIEF

Atef Elsherbeni
University of Mississippi, EE Dept.
University, MS 38677, USA

ASSOCIATE EDITORS-IN-CHIEF

Sami Barmada
University of Pisa. EE Dept.
Pisa, Italy, 56126

Fan Yang
University of Mississippi, EE Dept.
University, MS 38677, USA

Mohamed Bakr
McMaster University, ECE Dept.
Hamilton, ON, L8S 4K1, Canada

Yasushi Kanai
Niigata Inst. of Technology
Kashiwazaki, Japan

Mohammed Hadi
Kuwait University, EE Dept.
Safat, Kuwait

Mohamed Abouzahra
MIT Lincoln Laboratory
Lexington, MA, USA

Alistair Duffy
De Montfort University
Leicester, UK

EDITORIAL ASSISTANTS

Matthew J. Inman
University of Mississippi, EE Dept.
University, MS 38677, USA

Anne Graham
University of Mississippi, EE Dept.
University, MS 38677, USA

EMERITUS EDITORS-IN-CHIEF

Duncan C. Baker
EE Dept. U. of Pretoria
0002 Pretoria, South Africa

Allen Glisson
University of Mississippi, EE Dept.
University, MS 38677, USA

David E. Stein
USAF Scientific Advisory Board
Washington, DC 20330, USA

Robert M. Bevensee
Box 812
Alamo, CA 94507-0516, USA

Ahmed Kishk
University of Mississippi, EE Dept.
University, MS 38677, USA

EMERITUS ASSOCIATE EDITORS-IN-CHIEF

Alexander Yakovlev
University of Mississippi, EE Dept.
University, MS 38677, USA

Erdem Topsakal
Mississippi State University, EE Dept.
Mississippi State, MS 39762, USA

EMERITUS EDITORIAL ASSISTANTS

Khaled ElMaghoub
University of Mississippi, EE Dept.
University, MS 38677, USA

Mohamed Al Sharkawy
Arab Academy for Science and
Technology, ECE Dept.
Alexandria, Egypt

Christina Bonnington
University of Mississippi, EE Dept.
University, MS 38677, USA

FEBRUARY 2013 REVIEWERS

Ahmed Abdelrahman
Giovanni Angiulli
Marco Arjona
Manuel Arrebola
Kabir Ashraf
Mohamed Bakr
M. do Rosário Calado
Fangyuan Chen
Danesh Daroui
Darko Kajfez
Yasushi Kanai
Mun Soo Lee
Payam Nayeri
Nasser Ojaroudi
Kurt Oughstun
Eesa Rahimi
Edward Rothwell
António Espírito Santo
Hossein Torkaman
Haogang Wang
Quanquan Wang
John Young
Okan Yucedag
Faiza Zafar
Hua Zeng
Ruiqiang Zhang

THE APPLIED COMPUTATIONAL ELECTROMAGNETICS SOCIETY

JOURNAL

Vol. 28 No. 2 February 2013

TABLE OF CONTENTS

Selecting Sampling Interval in the Improved Spectral Domain Method to Simulate Microstrip Circuits

Zhuqian Gong[1], Raj Mittra[2], Wenhua Yu[2], Xiaoling Yang[2], and Jianyan Guo[3]

[1] School of Information Science & Technology,
Sun Yat-sen University, Guangzhou 510006, China
gongchibi@163.com

[2] Electromagnetic Communication Laboratory,
Pennsylvania State University, University Park, PA 16802, USA
mittra@engr.psu.edu, wenyu@2comu.com, and xuy3@psu.edu

[3] Electronic and Electrical Engineering Department,
Xiamen University of Technology, Xiamen 361005, P.R.China,
guonetmail@163.com

Abstract **─** In this paper, we investigate the spectral method that calculates the S-parameters for microstrip circuits and antennas. A sampling interval selection criterion is proposed. The scheme for low-loss cases is specially discussed. Several examples are employed to demonstrate the engineering applications of the spectral domain method and its results are compared with previously published and measured results.

Index Terms - Microstrip circuits, sampling interval, and spectral domain method.

I. INTRODUCTION

The time domain Prony's method [1, 2] and its improved version [3] have been proposed to derive complex resonant frequencies of a scatterer from its transient response. The optimum sampling technique for the original time domain Prony's method has been presented in [4] and the issue of choosing the sampling interval for the improved time domain Prony's method has been addressed in [5]. A combination of FDTD and time domain Prony's methods [6] have been employed for the analysis of microwave integrated circuits and to obtain their scattering parameters. The concept of spectral domain Prony's method has been introduced in [7], and has been applied to the problem of analyzing planar microstrip circuits. It employs the least squares procedure to estimate the complex scattering parameters. It does this by extracting the magnitude and phase of the incident and reflection waves from the sampled voltage data, and it does not require the knowledge of the characteristic impedance of the microstrip feed line. However, if the dimensions of microstrip lines at the feed and load ends are relatively small, then the distance between the sampling points to which the Prony's method is applied is small. Under these circumstances, the conventional spectral domain Prony's method suffers from the problem of ill-conditioned equations whose solution has considerable errors, especially at low frequency. We have introduced its improved version in [8] to circumvent this problem. The improved version has higher accuracy and smaller computational domain compared with the conventional spectral domain Prony's method, and is in good agreement with analytic formula as well as measured data. In this work we propose the sampling interval selection criterion based on error analysis and numerical experiments. Further, this method cannot get physical attenuation for low-loss cases, but it can get good results for S-parameters. We will demonstrate this point in the following sections and propose a special scheme for lossy cases.

Submitted On: Apr. 10, 2012
Accepted On: Jan. 16, 2013

II. SPECTRAL-DOMAIN PRONY METHOD

The sampled values of the complex voltage at the feed end of the microwave circuit can be given by [7]

$$V_n = A_1 z_1^n + A_2 z_2^n, \qquad n = 0,1,\cdots,N-1, \quad (1)$$

where both A_1 and A_2 are complex unknowns, as yet undetermined, and

$$z_1 = e^{-\gamma d}, \;\; z_2 = e^{\gamma d}, \quad (2)$$

where γ (γ=α+jβ) is the complex wave number, and *d* is the sampling interval along the microstrip transmission line. In equation (1), V_n are obtained from the time domain data at *N* equally spaced nodes via Fourier transformation.

It is assumed that z_1 and z_2 are the roots of the algebraic equation

$$B_2 + B_1 z - z^2 = 0. \quad (3)$$

From equations (1) and (3), one can obtain

$$\begin{bmatrix} V_1 & V_0 \\ V_2 & V_1 \\ \vdots & \vdots \\ V_{N-1} & V_{N-2} \end{bmatrix} \begin{bmatrix} B_1 \\ B_2 \end{bmatrix} = \begin{bmatrix} V_2 \\ V_3 \\ \vdots \\ V_N \end{bmatrix}. \quad (4)$$

Using the least squares procedure, the original spectral domain Prony's method solves equations (4), (3) and (1) to get A_1 and A_2 i.e., the incident and reflection voltages, and knowledge of which one can calculate all of the entries of the scattering matrix.

An improved method has been presented in [8]. From equations (2), (3) and (4), we have

$$\begin{bmatrix} V_1 \\ V_2 \\ \vdots \\ V_{N-1} \end{bmatrix} \left[e^{\gamma d} + e^{-\gamma d} \right] = \begin{bmatrix} V_2 + V_0 \\ V_3 + V_1 \\ \vdots \\ V_N + V_{N-2} \end{bmatrix}. \quad (5)$$

Numerical simulations show that solving the above matrix cannot get physical attenuation constant for small loss cases. Considering that loss is generally low and sampling interval is very small (generally 0.01 mm ~ 2 mm), even if we set α = 0, we can get good results of scattering parameters. When it is very lossy, we still use the above matrix.

For a lossless line, the matrix shown in equation (5) reduces to

$$\begin{bmatrix} Re\begin{pmatrix} V_1 \\ V_2 \\ \vdots \\ V_{N-1} \end{pmatrix} \\ Im\begin{pmatrix} V_1 \\ V_2 \\ \vdots \\ V_{N-1} \end{pmatrix} \end{bmatrix} 2\cos(\beta d) = \begin{bmatrix} Re\begin{pmatrix} V_2 + V_0 \\ V_3 + V_1 \\ \vdots \\ V_N + V_{N-2} \end{pmatrix} \\ Im\begin{pmatrix} V_2 + V_0 \\ V_3 + V_1 \\ \vdots \\ V_N + V_{N-2} \end{pmatrix} \end{bmatrix}, \quad (6)$$

where *Re* (•) and *Im* (•) imply the real and the imaginary parts, respectively. We derive *β* from these above equations. It is evident that the values of thus obtained, have numerical artifacts and, hence, we fit the computed values with a straight line passing through the origin. This is due to the fact that *β* is proportional to the frequency *f*

$$\beta = \frac{2\pi\sqrt{\varepsilon_e}}{c} f, \quad (7)$$

where ε_e is the effective dielectric constant and *c* is the speed of light in free space. Then, the improved method leads to S-parameters that are much more reasonable and physically acceptable than the original results. A more accurate approach for solving *α* and *β* is to introduce analytic solution of *α* and *β*. For a microstrip line, the phase constant can be written as shown in equation (7), and the attenuations due to dielectric loss and due to conductor loss can be given by [9],

$$\alpha_d = \frac{k_0 \varepsilon_r (\varepsilon_e - 1)\tan\psi}{2\sqrt{\varepsilon_e}(\varepsilon_r - 1)} \quad (8)$$

$$\alpha_c = \frac{R_s}{Z_0 W}, \quad (9)$$

where k_0 is the free space wave number, tanψ is the loss tangent of the dielectric, R_s is the surface resistivity of the conductor, *W* is the width of the microstrip line, Z_0 is the characteristic impedance of the feeding transmission line whose expression is also given in [9]. For coplanar waveguides, its attenuation has been analyzed in [10-14]. In fact, for these cases as well as other complex problems [15-17], it is very complicated to calculate their phase and attenuation constant. So, we solve equation (5) for very lossy cases and equation (6) for lossless and low loss cases. We subsequently solve equation (1) to get incident and reflection voltages and then calculate the S-parameters.

III. SAMPLING INTERVAL

There are several popular excitation techniques in FDTD simulations: lumped port, wave port, mode port, aperture field, and plane wave source [18]. The difference of the wave port from the lumped port is that the wave port is used to excite a matched port and the lumped port is used to excite an open port. Since the feed line is terminated at the domain boundary, it is perfectly matched at the domain boundary. We then use wave port excitation, not lumped port excitation. Another suitable excitation source for uniform transmission lines is a mode port [18, 19]. For solving and storing modal field, it needs more memory and computational time than wave port.

Theoretically, we choose d to be as large as possible to improve the property of equation (1). Unfortunately, if d is too large, the computational cost will greatly rise. Consequently, there is an optimal choice for the sampling interval that balances computational cost in the FDTD method and numerical error in the spectral domain method. To derive the selecting criterion of sampling interval, we firstly define a function $y = f(x)$ plotted in Fig. 1. As shown in this figure, the same error ± Δy has different confidence intervals, and with large gradient comes small interval, in which it has higher probability to obtain the exact solution. From equation (6), we approximately have

$$d\sin(\beta d)\Delta\beta = \delta, \tag{10}$$

where δ is the relative numerical error of the sample data. The relative error depends on a number of factors such as the cell-size in the FDTD method, and the structure of microstrip circuit. If we want to get a reasonable β, the sampling interval d must satisfy

$$(\beta d)^2 > \delta \ . \tag{11}$$

Numerical simulations for the band pass filter with wave port cases indicate that the suitable sampling interval approximately satisfies

$$d > \frac{0.01}{\beta_{\min}} \ . \tag{12}$$

One can also get good results if selecting such sampling interval for simple microstrip circuits as the patch antenna and low pass filter given in [20]. Although being an approximation, the above expression provides a selecting criterion that has not been presented before. Note that the sampling interval should be larger than the minimum cell size of the FDTD simulation.

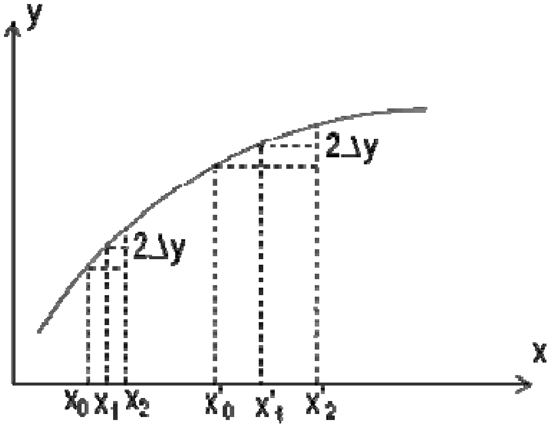

Fig. 1. Relationship between interval and gradient with the same error.

IV. EXAMPLE

We now use the spectral domain method to simulate a microstrip patch antenna, whose actual dimensions are shown in Fig. 2. The relative permittivity of the substrate is 2.2 and the conductivity of the patch and feed line is 5.8 × 10^8 S/m. We get the conductor loss by the use of equation (9), which is plotted in Fig. 3 (a). The computational domain for this problem is 25 mm × 50 mm × 20 mm and the sampling interval d is equal to 0.5 mm. Since the conductance of the conductor is finite, several cells are needed to simulate the conductors in the z-direction. It is very important to ensure that the FDTD mesh coincides with the edges of the feed line and the patch. We take the minimum cell sizes to be 0.05, 0.05, and 0.01 mm, in the x-, y-, and z-directions, respectively. Thus a non uniform mesh of (225 × 320 × 261 cells) is generated including six-layers of PML. A wave port is employed as an excitation source. To calculate the S-parameters, we use these three approaches as follows:

i. using equation (5) and set $\alpha = 0$, then fitting β,
ii. using equation (6) and fitting β,
iii. using analytic α and β from equations (8) and (9).

The numerical results of the attenuation constant are shown in Fig. 3 (b). We then plot its magnitude in Fig. 4. Moreover, the results of the phase constants are shown in Fig. 5. From the example, we conclude that it is difficult to solve the attenuation constant for the present spectral domain, although the method can get good results for the scattering parameters. As mentioned above, if the sampling distance is large enough, the current method can get good result of attenuation constant, but it will significantly add computational domain and require more memory. Using the current method, we can get good results for the S-parameters even though we cannot get physical attenuation for low-loss cases in the case of small sampling interval.

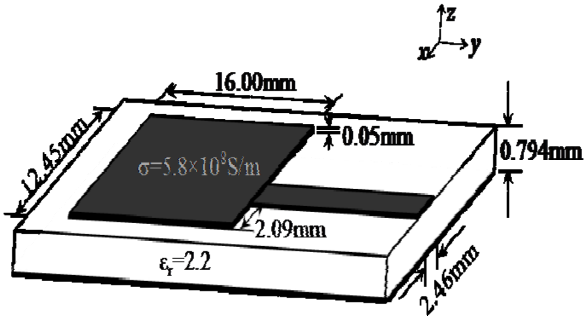

Fig. 2. Microstrip patch antenna.

Finally, we study a microstrip branch line coupler with four ports. The substrate relative permittivity is 2.2. The dimensions of the branch line coupler are given in [19] and repeated here in Fig. 6. The computation domain is 50 mm × 20 mm × 3 mm, in the x-, y-, and z-directions, respectively. The minimum spaced steps used are $\Delta x = 0.5$ mm, $\Delta y = 0.38675$ mm, and $\Delta z = 0.2$ mm and the non-uniform mesh is 85 × 47 × 13 cells, which is relatively small for a single PC. The corresponding time step is approximately 0.532 ps. The sampling interval is 0.5 mm and a wave port is employed to excite port 1. The computation time for this circuit is approximately only one minute on a single PC with two cores and 6 GB memory. It is a lossless case, so we use equation (6) to get the phase constant and plot it and its fitting curve shown in Fig. 7. The scattering coefficient results, as shown in Fig. 8, indicate good agreement in the location of the response nulls and crossover point. The desired branch line coupler performance is seen in the sharp S_{11} and S_{21} nulls, which occur at approximately at the same frequency as the crossover in S_{11} and S_{21}. At this point S_{31} and S_{41} are both approximately -3 dB, indicating that almost all of the power from port 1 is equally divided and transmitted through the device to ports 3 and 4.

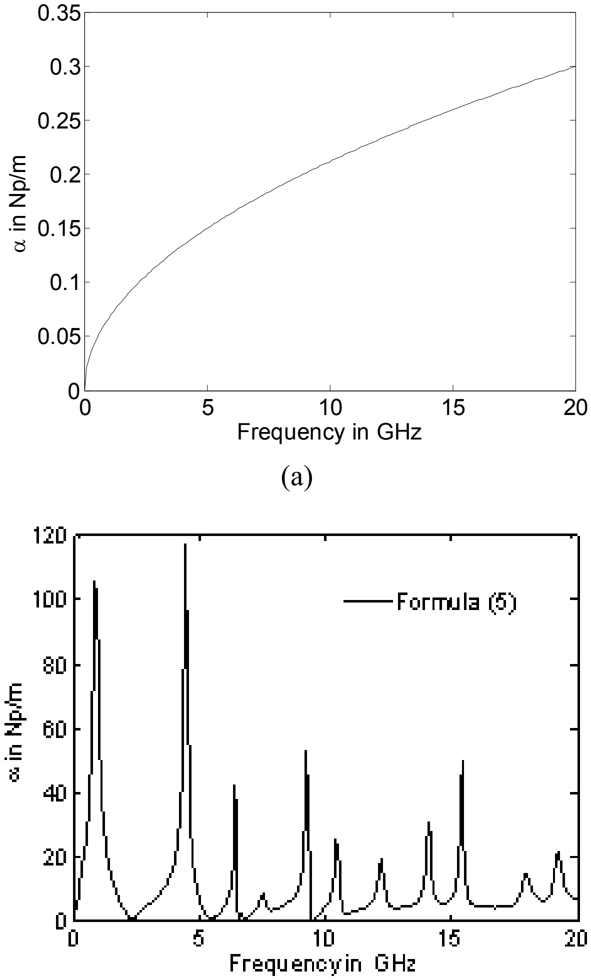

(a)

(b)

Fig. 3. Attenuation constant versus frequency for (a) analytic solution and (b) using equation (5).

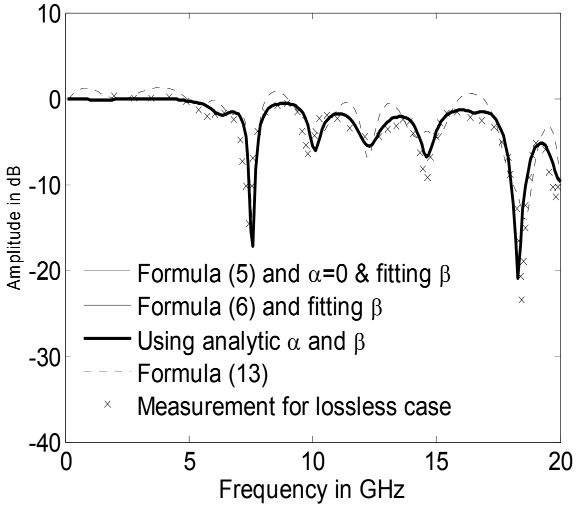

Fig. 4. Magnitude of S_{11} versus frequency.

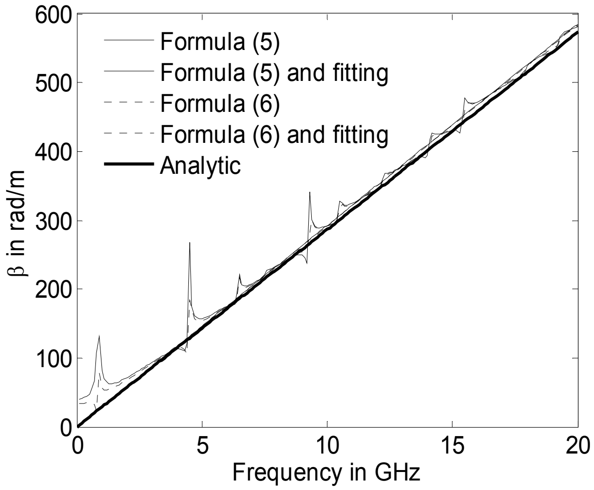

Fig. 5. Phase constant versus frequency.

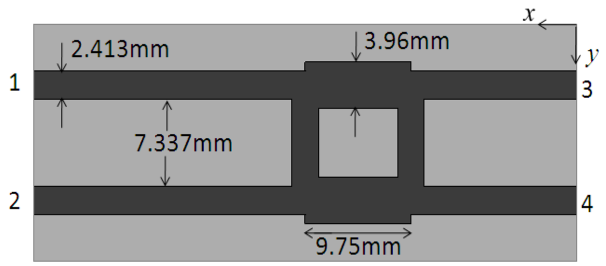

(a) Top view

(b) Side view

Fig. 6. Dimensions of the microstrip branch line coupler.

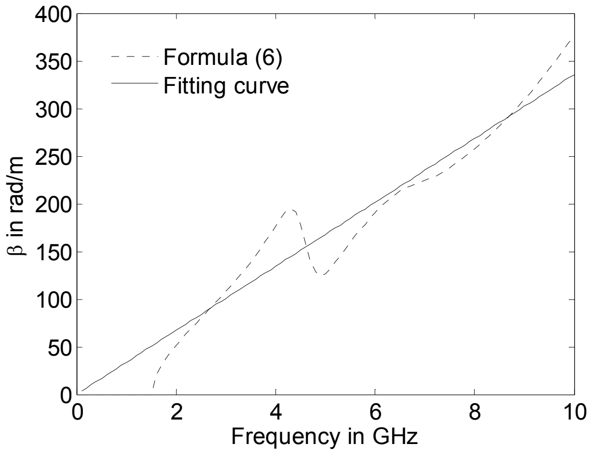

Fig. 7. The computational results of the phase constant and its fitting curve.

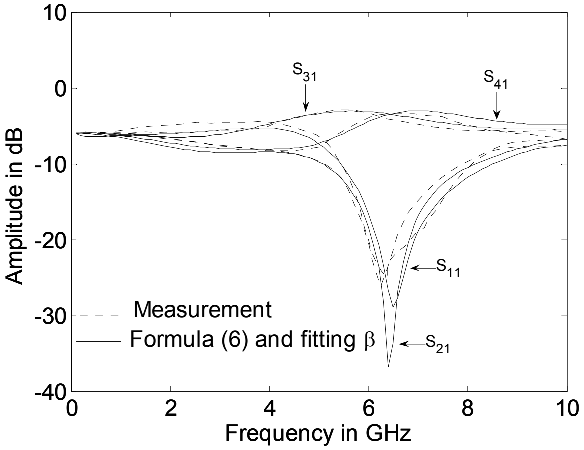

Fig. 8. Scattering parameters of the branch line coupler.

V. CONCLUSION

We have investigated the improved spectral domain method for the computation of scattering parameters of microstrip circuits. An empirical formula has been proposed for selecting a suitable sampling distance of the total voltages along the feed line. Moreover, we have also presented three approaches to analyze the lossy cases in spectral domain, and found that lossy problems can be processed as lossless cases in the present method. Using the current method, we can still get good results for S-parameters even though we cannot get physical attenuation for low-loss cases in the case of small sampling interval.

REFERENCES

[1] M. L. Van Blaricum and R. Mittra, "A technique for extracting the poles and residues of a system directly from its transient response," *IEEE Trans. Antennas Propagat.*, vol. Ap-23, pp. 777-781, Nov. 1975.

[2] J. A. Pereda, L. A. Vielva, A. Vegas, and A. Prieto, "Computation of resonant frequencies and quality factors of open dielectric resonators by a combination of the finite-difference time-domain (FDTD) and Prony's methods," *IEEE Microwave and Guided wave Letters*, vol. 2, pp. 431-433, Nov. 1992.

[3] A. J. Mackay and A. McCowen, "An improved pencil-of-function method and comparisons with traditional methods of pole extraction," *IEEE Trans. Antennas Propagat.*, vol. Ap-35, pp. 435-441, April 1987.

[4] R. W. Kulp, "An optimum sampling procedure for use with the Prony method," *IEEE Trans.*

Electromag. Compat. vol. EMC-23, pp. 67-71, May 1981.

[5] J. Lee and H. Kim, "Selecting sampling interval of transient response for the improve Prony method," *IEEE Trans. Antennas Propagat.*, vol. Ap-51, pp. 74-77, Jan. 2003.

[6] W. L. Ko and R. Mittra, "A combination of FDTD and Prony's methods for analyzing microwave integrated circuits," *IEEE Trans. Microwave Theory and Techniques*, vol. 39, pp. 2176-2181, Dec. 1991.

[7] K. Naishadham and X. P. Lin, "Application of spectral domain Prony's method to the FDTD analysis of planar microstrip circuits," *IEEE Trans. Microwave Theory and Techniques*, vol. 42, pp. 2391-2398, Dec. 1994.

[8] Z. Gong, W. Yu, and X. Yang, "Improvements to spectral domain Prony's method for analyzing microstrip circuits," *Electronics Letters*, vol. 47, no. 5, pp. 330-331, March 2011.

[9] D. M. Pozar, *Microwave Engineering, 2nd Ed.*, John Wiley & Sons Inc., New Jersey, 1998.

[10] R. N. Simons, *Coplanar Waveguide Circuits, Components, And Systems*, John Wiley & Sons Inc., New Jersey, 2001.

[11] R. E. Collin, *Foundations For Microwave Engineering, 2nd Ed.*, Wiley-IEEE Press, New Jersey, Dec. 2000.

[12] K. C. Gupta, R. Garg, I. Bahl, and P. Bhartia, *Microstrip Lines and Slotlines, 2nd Ed.*, Artech House Inc., Norwood, MA, 1996.

[13] F. D. Paolo, *Networks And Devices Using Planar Transmission Lines*, CRC Press LLC, Boca Raton, FL, 2000.

[14] M. Fujii and S. Kobayashi, "Accurate analysis of losses in waveguide structures by compact two-dimensional FDTD method combined with autoregressive signal analysis," *IEEE Trans. Microwave Theory and Techniques*, vol. 44, pp. 970-975, June 1996.

[15] H. Chen, Y.-H. Wu, Y.-M. Yang, and Y.-X. Zhang, "A novel and compact bandstop filter with folded microstrip/CPW hybrid structure," *J. of Electromagn. Waves and Appl.*, vol. 24, pp. 103-112, 2010.

[16] A. Hussain and Q. A. Naqvi, "Fractional rectangular impedance waveguide," *Progress In Electromagnetics Research,* PIER 96, pp. 101-116, 2009.

[17] T. Vaupel, "A fast spectral domain solver for the characterization of larger microwave structures in multilayered environments," *Appl. Comp. Electro. Soc. (ACES) Journal*, vol. 24, no. 5, pp. 493-503, Oct. 2009.

[18] W. Yu, X. Yang, Y. Liu, and R. Mittra, *Electromagnetic Simulation Techniques Based on the FDTD Method*, John Wiley & Sons Inc., New Jersey, 2009.

[19] W. Yu, R. Mittra, Y. Liu, and X. Yang, *Parallel Finite-Difference Time-Domain Method*, Artech House Inc., Norwood, MA, 2006.

[20] D. M. Sheen, S. M. Ali, M. D. Abouzahra, and J. A. Kong, "Application of the three-dimensional finite-difference time-domain method to the analysis of planar microstrip circuits," *IEEE Trans. Microwave Theory and Techniques*, vol. 38, pp. 849-857, July 1990.

A Closed-Form Spatial Green's Function for the Thick Microstrip Substrate: The Meshless Interpolation Approach

B. Honarbakhsh[1] **and A. Tavakoli** [2]

[1] Department of Electrical Engineering
Amirkabir University of Technology (Tehran Polytechnic), Tehran, IRAN
b_honarbakhsh@aut.ac.ir

[2] Institute of Communications Technology and Applied Electromagnetics
Amirkabir University of Technology (Tehran Polytechnic), Tehran, IRAN
tavakoli@aut.ac.ir

Abstract **─** In this paper the Green's functions (GFs) of a thick microstrip in the spatial-domain is computed based on expanding the corresponding spectral-domain functions over inverse quadric (IQ) radial basis functions (RBFs). The scattered data interpolation ability of RBFs is exploited for efficient sampling of the Sommerfeld integration path (SIP), passing from close vicinity of singularities in the complex k_ρ plane. By this, the information content of spectral-domain GFs is preserved, which makes it possible to compute the far-fields accurately. Thus, the method can be applied to the analysis of electrically large structures near layered media. The proposed method is direct with only one approximation level.

Index Terms - Microstrip, integral equation, IQ, RBF, and Sommerfeld integral.

I. INTRODUCTION

Development of integral equation (IE)-based methods, was a revolutionary step in the growth of computational electromagnetics (CEM). The most obvious advantage of IE solvers over PDE solvers is to decrease the amount of discretization region, which is limited only to the body under study in the former case. This removes the need of IE solvers to absorbing boundary conditions (ABCs), which is a troubling requirement of PDE counterparts [1, 2]. There also exists a rather not obvious priority for IE solvers, which if not dismissed, is not sufficiently highlighted in the literature; i.e., *the unambiguous description of the problem at its edges and corners*. To clarify this issue, consider electromagnetic (EM) scattering from a PEC plate. Handling this problem by the Finite Element Method (FEM) requires determination of boundary conditions at interior region of the plate, its edges and corners. Although for the interior region, the tangential components of the electric field are known to be zero, the exact condition on EM fields is unknown on rest of the boundary. What is known is its order of singularity [3]. On the other hand, solving the same problem by MoM is straightforward noting that at the edges, the normal component of current and at the corners, the total current should vanish [4].

Beside the aforementioned benefits, there are two challenges dealing with IE solvers. The first is the knowledge of the Green's function (GF) of the problem, which is known for limited cases such as free space, half-space, and multi-layered media [5]. The second challenge is computing the layered media GF in the spatial-domain, which requires numerical evaluation of an inverse Fourier-Bessel transform (IFBT) and follows four difficulties. First, the spectral-domain GFs are multi-valued, having number of branch point singularities and their corresponding branch cuts. Second, these functions have number of pole singularities, leading to abrupt changes. It is important to note that in addition to poles, which intrinsically lead to harsh variations, some of the branch points also lead to such behavior. Third, the Bessel functions

Submitted On: Aug. 20, 2012
Accepted On: Nov. 25, 2012

are oscillatory, which complicates the process of the numerical integration. Fourth, the Bessel functions are slow decaying, which decelerates the computation process, i.e., more sampling is needed, which will lead to longer computation time.

At present, a winning approach to the problem is expanding the spectral-domain GFs over a class of functions with known analytical IFBT. Assuming a successful expansion, all four said difficulties are bypassed. In the recent decades, lots of research is done based on this idea, e.g., [6-13]. These methods can be classified from the following aspects:

A. Expansion function

Up to now, the most used expansion functions are complex exponentials [6, 7, 10], rational [8, 11] and Gaussian functions [13], in either of k_{z0} or k_ρ complex planes, defined in [6]. These planes can be uniquely mapped on each other. The corresponding integrals are then analytically computed via available mathematical identities, e.g., the Sommerfeld Identity (SI) [5], or by the residue theorem [14].

B. Expansion method

Expanding a known function over a class of functions with unknown parameters can be studied under the context of model-based parameter estimation (MBPE). The MBPE can be carried out by non-linear programming or optimization methods. However, there exist conditions which allow solving non-linear problems by linear algebra, e.g., the Prony method [15], generalized pencil-of-function (GPOF) method [16] and matrix-pencil method (MPM) [17]. These methods are all one-step solutions to the expansion problem and expand a complex valued function of a real variable over sum of complex exponentials, provided that the independent variable is sampled uniformly. For expanding over rational functions, the rational function fitting method (RFFM) has currently attracted the researchers [18]. This method is iterative and should be initialized properly.

C. Dependence on human labour

Achieving fully automatic IE solver requires direct methods for computation of spatial-domain GFs. By direct method, it is meant methods independent of human labour, e.g., [7, 10]. In the pioneering works, e.g. [6], the contributions of quasi dynamic images and surface-wave poles (SWPs) were subtracted, analytically. It should be noted that for a general multilayered case, the surface-wave terms cannot be obtained analytically [10].

D. Integration path

Another distinguishing factor is the integration path, which is called the Sommerfeld integration path (SIP). The SIP can be considered in either of the k_{z0} or k_ρ complex planes. Theoretically, all valid paths are equivalent. However, as clearly stated in [10], the limited number of significant digits in numerical computations leads to different results from different paths. The information content of the evaluated GFs increases as the path become closer to singular points. Thus, if the expansion method is incapable of tracking abrupt changes, the path should pass sufficiently far from singularities. Stating another way, there is a compromise between the sharpness of the function and its information content. Such a decrease, leads to erroneous evaluations in the far-field region of the spatial-domain GFs.

E. Number of approximation levels

The variation rate of the spectral-domain GFs differs on different sections of the SIP. Therefore, if the expansion method requires uniform sampling, the efficiency of the process decreases drastically. This fact should specially be considered when direct methods are of interest. A classical solution to this problem is partitioning the integration path to sub-sections and sample each of them independently, based on the behavior of the corresponding spectral-domain GF. The number of approximation levels is then equal to the number of partitions. This procedure is utilized in [7] for the first time, leading to a two-level approximation, and is still followed by other researchers.

F. Physical compatibility

Different sections of the SIP correspond to EM waves of different nature. Thus, it seems reasonable to expand each part such that its IFBT coincides with the real nature of the wave. For instance, the EM wave at the near-field and the far-field along the substrate becomes spherical and cylindrical, respectively. Consequently, physical compatibility is met by expanding the low and high spatial frequency sections of the path such that their IFBT lead to $e^{-jk_0 r}/r$ and $H_0^{(1)}\left(k_0\rho\right)$, respectively, as is done in [11]. Nevertheless, for a successful result, such a compatibility is not necessary [10].

The proposed method employs inverse quadric (IQ) and radial basis functions (RBFs) for expansion, which are rational [19]. The RBFs are mainly constructed for scattered data interpolations [20] and are currently exploited in mesh free solution of operator equations [21, 22]. Expanding over RBFs is done by solving a linear system of equations. Therefore, the expansion process is carried out in one-step, without the need to initial guess. The proposed method is direct and does not need any human labor. Moreover, the extreme ability of RBFs in data fitting makes it possible to pass the SIP from vicinity of singularities. As a result, the method is capable to correctly evaluate the spatial-domain GFs in the far-field region, due to preserving the information content of the spectral-domain GFs. Thus, the method is applicable for the analysis of electrically large structures near layered media. The scattered data interpolation property of RBFs is utilized for non-uniform sampling of the SIP, leading to one-level approximation and significant increase in computational efficiency. Finally, the method does not possess physical compatibility, due to expressing the EM field by cylindrical waves in the whole spatial range.

II. MATHEMATICAL STATEMENT OF THE PROBLEM

Suppose an infinite grounded dielectric substrate with height h and real electric permittivity of ε_r. The substrate is placed on x-y plane such that its top side coincides with $z = 0$. This structure is illuminated by an x-directed electric dipole of unit strength located at $z = z' \geq 0$ and oscillating at frequency $f = f_0$. It is assumed that $z \geq 0$ is free space. Under these assumptions, the spatial-domain GFs in the air region can be computed by [6]

$$\begin{cases} G_A^{xx} = \dfrac{\mu_0}{4\pi}\dfrac{e^{-jk_0 r_0}}{r_0} + \dfrac{\mu_0}{4\pi} F\left(R_{TE}\right) \\ G_q = \dfrac{1}{4\pi\varepsilon_0}\dfrac{e^{-jk_0 r_0}}{r_0} + \dfrac{1}{4\pi\varepsilon_0} F\left(R_{TE} + R_q\right) \end{cases}, \tag{1}$$

with

$$F\left(\cdot\right) = \int_{\text{SIP}} \left(\cdot\right) \frac{e^{-jk_0\left(z+z'\right)}}{jk_{z0}} J_0\left(k_\rho \rho\right) k_\rho dk_\rho, \tag{2}$$

where J_0 is the zero order Bessel function, and

$$\begin{cases} R_{TE} = -\dfrac{r_{10}^{TE} + \Phi}{1 + r_{10}^{TE}\Phi} \\ R_q = \dfrac{2k_{z0}^2\left(1-\varepsilon_r\right)\left(1-\Phi^2\right)}{\left(k_{z1}+k_{z0}\right)\left(k_{z1}+\varepsilon_r k_{z0}\right)\left(1+r_{10}^{TE}\Phi\right)\left(1-r_{10}^{TM}\Phi\right)} \end{cases}, \tag{3}$$

with,

$$\begin{cases} r_{10}^{TE} = \left(k_{z1}-k_{z0}\right)\left(k_{z1}+k_{z0}\right)^{-1} \\ r_{10}^{TM} = \left(k_{z1}-\varepsilon_r k_{z0}\right)\left(k_{z1}+\varepsilon_r k_{z0}\right)^{-1} \\ k_{z0}^2 + k_\rho^2 = k_0^2 \\ k_{z1}^2 + k_\rho^2 = \varepsilon_r k_0^2 \\ \Phi = \exp\left(-j2k_{z1}h\right) \end{cases}. \tag{4}$$

Traditionally, equation (2) is called the Sommerfeld integral. From the mathematical stand point, equation (2) is an IFBT and SIP coincide the real axis in k_ρ plane, not passing from poles and branch points [23]. Exclusion of singularities can be theoretically carried out by turning over them with hemi-circles of infinitely small radii such that the path remains in first and third quadrants to satisfy the Sommerfeld radiation condition [5, 23]. Therefore, the integrand remains analytic on the deformed path. It should be noted that the path deformation theorem ensures invariance of the integral [6, 14].

III. MESHLESS INTERPOLATION BY IQ RBF

Consider the problem of interpolating a function u based on its N scattered samples. The samples are assumed to be laid on the real axis, positioned at $x_1, \ldots, x_N$, and u is in general, complex valued. Currently, the most famous way for achieving this goal is exploiting RBFs. The RBFs are either global support (GS) or compact support (CS) [22]. There is a fundamental difference between these kinds; the CS RBFs are never analytic whereas it is possible to have analytic GS RBFs.

As a brief description of the proposed method, we intend to evaluate contour integrations over the complex k_ρ-plane where the integrand is expanded over RBFs. Thus, CS RBFs are excluded and among GS RBFs, the IQ kind is selected because it is analytic, all-pole, and has a well-conditioned (practically banded and sparse) moment matrix. For the problem at hand, IQ RBF can be expressed as,

$$\varphi(x) = \left(x^2 + A^2\right)^{-1} \tag{5}$$

where A is called the shape parameter [21]. The function u can now be uniquely interpolated at any $x \in [x_1, x_N]$, by the following expansion

$$\begin{cases} u(x) \cong u^h(x) = \sum\limits_{i=1}^{N} w_i \varphi_i(x) \\ \varphi_i(x) = \varphi(x - x_i) = \left[(x - x_i)^2 + A_i^2\right]^{-1} \end{cases}, \tag{6}$$

where u^h is the interpolated value of u. In addition, A_i and w_i are the shape parameter and weighting of the i^{th} sample (node), respectively. The shape parameter can be node dependent. The weightings are simply computed by collocating equation (6) at the nodes and solving a corresponding linear system of equations, which is a well-conditioned diagonal-dominant matrix for the problem at hand.

For determination of the shape parameter, it is preferable to express A_i as,

$$A_i = \alpha_i d_i, \quad \alpha_i > 0 \tag{7}$$

where α_i and d_i are called the dimension less shape parameter and the characteristic length of the i^{th} node, respectively [21]. These parameters are, in general, selected empirically. Unless the distribution of samples is not too irregular, d_i can be selected to be the average nodal spacing [21]. In this work, $\alpha_i = 2$ and $d_i = |x_{i+1} - x_i|$. As a final remark, the IQ RBFs tend to zero outside the sampling region. Thus, if u is practically zero out of $[x_1, x_N]$, u^h can also extrapolate it.

IV. IQ RBF APPROACH TO THE PROBLEM

In this section, the IQ RBF is used for evaluating equation (2). For this purpose, inspiring from [10], we start with the following SIP

$$\text{SIP}_1 : k_\rho = k'_\rho + j\gamma k_0, \quad 0 \le k'_\rho < \infty, \tag{8}$$

where k'_ρ is the real variable of the complex k_ρ plane and γ is a positive factor. Additionally, let's define

$$\begin{cases} R_1 = \dfrac{k_\rho}{jk_{z0}} R_{TE} \cdot e^{-jk_{z0}(z+z')} \\ R_2 = \dfrac{k_\rho}{jk_{z0}} \left(R_{TE} + R_q\right) \cdot e^{-jk_{z0}(z+z')} \end{cases}, \tag{9}$$

which leads to the following equivalent statement of equation (2)

$$F_l(\rho) = \int\limits_{\text{SIP}_1} R_l(k_\rho) \cdot J_0(k_\rho \rho)\, dk_\rho, \quad l = 1, 2. \tag{10}$$

The substrate is assumed to be loss-less. Thus, all the singularities of the spectral-domain GFs lay on the real axis and consequently, this path passes from above of R_1 and R_2 singularities. Moreover, since SIP$_1$ is a biased version of the real axis, the IQ RBF can interpolate the aforementioned functions based on their samples evaluated on this path. Noting the final remark of the previous section, it is necessary to study the behavior of R_1 and R_2 when k_ρ approaches to infinity. It is straightforward to show that

$$\begin{cases} \lim\limits_{k_\rho \to \infty} \operatorname{Re}\{R_1\} = \lim\limits_{k_\rho \to \infty} \operatorname{Im}\{R_1\} = \lim\limits_{k_\rho \to \infty} \operatorname{Im}\{R_2\} \\ \lim\limits_{k_\rho \to \infty} \operatorname{Re}\{R_2\} = (1 - \varepsilon_r)(1 + \varepsilon_r)^{-1} \end{cases}. \tag{11}$$

The above limits can be verified as follows, when $k_\rho \to \infty$, Sommerfeld radiation condition requires $k_{z0} \to -j\infty$ and $k_{z1} \to -j\infty$. Therefore,

$$\begin{cases} \Phi \to 0 \\ r_{10}^{TE} \to 0 \\ r_{10}^{TM} \to (1 - \varepsilon_r)(1 + \varepsilon_r)^{-1} \end{cases}. \tag{12}$$

Consequently,

$$\begin{cases} R_{TE} \to 0 \\ R_q \to (1 - \varepsilon_r)(1 + \varepsilon_r)^{-1} \end{cases}, \tag{13}$$

which noting to equation (9) leads to equation (11). Thus, interpolating R_1 by IQ RBFs will also lead to its extrapolation. This is not the case for R_2. One way to overcome this difficulty is to subtract and add the following function from R_2

$$R_b = (1 + \varepsilon_r)(1 - \varepsilon_r)^{-1} \frac{k_\rho}{\sqrt{k_\rho^2 + \eta^2}}, \quad \eta > 0, \tag{14}$$

and rewriting R_2 as:

$$\begin{cases} R_2 = R_3 + R_b \\ R_3 = R_2 - R_b \end{cases}. \tag{15}$$

The function R_b has the following properties:

$$\begin{cases} \lim\limits_{k_\rho \to \infty} R_b = (1 - \varepsilon_r)(1 + \varepsilon_r)^{-1} \\ \int\limits_{\text{SIP}_1} R_b \cdot J_0(k_\rho \rho)\, dk_\rho = (1 - \varepsilon_r)(1 + \varepsilon_r)^{-1} \dfrac{e^{-\eta\rho}}{\rho} \end{cases}, \tag{16}$$

where the second equality one can be verified by direct application of the SI. The first property in equation (16) ensures automatic extrapolation of R_3 by its expansion over IQ RBFs. In addition, by the second property in equation (16) the inverse transform of the residual function can be computed analytically. Thus, the problem to be solved simplifies to the evaluation of

$$F_l(\rho) = \int_{\mathrm{SIP}_1} R_l(k_\rho)\cdot J_0(k_\rho \rho)\,dk_\rho, \qquad l = 1, 3. \tag{17}$$

For this purpose, consider the following expansion,

$$R^l(k_\rho)\Big|_{\mathrm{SIP}_1} \cong \sum_{i=1}^{N_l} w_i{}^l \varphi_i{}^l(k'_\rho), \qquad l = 1, 3 \tag{18}$$

where N_l is the number of samples along SIP$_1$ for describing R_l at $k^l_{\rho,i}, i = 1,\ldots,N_l$. Replacing equation (18) into equation (17) and following the final remark of the previous section, the SIP$_1$ can be extended to SIP$_2$

$$\mathrm{SIP}_2 : k_\rho = \begin{cases} k'_\rho + j\gamma k_0, & 0 \le k'_\rho < \infty \\ k'_\rho, & -\infty \le k'_\rho < 0 \end{cases}. \tag{19}$$

This makes is possible to rewrite equation (17) as,

$$F_l(\rho) = \sum_{i=1}^{N} w_i^l \int_{\mathrm{SIP}_2} \varphi_i{}^l(k'_p)\cdot J_0(k_\rho \rho)\,dk_\rho, \qquad l = 1, 3 \tag{20}$$

which by using [23] leads

$$2J_0(z) = H_0^{(1)}(z) - H_0^{(1)}(-z), \tag{21}$$

can be expressed as,

$$F_l(\rho) = F_l^+(\rho) + F_l^-(\rho), \qquad l = 1, 3 \tag{22}$$

with

$$\begin{cases} F_l^+(\rho) = +\dfrac{1}{2}\displaystyle\sum_{i=1}^{N} w_i{}^l \int_{\mathrm{SIP}_2} \varphi_i{}^l(k'_p) H_0^{(1)}(+k_\rho \rho)\,dk_\rho \\ F_l^-(\rho) = -\dfrac{1}{2}\displaystyle\sum_{i=1}^{N} w_i{}^l \int_{\mathrm{SIP}_2} \varphi_i{}^l(k'_p) H_0^{(1)}(-k_\rho \rho)\,dk_\rho \end{cases}, \; l = 1, 3 \tag{23}$$

where H_0 is the zero order Hankel function. At this step, noting that $H_0^{(1)}(z)$ is analytic at $+j\infty$, the integration paths corresponding to F_l^+ and F_l^- are closed by hemi-circles of infinite radii at upper and lower half planes, respectively. Doing so, equation (23) can be analytically evaluated by direct application of the residue theorem, i.e.,

$$\begin{cases} F_l^+(\rho) = +j\pi \displaystyle\sum_{i=1}^{N} \frac{w_i{}^l}{j2A_i{}^l} H_0^{(1)}\left[+\left(k^{\,l}_{\rho,i} + jA_i{}^l\right)\rho\right] \\ F_l^-(\rho) = -j\pi \displaystyle\sum_{i=1}^{N} \frac{w_i{}^l}{j2A_i{}^l} H_0^{(1)}\left[-\left(k^{\,l}_{\rho,i} + jA_i{}^l\right)\rho\right] \end{cases}, \; l = 1, 3 \tag{24}$$

where A_i^l is the corresponding shape parameter. This completes the proposed approach of the problem.

V. NUMERICAL RESULTS

In this section, the proposed method is applied to a microstrip substrate with $\varepsilon_r = 12.6$ and $h = 1$ *mm* illuminated at $f_0 = 30$ *GHz*. In addition, it is assumed that $\gamma = 10^{-3}$, $\eta = 10^2$, $0 \le k_\rho' \le 7k_0$ and $z = z' = 0$. Using this small value of γ, the information content of singularities are well-preserved and it is expected the method to be able to track the spatial-domain GFs at distances considerably far from the origin. Under the above conditions, the corresponding R_1 and R_3 functions are interpolated based on their non-uniform samples, depicted in Fig. 1. For this purpose, a simple algorithm is developed, which its details are beyond the scope of the paper. As a brief description, the algorithm starts with dividing the domain of the function to number of sub-intervals. Then, it iteratively increases the number of samples in each sub-interval, uniformly, unless the error in the corresponding sub-interval becomes less than a predetermined value. The non-uniform sampling has decreased the number of sample from 8887 to 406 for R_1, and from 9678 to 1232 for R_3, which corresponds to the reduction ratio of 95.4 % and 87.3 %, respectively. For clearly demonstrating the capability of IQ RBFs in tracking harsh variations, the singular regions of the functions are enlarged and depicted in Fig. 2. Applying the proposed method to IQ interpolation of R_1 and R_3, the amplitude of G_A^{xx} and G_q functions are evaluated and compared to their corresponding exact values in Figs. 3 (a) and (b), respectively. By exact value, we mean the value computed by direct numerical integration. For better showing the accuracy of the proposed method, the oscillating part of G_q is enlarged and depicted in Fig. 3 (c). Finally, the effect of γ is studied on G_A^{xx} and reported in Fig. 4. As is clear and was predictable, the valid range of far-field increases as γ decreases.

VI. CONCLUSION

The IQ RBFs are used for expanding the spectral-domain GFs of a microstrip thick substrate. The Sommerfeld integrals corresponding to spatial-domain GFs are then analytically evaluated by the residue theorem. This led to representing electromagnetic fields only by cylindrical waves. In view of extreme capability of

RBFs in data fitting, the SIP is deformed to pass from vicinity of singularities of spectral-domain GFs in the complex k_ρ-plain, which led to accurate evaluation of far-fields up to $\log_{10}(k_0\rho) = 3$. Moreover, the scattered data interpolation ability of RBFs is utilized for non-uniform sampling of the SIP which has led to considerable increase in computational efficiency.

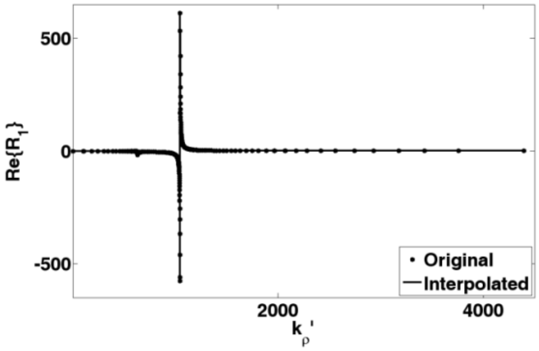

(a)

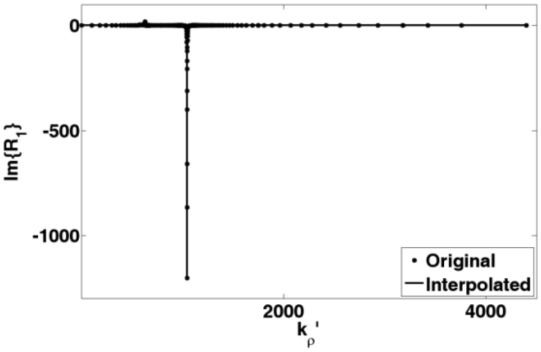

(b)

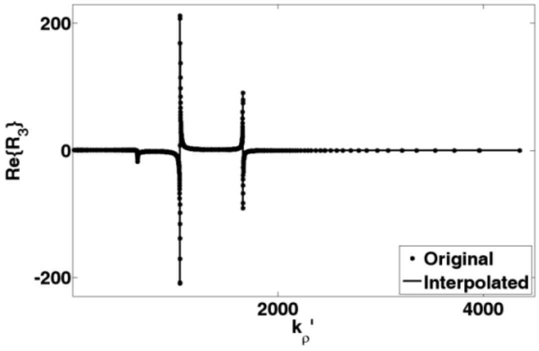

(c)

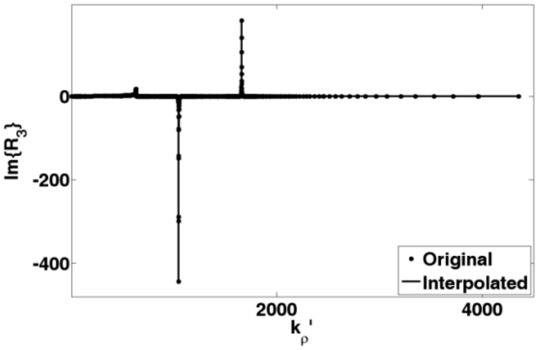

(d)

Fig. 1. IQ interpolation of R_1 and R_3 for (a) Re{R_1}, (b) Im{R_1}, (c) Re{R_3}, and (d) Im(R_3).

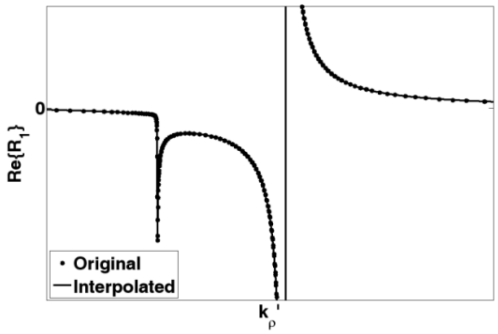

(a)

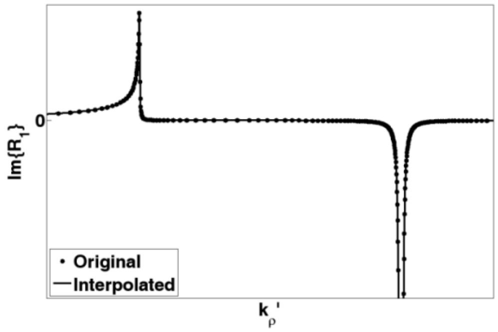

(b)

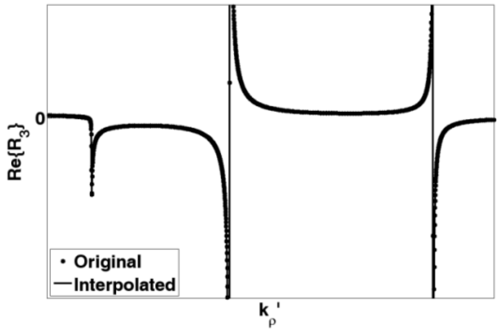

(c)

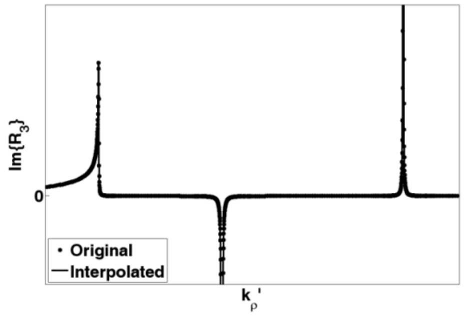

(d)

Fig. 2. IQ interpolation of R_1 and R_3, enlarged at singular regions for (a) Re{R_1}, (b) Im{R_1}, (c) Re{R_3}, and (d) Im(R_3).

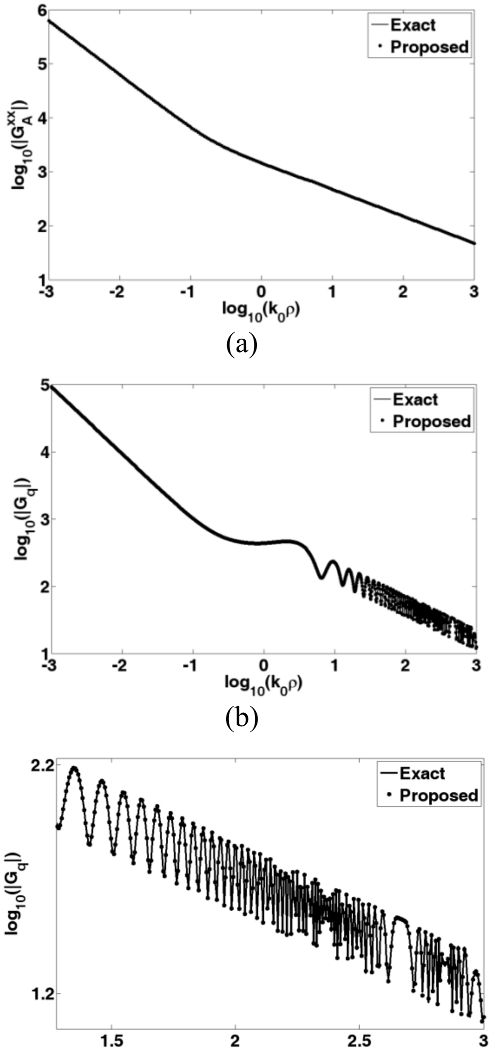

(a)

(b)

(c)

Fig. 3. The amplitude of spatial-domain GFs for (a) G_A^{xx}, (b) G_q, (c) G_q enlarged at its oscillating part.

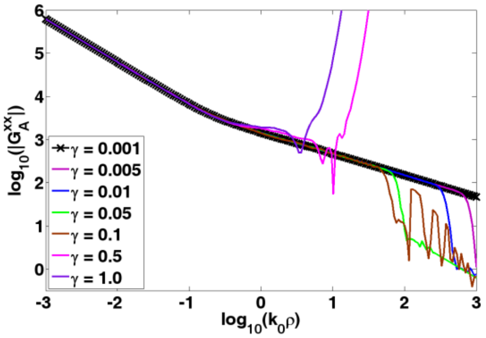

Fig. 4. Effect of γ on G_A^{xx}.

ACKNOWLEDGMENT

The authors acknowledge Dr. A. H. Shoory for inputs in Green's function of multilayered media. The authors thank reviewers for many constructive comments.

REFERENCES

[1] A. Taflove and S. Hagness, *Computational Electrodynamics*, Third Edition. Artech House, 2005.
[2] J. Jin, *The Finite Element Method in Electromagnetics*, 2nd John Wiley & Sons, 2002.
[3] J. G. Van Bladel, *Singular Electromagnetic Fields and Sources*. Wiley-IEEE Press, 1996.
[4] R. Bancroft, *Understanding Electromagnetic Scattering Using the Moment Method*. Artech House, 1996.
[5] W. C. Chew, *Waves and Fields in Inhomogeneous Media*. IEEE Press, 1995.
[6] Y. L. Chow, J. J. Yang, D. G. Fang, and G. E. Howard, "A closed-form spatial Green's function for the thick microstrip substrate," *IEEE Trans. Microwave Theory Tech.*, vol. 39, no. 3, pp. 588-592, 1991.
[7] M. I. Aksun, "A robust approach for the derivation of closed-form Green's functions," *IEEE Trans. Microwave Theory Tech.*, vol. 44, no. 5, pp. 651-658, 1996.
[8] F. Ling and J. Jin, "Discrete complex image method for Green's functions of general multilayer media," *IEEE Microwave and Guided Wave Letters*, vol. 10, no. 10, pp. 400-402, 2000.
[9] Y. Ge and K. P. Esselle, "New closed-form Green's functions for microstrip structures theory and results," *IEEE Trans. Microwave Theory Tech.*, vol. 50, no. 6, pp. 1556-1560, 2002.
[10] M. Yuan, T. K. Sarkar, and M. Salazar-Palma, "A direct discrete complex image method from the closed-form Green's functions in multilayered media," *IEEE Trans. Microwave Theory Tech.*, vol. 54, no. 3, pp. 1025-1032, 2006.

[11] V. N. Kourkoulos and A. C. Cangellaris, "Accurate approximation of Green's functions in planar stratified media in terms of a finite sum of spherical and cylindrical waves," *IEEE Trans. Antennas Propag.*, vol. 54, no. 5, pp. 1568-1576, 2006.

[12] A. G. Polimeridis, T. V. Yioultsis, and T. D. Tsiboukis, "A robust method for the computation of Green's functions in stratified media," *IEEE Trans. Microwave Theory Tech.*, vol. 55, no. 7, pp. 1963-1969, 2007.

[13] M. M. Tajdini and A. A. Shishegar, "A novel analysis of microstrip structures using the Gaussian Green's function method," *IEEE Trans. Antennas Propagat.*, vol. 58, no. 1, pp. 88-94, 2010.

[14] J. W. Brown, R. V. Churchill, *Complex Variables and Applications*. McGraw-Hill, 1996.

[15] R. W. Hamming, *Numerical Methods for Scientists and Engineers*. Dover Publications, 1987.

[16] Y. Hua and T. K. Sarkar, "Generalized pencil-of-function method for extracting poles of an EM system from its transient response," *IEEE Trans. Antennas. Propagat*., vol. 37, no. 2, pp. 229-234, 1989.

[17] T. K. Sarkar and O. Pereira, "Using the matrix pencil method to estimate the parameters of a sum of complex exponentials," *IEEE Antennas Propagat. Mag*., vol. 37, no. 3, pp. 48-55, 1995.

[18] B. Gustavsen and A. Semlyen, "Rational approximation of frequency domain responses by vector fitting," *IEEE Trans. Power Delivery*, vol. 14, no. 3, pp. 1052-1061, 1999.

[19] B. Fornberg and C. Piret, "On choosing a radial basis function and a shape parameter when solving a convective PDE on a sphere," *Elsevier J. Comput. Phys*., vol. 227, pp. 2758-2780, 2008.

[20] M. J. D. Powell. "The theory of radial basis function approximations in 1990," *Advances in Numerical Analysis: Wavelets, Subdivision Algorithms, and Radial Basis Functions*, vol. 2. W. Light, Ed. USA: Oxford University Press, pp.105-210, 1992.

[21] G. R. Liu, *Mesh Free Methods*. CRC Press, 2003.

[22] G. R. Liu and Y. T. Gu, *An Introduction to MeshFree Methods and Their Programming*, Springer, 2005.

[23] A. Banos, *Dipole Radiation in the Presence of a Conducting Half-Space*, Pergamon, 1966.

Babak Honarbakhsh was born in Tehran, Iran. He received his B.Sc. and M.Sc. degrees in Electrical Engineering from Amirkabir University of Technology where he is currently working toward his Ph.D. degree. His current research interest is numerical solution of electromagnetic problems by meshfree methods.

Ahad Tavakoli was born in Tehran, Iran, on March 8, 1959. He received B.Sc. and M.Sc. degrees from the University of Kansas, Lawrence, and the Ph.D. degree from the University of Michigan, Ann Arbor, all in electrical engineering, in 1982, 1984, and 1991, respectively. He is currently a Professor in the Department of Electrical Engineering at Amirkabir University of Technology. His research interests include EMC, scattering of electromagnetic waves and microstrip antennas.

Analysis of Thick Microstrip Antennas by the Meshfree Collocation Method

B. Honarbakhsh[1] **and A. Tavakoli**[1, 2]

[1]Department of Electrical Engineering
[2]Institute of Communications Technology and Applied Electromagnetics
Amirkabir University of Technology (Tehran Polytechnic), Tehran, IRAN
b_honarbakhsh@aut.ac.ir and tavakoli@aut.ac.ir

Abstract ─ A meshless integration free approach is applied to numerical solution of the mixed potential integral equation (MPIE) governing various microstrip resonators/antennas. The idea behind the discrete complex image method (DCIM) is exploited to provide closed form expressions for all of the integrals, leading to an efficient spectral-domain meshless integral equation (IE) solver. The proposed meshfree method (MFM) is compared with low order method of moments (MoM) from the aspects of memory usage and simulation time, which shows superior performance of the MFM.

Index Terms - Collocation, meshfree, microstrip antenna, MoM, RBF, and Shepard.

I. INTRODUCTION

Currently, meshfree methods (MFMs) are well-known as partial differential equation (PDE) solvers and the amount of research devoted to meshless solution of integral equations (IEs) is negligible [1-7]. Not so far, a study is reported on numerical solution of electromagnetic (EM) IEs by the meshfree collocation method (MCM) [7]. The purpose of this work is applying that method to the analysis of microstrip resonators/antennas by meshfree (meshless) solution of the mixed potential integral equation (MPIE) [8]. This equation is the most practical IE in numerical solution of microstrip structures due to its weak singular kernels, numerical stability, and intense capability of handling multilayered media [9].

At present, the method of moments (MoM) is known as the most versatile numerical method for such problems. One of the pre-assumptions in MoM is partitioning the problem domain by meshes. The unknown field variable is then expanded over known basis functions with unknown weightings on each mesh, leading to discretization of the IE. These expansion functions most often have simple mathematical form and thus, low reconstruction capability. Although it is possible to use basis functions with high reconstruction ability, currently the most used MoM solvers are of low order. Hereafter in this paper, by MoM it is meant low order MoM, which exploits pulse/roof-top basis functions.

In contrast to MoM, MFMs discretize operator equations by nodes instead of meshes and utilizing meshfree shape functions. These functions are highly complicated, with excellent fitting capability [10]. Thus, it is expected that MFMs be able to solve the same problem with less number of unknowns compared to MoM, leading to save in memory usage. On the other hand, noting that evaluation of meshless shape functions often requires matrix computations, MFMs are expected to be slow solvers. This makes meshless solution of IEs a challenging problem.

For decreasing the simulation time, guidelines reported in [7] are followed throughout this paper, which has led to less computational cost with respect to MoM. Since all numerical integrations are effectively carried out in the spectral domain, the proposed method can be regarded as the meshless counterpart of the spectral domain MoM. This study covers different aspects of geometries, feeding techniques, nature of structures, and number of exciting ports. For decoupling the effect of the substrate Green's functions (GFs) from the

Submitted On: Aug. 20, 2012
Accepted On: Nov. 25, 2012

method itself, the first four structures are analyzed based of air-filled substrate and for completeness, the last case is devoted to a realistic antenna.

All MFM simulations are carried out based on regular node arrangements. This restriction is due to presently available strategy for bypassing numerical integration. By introducing wise irregularity in node distribution, the scattered data fitting capability of meshless shape functions can be exploited which leads to more decrease in the number of unknowns. Nevertheless, although the present study has led to over sampling of the problem domain, both of the number of unknowns and simulation time are decreased compared to MoM. The main ideas of the method are general and can be applied to arbitrary node arrangements. Finally, it should be pointed out that by “thick” we mean that the variations of EM fields normal to the substrate are not neglected in this work.

II. MATHEMATICAL STATEMENT OF THE PROBLEM

Consider a planar microstrip structure of domain Ω and boundary ∂Ω, illuminated by an incident electric field, $\mathbf{E}^i$. The MPIE governing this problem can be expressed as

$$\begin{cases} \mathbf{n}\times\mathbf{E}^i = \mathbf{n}\times\left(j\omega\mathbf{A}+\nabla V\right), \text{ in problem domain} \\ \mathbf{m}\cdot\mathbf{J}_s = 0, \text{ on smooth boundaries} \\ \mathbf{J}_s = 0, \text{ on convex corners} \end{cases}, \quad (1)$$

where **n** and **m** are unit normal vectors to Ω and ∂Ω, respectively, with $\mathbf{n}\cdot\mathbf{m}=0$. In addition

$$\begin{cases} \mathbf{A}(\boldsymbol{\rho}) = \mu_0\int_\Omega \overline{\overline{\mathbf{G}}}_A(\boldsymbol{\rho},\boldsymbol{\rho}')\cdot\mathbf{J}_s(\boldsymbol{\rho}')d\Omega \\ \varepsilon_0 V(\boldsymbol{\rho}) = \int_\Omega G_V(\boldsymbol{\rho},\boldsymbol{\rho}')\rho_s(\boldsymbol{\rho}')d\Omega \end{cases}, \quad (2)$$

where $\overline{\overline{\mathbf{G}}}_A$ and G_V are dyadic and scalar GFs of the substrate medium, respectively [9]. As well, ρ_s and $\mathbf{J}_s$ are related by the continuity equation, i.e.,

$$\nabla\cdot\mathbf{J}_s + j\omega\rho_s = 0. \quad (3)$$

In conventional MoM solvers, $\mathbf{J}_s$ is expanded over a set of basis functions satisfying boundary conditions (BCs) and equation (2) is injected in equation (1). Thus, the problem reduces to

$$\varepsilon_0\mathbf{n}\times\mathbf{E}^i(\boldsymbol{\rho}) = \mathbf{n}\times\left[j\omega\varepsilon_0\mu_0\int_\Omega \overline{\overline{\mathbf{G}}}_A(\boldsymbol{\rho},\boldsymbol{\rho}')\cdot\mathbf{J}_s(\boldsymbol{\rho}')d\Omega \right. \quad (4)$$
$$\left. +\nabla\int_\Omega G_V(\boldsymbol{\rho},\boldsymbol{\rho}')\rho_s(\boldsymbol{\rho}')d\Omega \right],$$

and is solved by a weighted residual method, which is usually of the Galerkin type. This choice with applying integration by parts, removes the gradient operator [9]. As the MoM enforces the basis functions to be only linear independent, it is possible to use simple functions such as rectangular pulses and roof-tops. These functions have low order of continuity, and therefore, differentiation is not straightforward, if not impossible. On the other hand, this option simplifies computing of fourfold integrals appearing in solution of 2D problems.

In contrast to MoM, MFM not only enforces the meshless shape functions to be linear independent, but also imposes them to be either approximants or interpolants. Sample 1D approximant and interpolant meshless shape functions are depicted in Fig. 1.

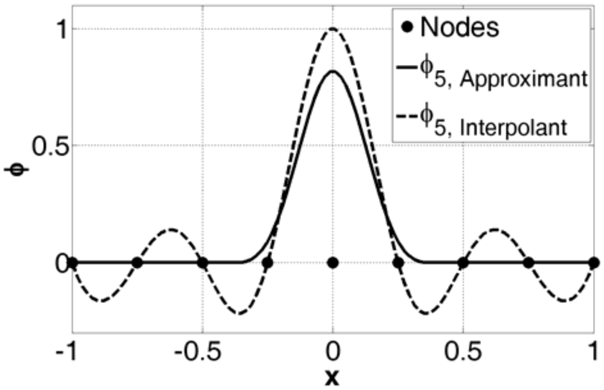

Fig. 1. Sample 1D approximant and interpolant meshless shape functions.

Clearly, construction of meshless shape functions satisfying the BCs of equation (1) is too hard, if not impossible. As stated earlier, these functions possess high order of continuity and their evaluation is computationally expensive. Thus, numerical integration over them is time consuming, which makes application of the Galerkin method computationally inefficient. As a conclusion, for meshless solution of the MPIE, we suggest the collocation method, without replacing equation (2) into equation (1).

III. MESHLESS DISCRETIZATION

The first step for meshless discretization is to scatter M nodes in the problem domain and on its boundary. This leads to nodal description of the problem. Next, the unknown field variable should be expanded over meshless shape functions. This step is highly problem dependent. An improper selection of expansion functions leads to inaccuracy and/or computational inefficiency. Considering the present formulation, i.e., equations (1) and (2), reveals that the problem can be regarded as a combination of two parts; the differential part, i.e., equation (1), and an integral part, i.e., equation (2). Thus, the field variable V should be expanded over a set of smooth functions; no matter they are localized or distributed over the entire problem domain. We suggest expanding V over radial basis function (RBF) interpolants and not over moving least square (MLS) approximants. For detailed introduction to meshless shape functions, the reader is referred to [10]. The relative computational cost of evaluating the differential part for a sample 2D problem is reported in Fig. 2, wherein conventional MLS and RBF shape functions are used.

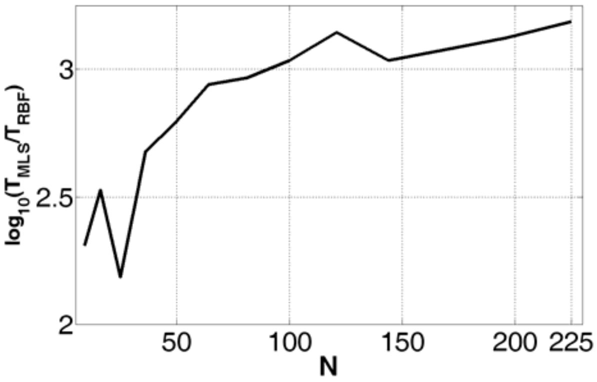

Fig. 2. Relative computational cost of evaluating the differential part for a sample 2D problem.

On the other hand, $\mathbf{J}_s$ should be expanded over functions, which are localized over a small portion of the problem domain. If not, integration over each of the corresponding shape functions requires either huge number of quadrature points or a back ground mesh. The computational cost of evaluating the integral part for a sample 2D problem using conventional MLS, Shepard and RBF shape functions is reported in Fig. 3. Thus, we suggest expanding $\mathbf{J}_s$ over Shepard approximants [11], which their evaluation does not require matrix computations.

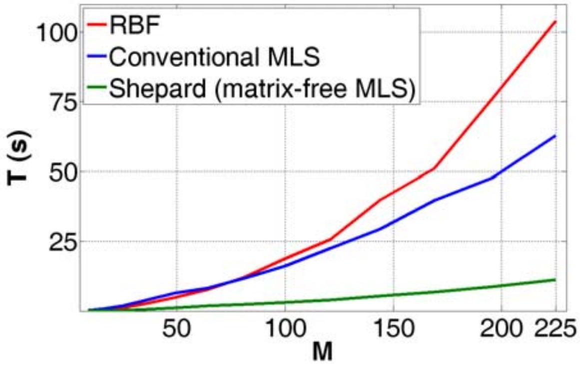

Fig. 3. Computational cost of evaluating the integral part for a sample 2D problem using different meshless shape functions.

Assume $\{\varphi_i\}_{i=1}^{M}$ and $\{\psi_i\}_{i=1}^{M}$ be sets of, respectively, interpolants and approximants corresponding to nodes describing the problem. Therefore,

$$\begin{cases} V^h(\boldsymbol{\rho}) = \boldsymbol{\Phi}^T(\boldsymbol{\rho}) \cdot \widehat{\mathbf{V}} = \sum_{i=1}^{M} \varphi_i(\boldsymbol{\rho}) \widehat{V_i} \\ A_\alpha^h(\boldsymbol{\rho}) = \boldsymbol{\Phi}^T(\boldsymbol{\rho}) \cdot \widehat{\mathbf{A}_\alpha} = \sum_{i=1}^{M} \varphi_i(\boldsymbol{\rho}) \widehat{A_{\alpha,i}}, \\ J_\alpha^h(\boldsymbol{\rho}) = \boldsymbol{\Psi}^T(\boldsymbol{\rho}) \cdot \widehat{\mathbf{J}_\alpha} = \sum_{i=1}^{M} \psi_i(\boldsymbol{\rho}) \widehat{J_{\alpha,i}} \end{cases} \tag{5}$$

with

$$\begin{cases} \widehat{\mathbf{V}} = \left[\widehat{V_1} \quad \ldots \quad \widehat{V_M} \right]^T \\ \widehat{\mathbf{A}_\alpha} = \left[\widehat{A_{\alpha,1}} \quad \ldots \quad \widehat{A_{\alpha,M}} \right]^T, \\ \widehat{\mathbf{J}_\alpha} = \left[\widehat{J_{\alpha,1}} \quad \ldots \quad \widehat{J_{\alpha,M}} \right]^T \end{cases} \tag{6}$$

where V^h and A_α^h are interpolated value of V and A_α, respectively, J_α^h is the approximated value of J_α, and α is either of x or y. Collocating sides of equation (5) and the first of equation (1) at the nodes yields

$$\mathbf{L} \cdot \hat{\mathbf{J}} = \mathbf{b}, \tag{7}$$

where

$$\begin{cases} \mathbf{L} = \begin{bmatrix} \mathbf{L}_{11} & \mathbf{L}_{12} \\ \mathbf{L}_{21} & \mathbf{L}_{22} \end{bmatrix} \\ \hat{\mathbf{J}}^T = \left[\widehat{\mathbf{J}_x}^T \quad | \quad \widehat{\mathbf{J}_y}^T \right], \\ \mathbf{b}^T = \left[E_{x,1}^i \cdots E_{x,M}^i \mid E_{y,1}^i \cdots E_{y,M}^i \right] \end{cases} \tag{8}$$

with

$$\begin{cases} \mathbf{L}_{11} = j\omega\mu_0\mathbf{K}_1 - \left(j\omega\varepsilon_0\right)^{-1}\mathbf{\Phi}_x\cdot\mathbf{K}_2 \\ \mathbf{L}_{12} = -\left(j\omega\varepsilon_0\right)^{-1}\mathbf{\Phi}_x\cdot\mathbf{K}_3 \\ \mathbf{L}_{21} = -\left(j\omega\varepsilon_0\right)^{-1}\mathbf{\Phi}_y\cdot\mathbf{K}_2 \\ \mathbf{L}_{22} = j\omega\mu_0\mathbf{K}_1 - \left(j\omega\varepsilon_0\right)^{-1}\mathbf{\Phi}_y\cdot\mathbf{K}_3 \end{cases}, \tag{9}$$

and

$$\begin{cases} \left[\mathbf{K}_1\right]_{ij} = \int\limits_{\Omega}\psi_j\left(\boldsymbol{\rho}'\right)G_A^{xx}\left(\boldsymbol{\rho}_i,\boldsymbol{\rho}'\right)d\Omega \\ \left[\mathbf{K}_2\right]_{ij} = \int\limits_{\Omega}\psi_{j,x}\left(\boldsymbol{\rho}'\right)G_V\left(\boldsymbol{\rho}_i,\boldsymbol{\rho}'\right)d\Omega. \\ \left[\mathbf{K}_3\right]_{ij} = \int\limits_{\Omega}\psi_{j,y}\left(\boldsymbol{\rho}'\right)G_V\left(\boldsymbol{\rho}_i,\boldsymbol{\rho}'\right)d\Omega \end{cases} \tag{10}$$

The unknown field variable $\hat{\mathbf{J}}$ can now be computed by solving the linear system of equation (7) after imposition of BCs, which is now straightforward.

IV. COMPUTATION OF THE L MATRIX

This section follows [7]. The computational cost of the **L** matrix is mainly due to matrices introduced in equation (10). The key point is noting the fact that under the assumption of regular node arrangement, Shepard functions become bell-shaped and consequently, can be well approximated by a single Gaussian function. Hereafter, we assume

$$\psi_i\left(x+x_i, y+y_i\right) = \exp\left[-\left(\xi_x^{(i)}x^2 + \xi_y^{(i)}y^2\right)\right], \tag{11}$$

where a_i, $\xi_x^{(i)}$ and $\xi_y^{(i)}$ are constants corresponding to the i^{th} approximant and can be simply estimated by curve fitting methods. This point, itself, simplifies handling the problem and increases computational efficiency. The aforementioned matrices can be computed in both of space and spectral domains. Thus, we split this section to two parts and discuss each one separately.

A. Space domain

Computation in the space domain requires evaluation of space domain GFs of the problem. Although the GFs of multi-layered media have closed forms in the spectral domain, their evaluation in the space domain has a long history and still is known as an active research topic. Currently, one of the most famous and efficient approaches used for this purpose, is the discrete complex image method (DCIM) [12, 13]. The DCIM is a general idea for computing the inverse Fourier-Bessel transform and, itself, can be implemented in a variety of ways. In this work, we have followed [13] which, for the problem at hand, express the space domain GFs as a sum of complex-valued spherical wave, i.e.,

$$\begin{cases} G\left(\boldsymbol{\rho},\boldsymbol{\rho}'\right) = \sum_{p=1}^{P} c_p \dfrac{e^{-jk_0 r_p}}{4\pi r_p} \\ r_p = \sqrt{\left|\boldsymbol{\rho}-\boldsymbol{\rho}'\right|^2 - d_p^2} \end{cases}, \tag{12}$$

where $c_m, d_m \in \mathbb{C}$ and $G = G_A^{xx}, G_A^{yy}, G_V$. Details of this method are beyond the scope of this work. Considering equations (10) to (12), the mathematical form of the first integrals in equation (10) can be stated as

$$\begin{cases} f\left(m,n\right) = \int\limits_{\Omega_n} f_m\left(x,y\right)f_n\left(x,y\right)d\Omega \\ f_m\left(x+x_m, y+y_m\right) = \dfrac{\exp\left[-jk_0\sqrt{x^2+y^2-d_p^2}\right]}{\sqrt{x^2+y^2-d_p^2}} \\ f_n\left(x+x_n, y+y_n\right) = \exp\left[-\left(\xi_x^{(n)}x^2 + \xi_y^{(n)}y^2\right)\right] \end{cases}, \tag{13}$$

where Ω_n is the support of the n^{th} approximant. The other integrals can be stated, and consequently treated similarly. This integral has a potential first order singularity and is classified as a weak singular integral. Nevertheless, for fast and accurate numerical integration, all sharp behaviours and infinite values of the integrand should be avoided. Such integrals can be evaluated numerically by applying the Duffy transform, which is simple to implement and annihilates the possible singularity at the expense of triangular meshing the integration domain and the corresponding increase in computational complexity [14].

B. Spectral domain

It is well known that all integrals of equation (10) are linear convolutions. This fact can be exploited to calculate equation (10) by the continuous Fourier transform (CFT), e.g., the j^{th} column of $\mathbf{K}_1$ can be computed as follows

$$\left[\mathbf{K}_1\right]_{ij} = \mathcal{F}^{-1}\left\{\mathcal{F}\left\{\psi_j\right\}\cdot\mathcal{F}\left\{G_A^{xx}\right\}\right\},\quad i=1,\ldots,M, \tag{14}$$

where $\mathcal{F}$ stands for CFT. A situation exists, which can decrease the computational cost of the method by providing closed form expressions for the integrals of equation (10). Suppose,

$$\begin{cases} \psi_i(\boldsymbol{\rho}) = \psi(\boldsymbol{\rho} - \boldsymbol{\rho}_i) \\ \xi_x^{(i)} = \xi_y^{(i)} = \xi \end{cases}, \quad 1 \le i \le M \tag{15}$$

which is met by nodal arrangements with equal radial distance. Thus, the mathematical forms of the required integrals are

$$\begin{cases} g_1(\boldsymbol{\rho}) = \int_0^\infty e^{-\frac{k_\rho^2}{4\xi}} \widetilde{G_A^{xx}}\left(k_\rho^2\right) J_0\left(k_\rho \rho\right) k_\rho dk_\rho \\ g_2(\boldsymbol{\rho}) = \cos\varphi \int_0^\infty e^{-\frac{k_\rho^2}{4\xi}} \widetilde{G_V}\left(k_\rho^2\right) J_1\left(k_\rho \rho\right) k_\rho^2 dk_\rho \,, \\ g_3(\boldsymbol{\rho}) = \sin\varphi \int_0^\infty e^{-\frac{k_\rho^2}{4\xi}} \widetilde{G_V}\left(k_\rho^2\right) J_1\left(k_\rho \rho\right) k_\rho^2 dk_\rho \,, \end{cases} \tag{16}$$

where $\widetilde{G}$ stands for the spectral domain counterpart of G. The remained step is computing the above Sommerfeld-type integrals, which can be done by following the strategy introduced in [13]. The time gain achieved by computing the first integral of equation (16) in space and spectral domains for a sample 2D problem is reported in Fig. 4. Relaxing the condition of equation (15) does not invalidate this approach. Application to general case is under study.

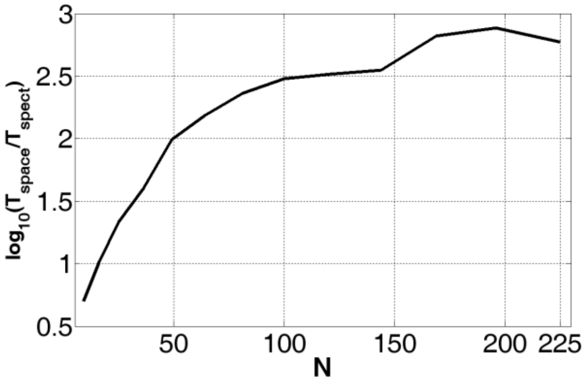

Fig. 4. Time gain achieved by computing the first integral of equation (16) in space and spectral domains.

V. FEED MODELING

There are varieties of methods for feeding microstrip antennas [9, 15]. One of the most practical picks is to directly connect a microstrip line to the radiating patch. This choice has two valuable benefits. First, it preserves the planarity of the problem and restricts the discretization to the microstrip plane. Second, it allows analysis of the problem by the collocation method. This is in contrast to feeding by vertical filament acting on some point of the upper conductor, which requires a distributed weighting function needed for absorbing the singularity of the Dirac delta function. Another choice is proximity feeding technique, in which the feed line truncates at the vicinity of the radiating element. Although this case preserves benefits of the former one, the coupling of EM energy is drastically decreased compared to that, making the impedance matching difficult. Moreover, the high sensitivity of the return loss to the distance between the line and patch makes this choice impractical. Nevertheless, from numerical stand point and for the purpose of validation, both of the aforementioned methods are used in this study.

Another point that should be noted is the mathematical form of the excitation function. In MoM, it is straightforward to use a half roof-top function with acting at the first mesh of the feed line. In this case the EM field distribution of the exciting function suddenly drops from its maximum value to zero. This sharp variation does not affect the solution and satisfactory results are obtained following this strategy. We have found that meshless methods are incapable of handling abrupt changes. In fact, we could not get satisfactory results from the proposed method unless we modeled the excitation by a smooth decaying function. In this study, a slowly decaying Gaussian function is used. At present, the optimum value for the damping factor is unknown to us.

VI. NUMERICAL DE-EMBEDDING

A crucial step in both of the measurement and numerical analysis of microwave components is extracting the scattering (S) parameters. The difficulty of this step arises from the disturbance of the EM field at the source/load location. The process of extracting the effect of the source/load from the intrinsic behavior of the component is called de-embedding. In the context of numerical solution, this problem resembles itself, specially, when dealing with IE solvers and is called numerical de-embedding. Number of strategies is introduced for this purpose, e.g., [16, 17]. In this work, we followed [17]; it is simple and does not need knowledge of characteristic impedance of the feed line and its guiding wave length.

VII. NUMERICAL RESULTS

In this section, the proposed method is applied to five microstrip structures: a linear resonator, a proximity-coupled circular resonator, a proximity-coupled antenna array, a line-fed dual-polarized patch antenna, and a line-fed patch antenna. One of the vital steps in such analysis is evaluating of integrals including GFs of layered media. Any error in this step, directly affects the final result. Thus, for decoupling the effect of GFs from the method, the first four problems are devoted to substrates with ε_r = 1. These problems prove the capability of the method in handling various geometries and different feeding techniques. The final problem is a realistic microstrip antenna with ε_r = 2.2. The MFM analysis is based on the proposed spectral domain strategy. Apparently, it is also possible to evaluate the coefficient matrix by direct numerical integration in the space domain.

Meshless interpolants are constructed by the following compactly supported positive definite RBF [10],

$$R(\boldsymbol{\rho}) = \begin{cases} (1-\eta)^5 \\ \times\left(8+40\eta+48\eta^2+25\eta^3+5\eta^4\right), 0 \le \eta \le 1 \\ 0, \eta > 1 \end{cases} \tag{17}$$

where $\eta = \rho/r_I$, with r_I being the interpolant support size. For the first four problems $r_I = 30d_r$, and for the last one $r_I = 10d_r$ where d_r is the radial nodal distance. As well, Shepard approximants are constructed from the following quadric spline function [10],

$$w(\boldsymbol{\rho}) = \begin{cases} 1-6\eta^2+8\eta^3-3\eta^4, 0 \le \eta \le 1 \\ 0, \eta > 1 \end{cases} \tag{18}$$

where $\eta=\rho/r_A$, with r_A being the approximant support size and is set to $r_A=1.2d_r$ for all cases. These functions are approximated by Gaussian functions with equal amplitude and damping factors in *x* and *y* directions. Unfortunately, in the cases of circular resonator and dual polarized antenna, the computed input impedances are not in adequate agreement with MoM. This may be resulted from unsuccessful numerical de-embedding. Thus, in these cases, the monostatic radar cross section (RCS) computed by the proposed MFM and MoM are also provided to verify the validity of the method. For this purpose, the aforementioned structures are excited by x-polarized uniform plain wave. MoM results corresponding to S-parameter and RCS are computed by Agilent Momentum 2009 and FEKO suite 5.5, respectively. Finally, the plat form used is an Intel (R) Core (TM) 2 CPU with 4 GB RAM.

A. Linear resonator

Consider a 50 mm × 2.5 mm rectangular strip on a substrate with ε_r = 1 and h = 0.794 mm. The first resonance frequency of this structure can be analytically estimated to be 3 GHz. The node arrangement, BCs, current density distribution and the corresponding input impedance are depicted in Fig. 5. The computed results are in agreement with theoretical expectations.

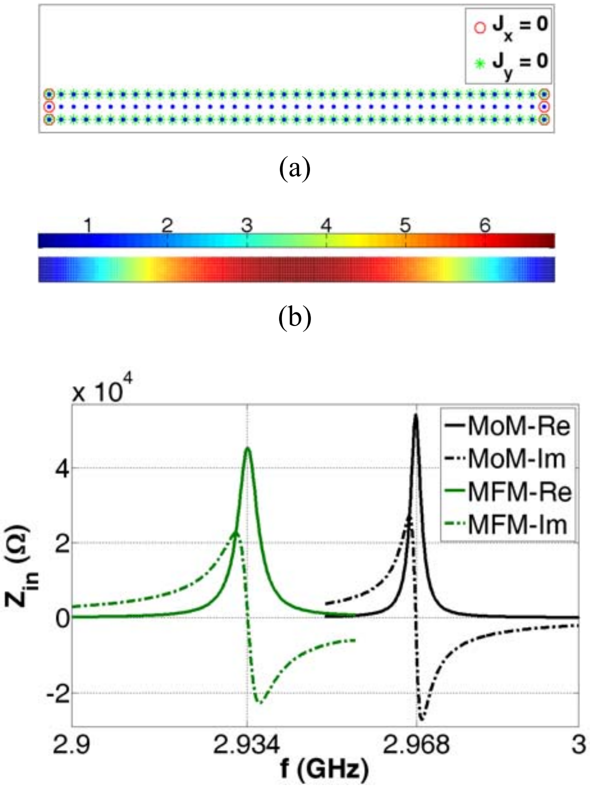

(a)

(b)

(c)

Fig. 5. Linear resonator for (a) nodal arrangement and BCs, (b) current density distribution, and (c) input impedance.

B. Proximity-coupled circular resonator

For verifying the applicability of the method to non rectangular geometries, consider a narrow ring, centered at the origin and fed by a 30 mm × 2.4 mm strip. The inner and outer radii of the ring are 7.5 mm and 10 mm, respectively. The ring and the feed line are positioned 2 mm apart and are placed on a substrate with $\varepsilon_r = 1$ and $h = 1.6$ mm. The resonance frequency of the ring can be estimated to be 5.46 GHz. The nodal arrangement and BCs, current density distribution and the corresponding input impedance are depicted in Fig. 6. The computed results are in accordance with physical sense. Specially, Fig. 6 (b) shows how the EM energy is coupled to the ring at the resonance. Additionally, the capacitive nature of the feeding structure can be concluded from the imaginary part of input impedance. However, adequate agreement between MFM and MoM cannot be seen, which may be stem from unsuccessful numerical de-embedding. Thus, the normalized RCS is also computed by both of the methods and reported in Fig. 6 (d) for further validation of the proposed MFM.

C. Proximity-coupled antenna array

As the first radiating structure, consider a two-element array antenna, excited by proximity coupling technique. Each element consists of a 2.5 mm × 21.5 mm strip, perpendicularly fed by a $1.5\lambda_0 \times 2.5$ mm line. The gap between the feed line and the strip is 1 mm, and the array elements are placed apart 6 mm. The substrate parameters are $\varepsilon_r = 1$ and $h = 1.6$ mm. The node arrangement and BCs for a single element, current density distribution at resonance and the corresponding $|S_{12}|$ are depicted in Fig. 7. For clearly visualizing the coupling of EM energy, the current density distribution is depicted in logarithmic scale.

D. Line-fed dual-polarized patch antenna

In contrast to previous cases, this case covers the microstrip discontinuity effect by connecting the feed lines to the radiating patch. For this purpose, a 10 mm ×10 mm patch is fed by two $1.5\lambda_0 \times 1.2$ mm lines from its perpendicular sides. The lines are positioned at the center of each side. The substrate parameters are $\varepsilon_r = 1$ and $h = 0.794$ mm. The nodal arrangement and BCs, current density distribution at 13.1 GHz and the corresponding $|S_{12}|$ are depicted in Fig. 8. As in the case of circular resonator, the agreement between the MFM and MoM is not satisfactory. Thus, with the same reasoning, the RCS of the structure is computed by both of the methods and reported in Fig. 8 (d).

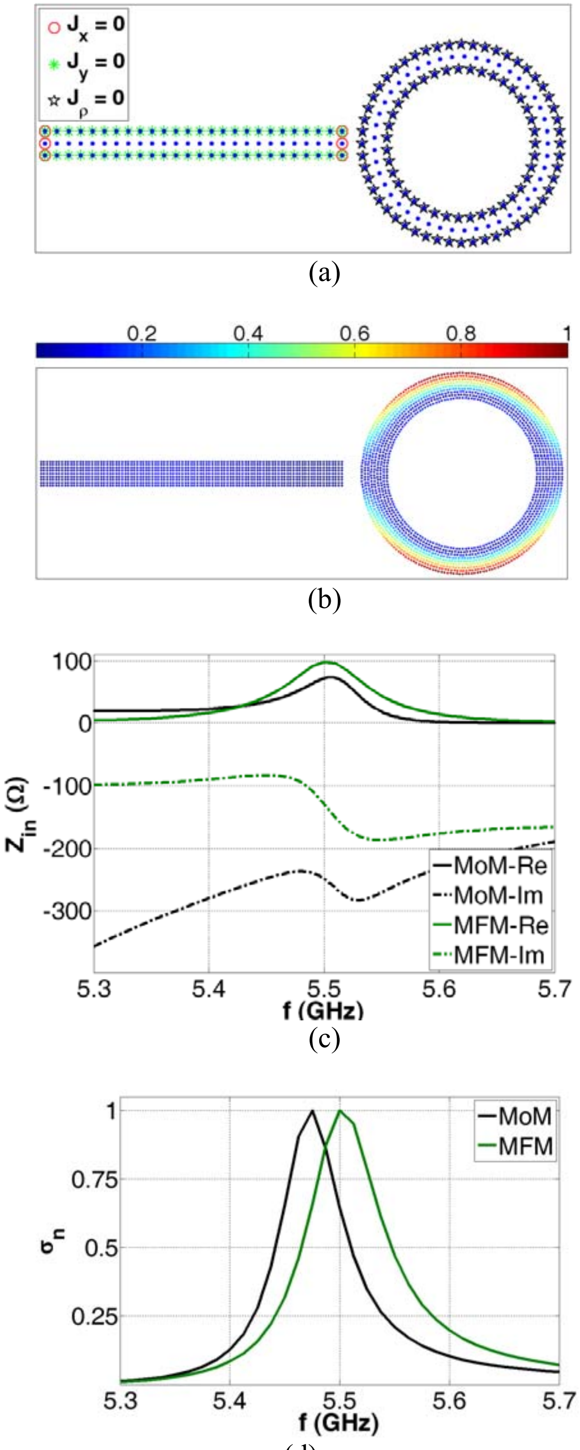

(a)

(b)

(c)

(d)

Fig. 6. Proximity-coupled circular resonator for (a) node arrangement and BCs, (b) current density distribution, (c) input impedance, and (d) normalized RCS.

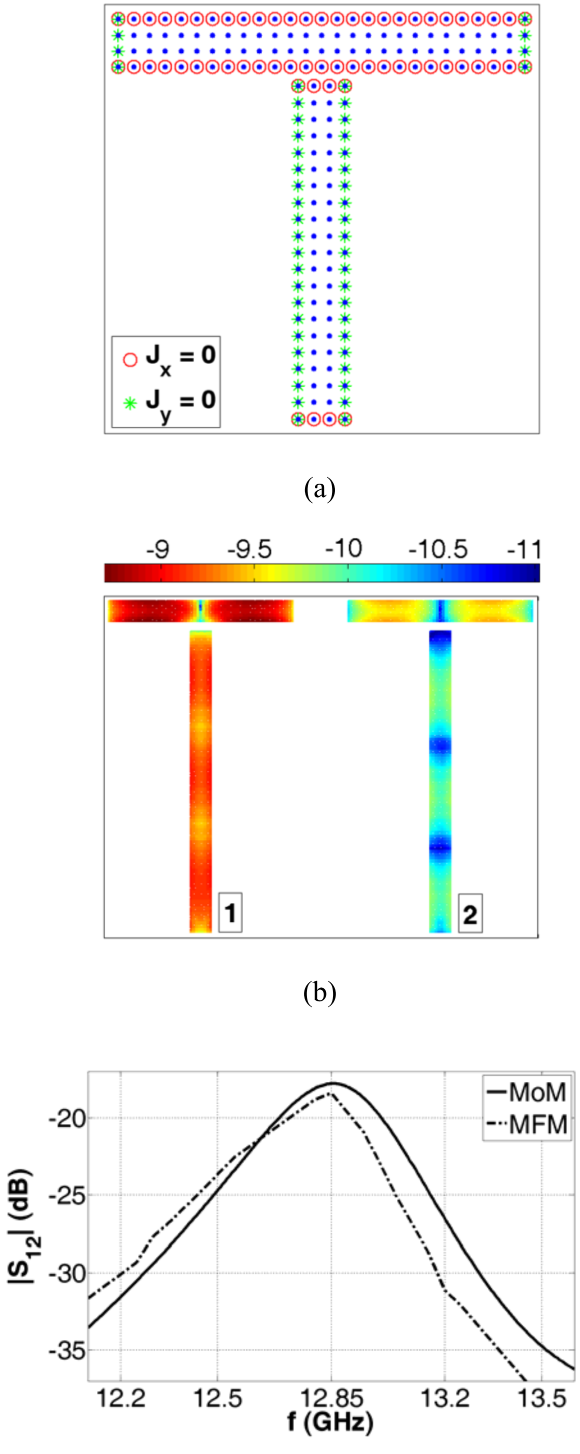

(a)

(b)

(c)

Fig. 7. Proximity-coupled antenna array for (a) node arrangement and BCs for a single element, (b) current density distribution, and (c) $|S_{12}|$.

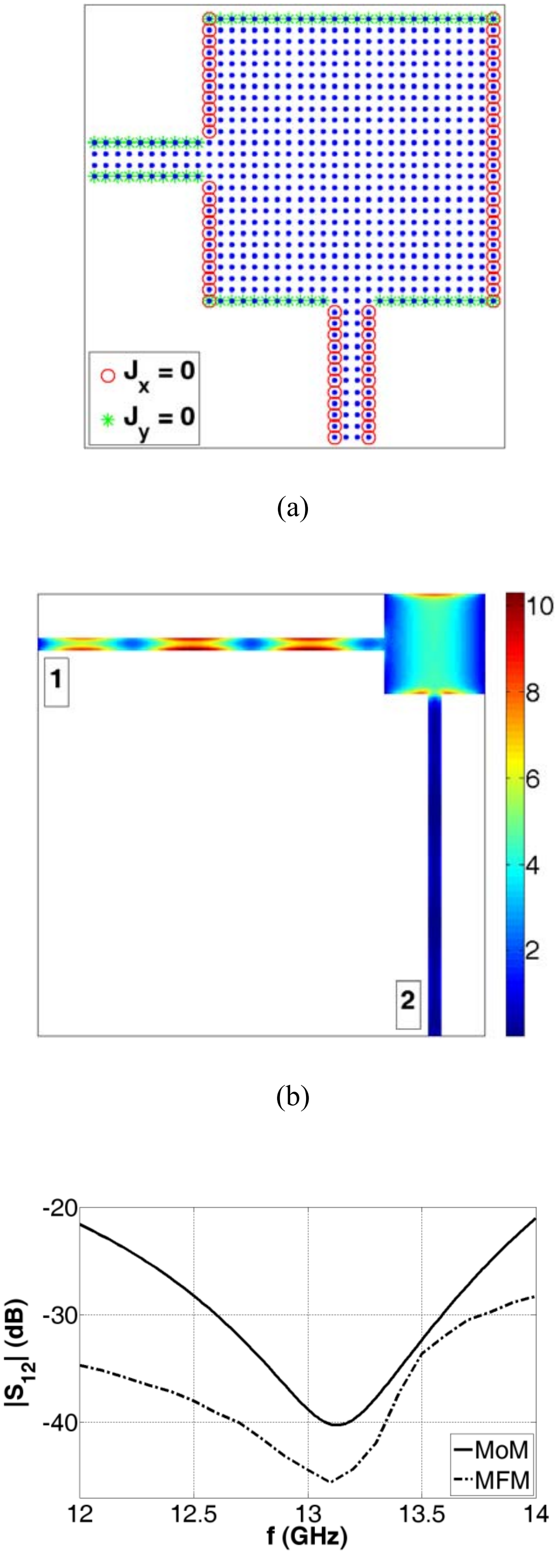

(a)

(b)

(c)

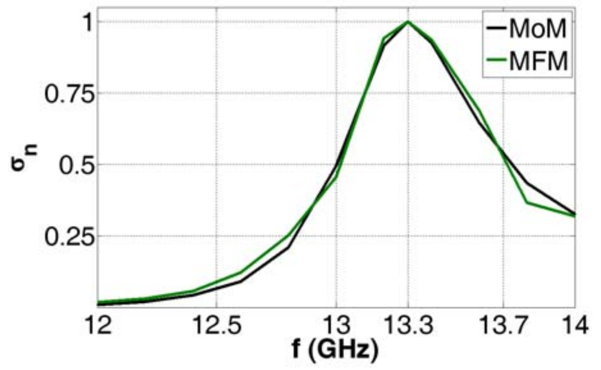

(d)

Fig. 8. Line-fed dual-polarized patch antenna for (a) node arrangement and BCs (the feeding lines are truncated for brevity.), (b) current density distribution, (c) $|S_{12}|$, and (d) normalized RCS.

E. Line-fed patch antenna

The final structure, is a 16 mm × 12.5 mm patch fed by a $1.5\lambda_0 \times 2.5$ mm line, located on a substrate with $\varepsilon_r = 2.2$ and $h = 0.794$ mm. The line is positioned on the shorter side, 7 mm apart from the corner. Computing equation (16) is carried out based on [13]. The Sommerfeld integration path (SIP) in k_{z0} and k_ρ planes and the corresponding spectral domain functions at 18.7 GHz are depicted in Fig. 9. The matrix-pencil method (MPM) is used for expansion over complex exponentials [18]. The variables t, k_{z0}, k_ρ and functions R_{TE} and R_{q} are defined based on [12]. The nodal arrangement, BCs and the $|S_{11}|$ parameter in a wide frequency range are depicted in Fig. 10. The number of unknowns, N = 2M, and the simulation time of the proposed MFM and MoM are reported in Fig. 11. For this purpose, four nodes are used for discretizing the width of the feed line in MFM analysis, which makes the simulation valid up to about 20 GHz. Similarly, the mesh frequency in MoM is set to 20 GHz. The current density distributions at deeps of $|S_{11}|$ are depicted in Fig. 12.

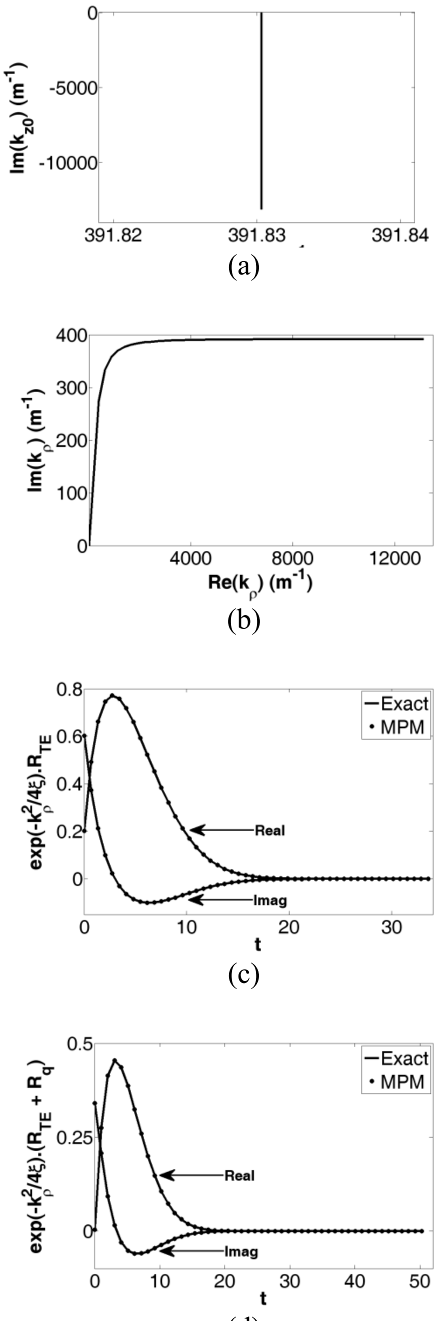

(a)

(b)

(c)

(d)

Fig. 9. Spectral domain curves at 18.7 GHz for (a) SIP in k_{z0}-plane, (b) SIP in k_ρ-plane, (c) spectrum corresponding to G_A^{xx}, and (d) spectrum corresponding to G_V .

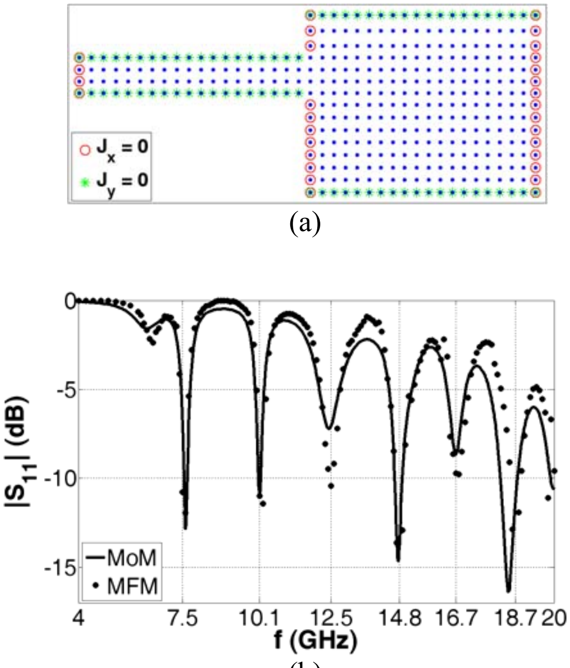

(a)

(b)

Fig. 10. Line-fed patch antenna for (a) node arrangement and BCs at 20 GHz and (b) $|S_{11}|$.

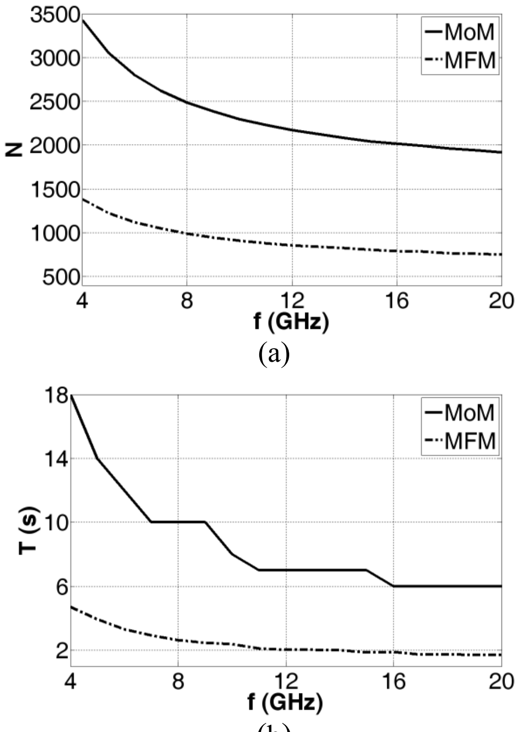

(a)

(b)

Fig. 11. Usage of computational resources for (a) number of unknowns (memory) and (b) time.

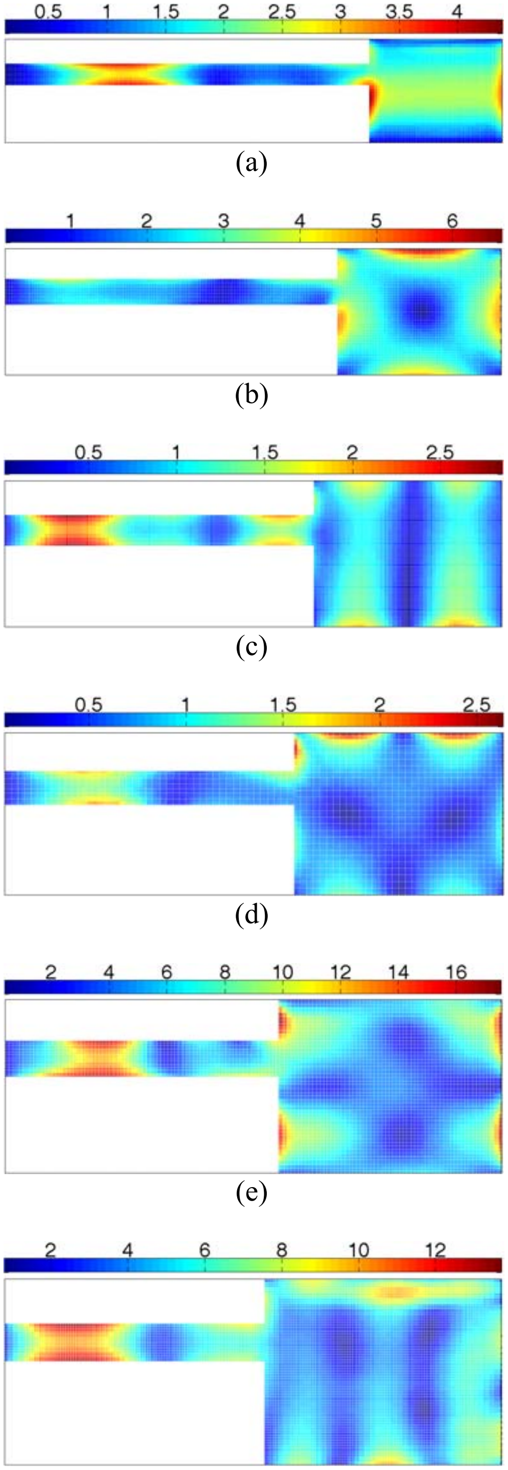

(a)

(b)

(c)

(d)

(e)

(f)

Fig. 12. Current density distribution of a line-fed patch antenna at (a) 7.5 GHz, (b) 10.1 GHz, (c) 12.5 GHz, (d) 14.8 GHz, (e) 16.7 GHz, and (f) 18.7 GHz (legends are scaled for each figure, independently.).

VIII. CONCLUSION

In this paper, five microstrip resonators/antennas are analyzed by the meshfree collocation method. The MPIE is used as the mathematical formulation of the problem. Guidelines are supplied for efficient meshless discretization leading to fast meshless integration-free solution. The proposed method is compared with MoM from the aspects of memory usage and simulation time which shows superior performance of the proposed MFM.

REFERENCES

[1] M. Zhang, L. Lingxia, P. Zhou, and X. Zhang, "A novel mesh-free method for electromagnetic scattering from a wire structure," *PIERS Online*, vol. 3, no. 6, pp. 774-776, 2007.

[2] D. Mirzaei and M. Dehghan, "A meshless based method for solution of integral equations," *Appl. Numer. Math.*, vol. 60, no. 3, pp. 245-262, 2010.

[3] W. L. Nicomedes, R. C. Mesquita, and F. J. S. Moreira, "An integral meshless-based approach in electromagnetic scattering," *COMPEL Int. J. Comput. Math. Elec. Elec. Eng.*, vol. 29, no. 6, pp. 1464-1473, 2010.

[4] W. L. Nicomedes, R. C. Mesquita, and F. J. S. Moreira, "2-D scattering integral field equation solution through an IMLS meshless-based approach," *IEEE Antennas Magn.*, vol. 46, no. 8, pp. 2873-2876, 2010.

[5] M. S. Tong and W. C. Chew, "A novel meshless scheme for solving surface integral equations with flat integral domains," *IEEE Trans. Antennas Propagat.*, vol. 60, no. 7, pp. 3285-3293, 2012.

[6] S. J. Lai, B. Z. Wang, and Y. Duan, "Meshless radial basis functions method for solving hallen's integral equation," *Appl. Comp. Electro. Society (ACES) Journal*, vol. 27, no. 1, pp. 9- 13, 2012.

[7] B. Honarbakhsh and A. Tavakoli, "Numerical solution of electromagnetic integral equations by the meshfree collocation method," *Appl. Comp. Electro. Society (ACES) Journal*, vol. 27, no. 9, pp. 706-716, 2012.

[8] R. F. Harrington, *Field Computation by Moment Methods*, New York: Macmillan, 1968.

[9] R. Mosig, "Arbitrary shaped microstrip structures and their analysis with a mixed potential integral equation," *IEEE Trans. Microwave Theory Tech.*, vol. 36, no. 2, pp. 314-323, 1988.

[10] G. R. Liu and Y. T. Gu, *An Introduction to MeshFree Methods and Their Programming*, Springer, 2005.

[11] D. Shepard, "A two dimensional interpolation function for irregularly spaced data," *Proc. 23rd Nat. Conf. ACM*, pp. 517-523, 1968.

[12] Y. L. Chow, J. J. Yang, D. G. Fang, and G. E. Howard, "A closed-form spatial Green's function for the thick microstrip substrate," *IEEE Trans. Microwave Theory Tech.*, vol. 39, no. 3, pp. 588-592, 1991.

[13] M. Yuan, T. K. Sarkar, and M. Salazar-Palma, "A direct discrete complex image method from the closed-form Green's functions in multilayered media" *IEEE Trans. Microwave Theory Tech.*, vol. 54, no. 3, pp. 1025-32, 2006.

[14] M. G. Duffy, "Quadrature over a pyramid or cube of integrands with a singularity at a vertex," *SIAM J. Numer. Ana.*, vol. 19, pp. 1260-1262, 1982.

[15] D. H. Schaubert, "A review of some microstrip antenna characteristics," D. M. Pozar and D.H. Schaubert, *Microstrip Antennas,* IEEE Press, 1995.

[16] J. C. Rautio, "A De-embedding Algorithm for Electromagnetics," *Int. J. MIMICAE*, vol. 1, no. 3, pp. 282-287, 1991.

[17] T. K. Sarkar, Z. A. Maricevic, and M. Kahrizi, "An accurate de-embedding procedure for characterizing discontinuities," *Int. J. MIMICAE*, vol. 2, no. 3, pp. 135-143, 1992.

[18] T. K. Sarkar and O. Pereira, "Using the matrix pencil method to estimate the parameters of a sum of complex exponentials," *IEEE Antennas Propagat. Mag.*, vol. 37, no. 3, pp. 48-55, 1995.

Babak Honarbakhsh was born in Tehran, Iran. He received his B.Sc. and M.Sc. degrees in Electrical Engineering from Amirkabir University of Technology where he is currently working toward his Ph.D. degree. His current research interest is numerical solution of electromagnetic problems by meshfree methods.

Ahad Tavakoli was born in Tehran, Iran, on March8, 1959. He received the B.S. and M.S. degrees from the University of Kansas, Lawrence, and the Ph.D. degree from the University of Michigan, Ann Arbor, all in electrical engineering, in 1982, 1984, and 1991, respectively. In 1991, he joined the Amirkabir University of Technology, Tehran, Iran, where he is currently a Professor in the Department of Electrical Engineering. His research interests include EMC, scattering of electromagnetic waves and microstrip antennas.

A Method to Reduce the Back Radiation of the Folded PIFA Antenna with Finite Ground

Yan Li, Peng Yang, Feng Yang, and Shiquan He

Department of Microwave Engineering
University of Electronic Science and Technology of China, Chengdu, 611731, China
liyaanem@gmail.com, yangpeng@uestc.edu.cn, yangf@uestc.edu.cn, and shiquanhe1984@gmail.com

Abstract **─** A novel method, named the resistors and inductors loading, is proposed in this paper to reduce the back radiation of the folded PIFA antenna with finite ground. With different loading schemes (i.e., resistors loading, inductors loading, and resistors and inductors loading), variable reduced back radiation and gain can be achieved. However, there is a compromise between the gain and back radiation and it can be chosen based on the specified applications. A prototype with resistors loading is fabricated and measured to verify the proposed design. Measured results agree well with the simulated results.

Index Terms - Back radiation, folded PIFA antenna, and resistors and inductors loading.

I. INTRODUCTION

Microstrip antennas have been widely used in modern mobile and wireless communication systems because of their significant advantages, such as the light weight, low profile, and low cost. Conventional microstrip antennas, operating at their fundamental mode (TM_{10} or TM_{01}), have an electrical length of about half wavelength and it is too large for many applications operating at lower frequencies such as portable UHF RFID reader antennas. Some techniques have been proposed to miniaturize the antenna size, such as the meandered patch, with high dielectric constant, PIFA antennas, meander PIFA antenna, the capacitive loading, the folded strip antenna, and the folded shorted-patch antenna [1-5]. However, the size of the ground plane is not considered in all of these methods, which can significantly affect the performances of the microstrip antenna. It is apparent that if the size of the ground plane is small, the gain will decrease and the back lobe will increase. As the size of the ground plane reduces, the currents on the edge of the ground plane increase and these currents result in a deceased front-to-back ratio of a patch antenna [6]. So the total size of the mcirostrip antenna should be determined by the size of the ground plane rather than the patch. Though some methods have been proposed recently to improve the front-to-back ratio of microstrip antennas [6, 7], a large ground plane is still employed. In [8], back radiation of the antenna is reduced by the resistors loading with a lower antenna gain.

A novel method, named the resistors and inductors loading, is proposed in this paper to improve the front to back ratio of the antennas with compact ground plane. The folded PIFA antenna is employed here to reduce the antenna size [4]. Compared with the method depicted in [6, 7], back radiation is reduced significantly in the proposed design while a compact ground plane is still remained. As can be seen, there is a compromise between the gain and the back radiation with different inductors and resistors loading schemes and it can be chosen according to the specified applications, so the proposed antenna in this paper have more freedom than the antenna presented in [8] and this antenna can also be considered as a reconfigurable antenna.

II. CONFIGURATIONS OF THE PROPOSED ANTENNA

A conventional folded PIFA antenna is shown in Fig. 1 and the dimensions of the antenna are shown in Table 1. It works at the UHF RFID band and the centre frequency of 915 MHz. This

Submitted On: Sep. 10, 2012
Accepted On: Jan. 3, 2013

antenna suffers large back radiations because of the small ground size. A novel configuration is proposed in this paper to reduce the back radiation of the antenna. As shown in Fig. 2 (a), four inductors and resistors are loaded on the ground plane. Back radiation of the proposed antenna can be largely reduced by tuning values of the loaded inductors and resistors. The operating frequency of this antenna is determined by lp_0 and lp_1, as shown in Fig. 2 (b). The dimensions of the proposed antenna and the optimized values of the loaded elements are all shown in Table 2. Figure 2 (c) demonstrates the simulated model of the proposed antenna.

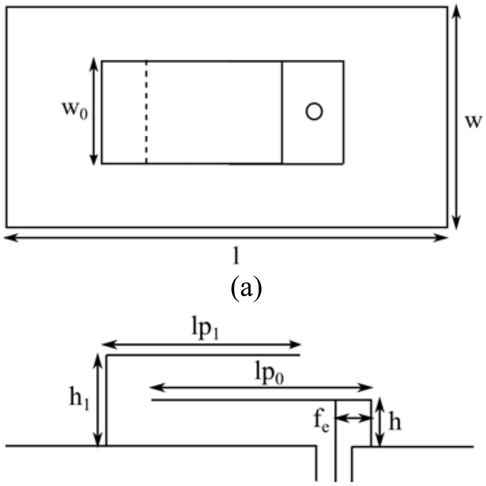

(a)

(b)

Fig. 1. The original configuration: (a) front view and (b) cross-section of the proposed antenna.

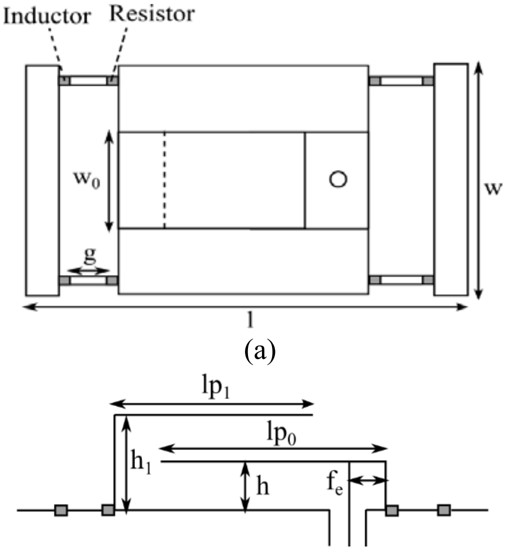

(a)

(b)

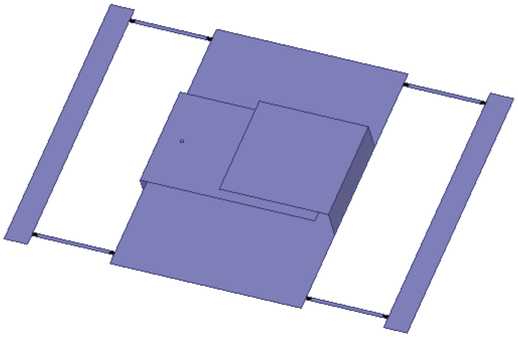

(c)

Fig. 2. Configuration of the proposed structure (a) front view, (b) cross-section, and (c) simulated model of the proposed antenna.

Table 1: Dimensions of the original patch.

l	120 mm	lp_0	52 mm
w	80 mm	lp_1	32.5 mm
h	5 mm	f_e	9 mm
h_1	10 mm	w_0	30 mm

Table 2: Dimensions and values of the loading elements of the proposed patch.

l	120 mm	lp_0	52 mm
w	80 mm	lp_1	32.5 mm
h	5 mm	f_e	6.5 mm
h_1	10 mm	g	24.5 mm
R	50 Ohm	w_0	30 mm
L	7 nH		

III. EXPLANATION AND SIMULATION OF THE PROPOSED ANTENNA

The working principle of the proposed antenna is discussed in this section. The induced equivalent magnetic currents (**M_1** and **M_2**) [9] on the edges of the finite ground plane, as shown in Fig. 3 (a), contribute not only to the antenna gain but also to the back radiation. Because of the size of the ground plane of the original antenna, which is only 0.39 λ_0 × 0.24 λ_0, which is even smaller than a conventional air substrate microstirp antenna, it is apparent that the induced equivalent magnetic current can be very large due to the small ground size. As shown in Fig. 3 (b), because of the large electric field on the edges of the ground plane, the induced equivalent magnetic currents will be very large, which are obtained according to the formula,

$$\mathbf{M} = -\mathbf{n} \times \mathbf{E} . \qquad (1)$$

Inductors and resistors are loaded on the ground plane in this paper to reduce the back radiation of the traditional fold PIFA antenna. As shown in Fig. 4 (a), the induced equivalent magnetic currents $\mathbf{M_1}$, $\mathbf{M_2}$, and $\mathbf{M_3}$ can be considered as a three-element antenna array. By controlling the amplitude and phase of $\mathbf{M_1}$, $\mathbf{M_2}$, and $\mathbf{M_3}$, the field produced by them will cancel each other in some directions and the back radiation can be reduced. Simulated electric field distribution on the edge of the ground plane of the proposed antenna is shown in Fig. 4 (b). Here, the resistors are used to control the amplitudes of each element while the inductors and gaps are used to control the phases of each element.

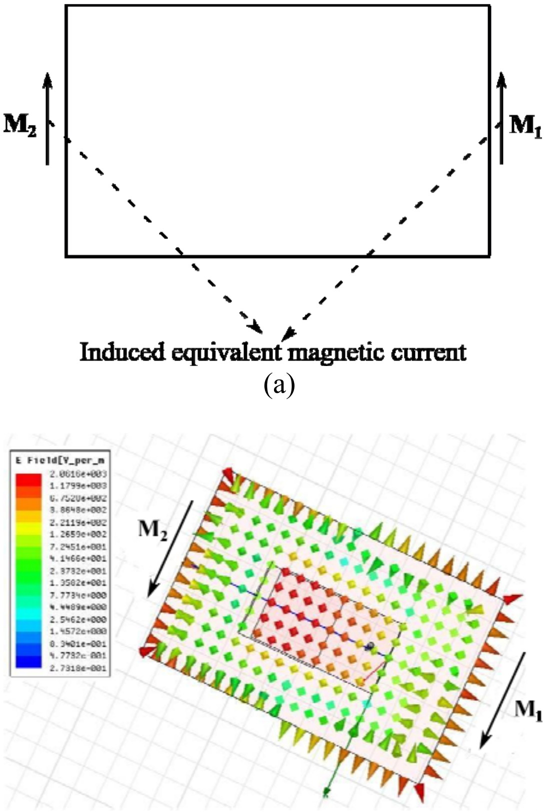

(a)

(b)

Fig. 3. Conventional folded-short patch antenna, showing induced equivalent magnetic currents on the ground plane: (a) induced equivalent magnetic currents and (b) simulated electric filed distribution.

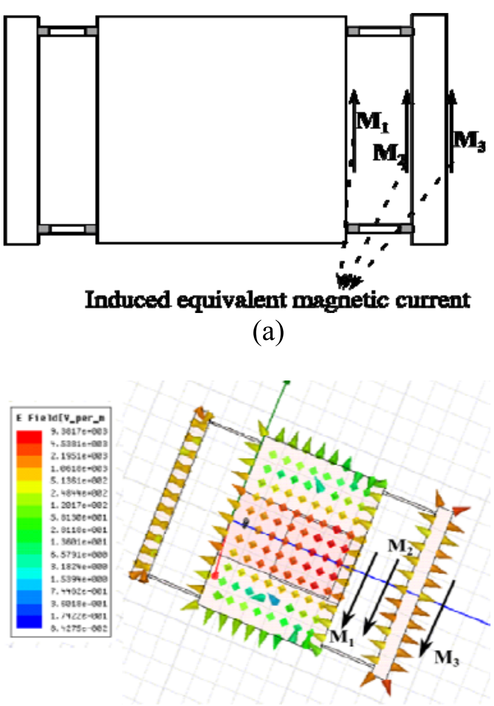

(a)

(b)

Fig. 4. Proposed folded-short patch antenna, showing induced equivalent magnetic currents on the ground plane: (a) induced equivalent magnetic currents and (b) simulated electric filed distribution.

The proposed antenna is simulated using an in-house full-wave electromagnetics solver based on the EFIE (Electric Field Integral Equation) and the magnetic frill source. The simulated radiation patterns with and without loadings are shown in Figs. 5 and 6, respectively. More details about the gain, the back radiation, and the front-to-back ratio are shown in Table 3. The optimized dimensions of the gap and values of inductors and resistors are shown in Table 2. They are obtained by the trial-and-error method.

Table 3: Performance comparison with different loading.

	Gain	Back Radiation	Front-to-Back Ratio
Original	4.65 dB	-0.51 dB	5.16 dB
R loading	3.86 dB	-11.42 dB	15.28 dB
L loading	5.08 dB	-5.61 dB	10.69 dB
R and L loading	3.41 dB	-26.23 dB	29.64 dB

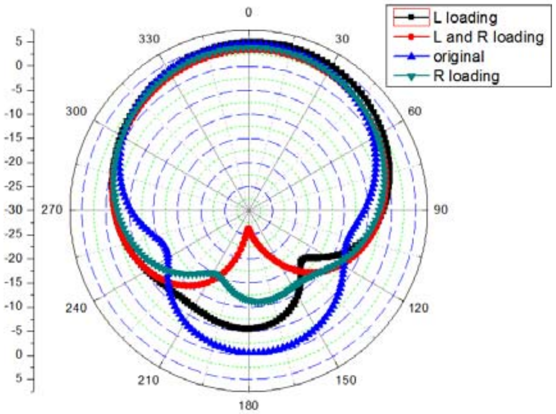

Fig. 5. Radiation pattern of E plane at 915 MHz.

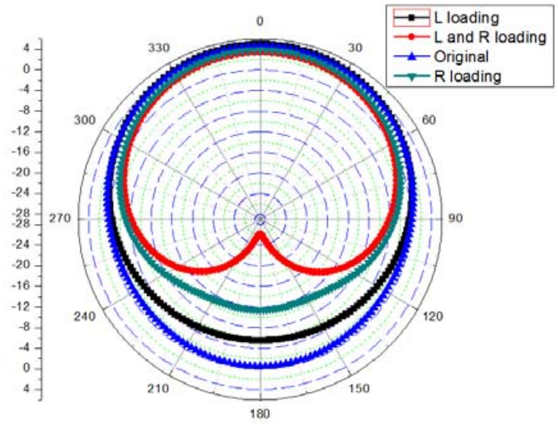

Fig. 6. Radiation pattern of H plane at 915 MHz.

Table 3 shows that if both resistors and inductors are loaded, the back radiation is reduced significantly. The front-to-back ratio is 29.64 dB, which is 24.48 dB higher than the conventional one. However, the gain deceases slightly. It is 1.24 dB lower than the conventional one because of the resistive loss. If only inductors are loaded on the ground plane, the front-to-back ratio is enhanced by 5.53 dB and the gain increases slightly. Meanwhile, if only resistors are loaded on the ground plane, the front-to-back ratio is enhanced by 10.8 dB, while the gain decreases, which is also because of the resistive loss. By slightly changing the feeding position (f_e), all the antennas can be matched to 50 Ohms easily. The S_{11} without loading or with different loadings schemes is shown in Fig. 7.

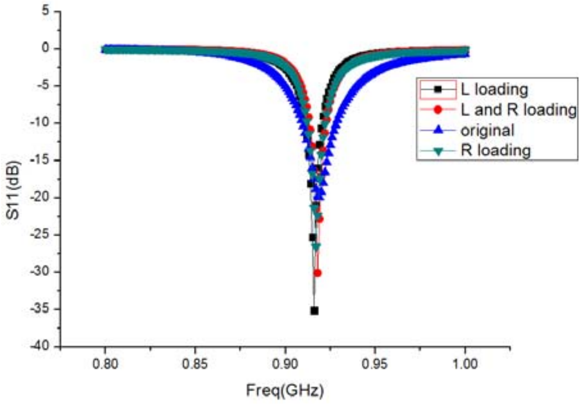

Fig. 7. Simulated S_{11} of the proposed antennas.

From the analysis above, it is found that there is a compromise between the antenna gain and the back radiation with different loading schemes. By changing the values of the loaded components, different antenna gain and back radiation can be obtained and it depends on specified applications.

IV. EXPERIMENTAL RESULTS

To verify the performance of the proposed antenna, a prototype of the design with resistors loading only was fabricated and measured. The fabricated prototype is shown in Fig. 8. Four 50 Ohm resistors are loaded on the ground plane to reduce the back radiation. The measured S_{11} and radiation patterns are shown in Figs. 9 and 10, respectively. Both of them have a good agreement with the simulated results.

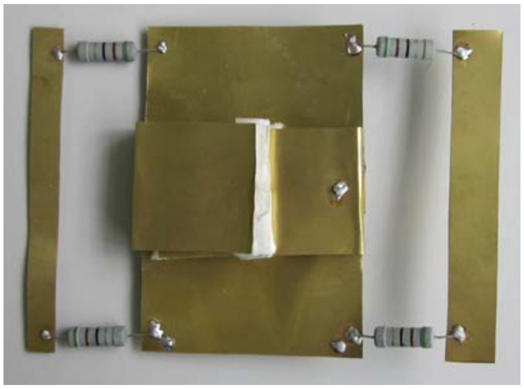

Fig. 8. Photograph of the fabricated prototype.

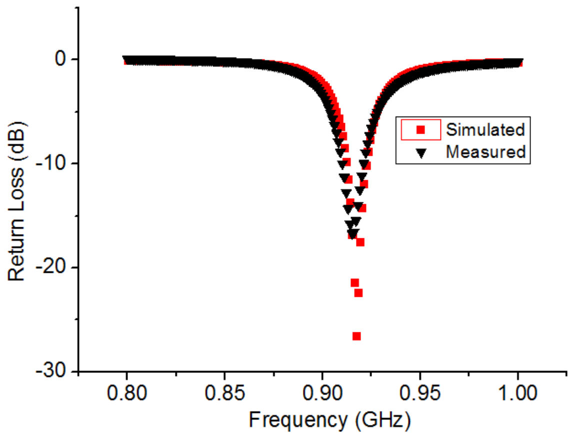

Fig. 9. Measured $|S_{11}|$ of the proposed antenna with resistors loading only.

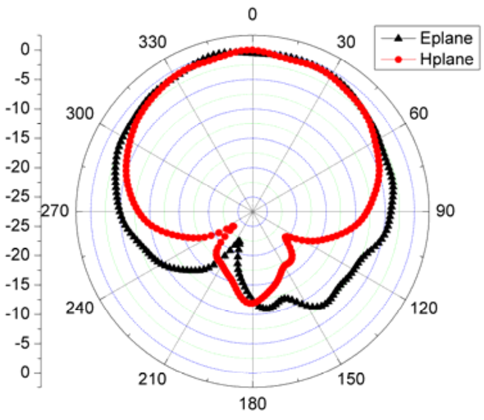

Fig. 10. Measured radiation pattern of the proposed antenna with resistors loading only.

VI. CONCLUSIONS

In this paper, the ground plane of the folded PIFA antenna is loaded with resistors and inductors to reduce the back radiation. By the resistors and inductors loading, the back radiation is reduced dramatically, which is 25.72 dB lower than the conventional counterpart, while the antenna gain decreases slightly. However, there is a compromise between the gain and back radiation. Different inductors and resistors loading schemes can be chosen according to the specified applications. For example, if the back radiation is of greater concern, resistors and inductors loading should be employed. If the antenna gain is more emphasized, the inductors loading should be chosen.

ACKNOWLEDGMENT

This work was supported in part by "The Fundamental Research Funds for the Central Universities" and in part by the Innovation Research Funds of Academy of Space Information System and in part by the Natural Science Foundation of China (No. 11176007 and No.61001029).

REFERENCES

[1] K.-L. Wong, *Compact and Broadband Microstrip Antennas*, John Wiley & Sons, INC, 2002.

[2] J. Noh, M. Heo, and J. Jeon, "Meandered planar inverted F-antenna for PCS mobile phone," *IEEE/ACES International Conference on Wireless Communications and Applied Computational Electromagnetics*, Honolulu, Hawaii, April 2005.

[3] Q. Rao, G. Wen, and D. Wang, "A multiple folded strip antenna for handset devices," *24th Annual Review of Progress in Applied Computational Electromagnetics (ACES)*, Niagara Falls, Canada, pp. 174-177, March-April 2008.

[4] R. Li, G. DeJean, M. M. Tentzeris, and J. Laskar, "Development and analysis of a folded shorted-patch antenna with reduced size," *IEEE Trans. Antennas Propagat.*, vol. 52, no. 2, pp. 555-562, March 2004.

[5] A. Holub and M. Polivka, "A novel microstrip patch antenna miniaturization technique: a meanderly folded shorted-patch antenna," 14th *Microwave Techniques, COMITE*, pp. 1-4, 2008.

[6] T. J. Cho and H. M. Lee, "Front-to-back ratio improvement of a microstrip patch antenna by ground plane edge shaping," *Antennas and Propagation Society International Symposium (APSURSI)*, pp. 1-4, 2010.

[7] H.-M. Lee and J.-k. Kim, "Front-to-back ratio improvement of a microstrip patch antenna using an isolated soft surface structure," *Proceedings of the 39th European Microwave Conference*, Rome, Italy, pp. 385-388, Sep.-Oct., 2009.

[8] Y. Li, S. Sun, L. Jiang, P. Yang, and S. He, "Back radiation reduction of the folded shorted-patch antenna using finite ground strips with resistive loads," *28th Annual Review of Progress in Applied Computational Electromagnetics (ACES)*, Columbus, Ohio, pp. 795-799, April 2012.

[9] T. Namiki, Y. Murayama, and K. Ito, "Improving radiation-pattern distortion of a patch antenna having finite ground plane", *IEEE Trans. Antennas Propagat.*, vol. 51, no. 3, pp. 478-482, March 2003.

Yan LI was born in Shaanxi, China. He received the B.Sc. degree in Electronic Engineering and M.Sc. degree in Electromagnetics and Microwave Technology from the University of Electronic Science and Technology of China (UESTC) in 2007 and 2010, respectively, where he is currently working toward the Ph. D. degree. From Feb. 2010 to Aug. 2011, he was a Research Assistant with the Department of Electrical and Electronic Engineering at the University of Hong Kong. His research interests include antenna theory and design, antenna array optimization, and passive microwave circuits design.

Peng YANG was born in Kunming, Yunnan, China. He received the B.Sc. degree in Electronic Engineering in 2001, M.Sc. degree and Ph.D. degree in Electromagnetics and Microwave Technology from the University of Electronic Science and Technology of China (UESTC) in 2008 and 2011, respectively. From Jan. 2009 to Nov. 2010, he was a Research Assistant with the Department of Electrical and Electronic Engineering at the University of Hong Kong. He is currently a lecture in the University of Electronic Science and Technology of China. His research interests include microstrip antenna theory and design, metameterials, and smart antenna systems.

Feng YANG was born in Shaanxi, China. He received the M.Sc. degree and Ph.D. degree in Electromagnetics and Microwave Technology from the University of Electronic Science and Technology of China, Chengdu, China, in 1995 and 1998, respectively. He is currently a Professor in the Department of Microwave Engineering, University of Electronic Science and Technology of China. He has published more than 90 journal papers. His research interests include antenna theory and techniques, electromagnetic scattering and inverse scattering, and UWB communication

Shiquan HE was born in Sichuan, China, and in1984. He received the B.S. degree and Ph.D. in Electromagnetic and Microwave Technology from the University of Electronic Science and Technology of China, Chengdu, China, in 2006 and 2011 respectively. Since October 2009, he has been a Visiting Researcher in the Electromagnetics and Optics Research Group, Department of Electrical and Electronic Engineering, the University of Hong Kong, Hong Kong. He is currently a lecture in the University of Electronic Science and Technology of China. His research interests include finite element methods, integral equation methods, and fast algorithms in computational electromagnetics.

Low-Profile Broadband Top-Loaded Triangular Antenna with Folded Rim

Naobumi Michishita, Woo-Jin Kim, and Yoshihide Yamada

Department of Electrical and Electronic Engineering
National Defense Academy, Yokosuka, 239-8686 Japan
naobumi@nda.ac.jp

Abstract **─** This paper presents the impedance matching technique and the bandwidth characteristics of a low-profile top-loaded triangular antenna with oblique shorting pins. The folded rim is arranged at the edge of the finite ground plane. The bandwidth diagrams for various antenna heights, finite sizes of the ground plane, and the widths of the folded rim are obtained through the moment-method simulation. The maximum bandwidth of 43 % is achieved with 0.05 λ height. For the low-profile configuration, the bandwidth of 17 % is obtained with 0.03 λ height.

Index Terms – Broadband, folded rim, low profile, moment method, and top-loaded triangular antenna.

I. INTRODUCTION

A radio-on-fiber system has been developed for enabling cellular mobile communication in radio-blind areas, such as highway tunnels and underground shopping malls [1]. A distributed antenna system consisting of coaxial cables and couplers has been specifically designed for use in the aforementioned radio-blind areas [2]. In an in-building antenna distribution system, the antenna is installed on the ceiling, and hence a low-profile antenna is preferred.

A top-loaded monopole antenna (TLMA) has been developed for use as a low-profile antenna. The TLMA that is arranged with a shorting cylinder or pins has a feature of low profile and vertical polarization antenna by exciting TM_{01} mode [3]. In typical example for the application of mobile communication, a disc-loaded monopole array antenna with electrically steerable beam has been proposed for diversity technique and reducing multipath or interference [4]. For bandwidth enhancement of the low-profile antenna, a triple-ellipse inverted-hat antenna has been proposed [5]. The bandwidth over 160 % can be achieved at an antenna height of 0.1 λ at the lowest frequency. For obtaining the TM_{01} mode with low-profile configuration, a disc-ring dielectric resonator antenna has been presented [6]. A 47 % bandwidth is achieved at an antenna height of 0.2 λ.

For achieving simple configuration, triangular or trapezoidal plates are used as the radiating elements for the TLMA [7]. Based on them, the TLMA was designed with clarified impedance-matching techniques showing the bandwidth characteristics of the TLMA with oblique shorting pins [8]. Moreover, the effects of a folded rim at the edge of a finite ground plane are also clarified to reduce the antenna height for the low-profile TLMA [9]. However, the optimum width of the folded rim has not been obtained at each size of the ground plane when the antenna height is less than 0.05 λ.

This paper presents the impedance matching and bandwidth characteristics of the low-profile top-loaded triangular antenna (TLTA) on a finite ground plane. To clarify the effect of the folded rim to the bandwidth enhancement at various antenna heights, the moment-method simulation is employed. And, the bandwidth diagrams for various sizes of the ground plane and the widths of the folded rim are investigated when the antenna height is less than 0.05 λ.

Submitted On: Aug. 31, 2012
Accepted On: Dec. 26, 2012

II. IMPEDANCE MATCHING TECHNIQUE USING OBLIQUE SHORTING PINS

Figure 1 shows the configuration and structural parameters of the TLTA with the folded rim. The TLTA comprises a triangular radiation element, a top-loaded capacitance disk, and oblique shorting pins on a finite ground plane as shown in Fig. 1 (a). Since the proposed antenna is fed against a ground plane at a center feed point, the antenna is operated as a monopole [10]. The antenna model has been designed using the electromagnetic simulation based on the moment method. The TLTA is designed to operate at a frequency of 2 GHz. The conductor thicknesses of the finite ground plane and side walls are 1.0 mm and 0.2 mm, respectively. The conductor thicknesses of the disk and the radiation element are 0.6 mm each. Wires of radius 0.5 mm are used as shorting pins. R_g is the radius of the finite ground plane and h is the height of antenna. The height of the rim is equal to h, while L_{ring} is the width of the upper part of the folded rim.

Figure 2 shows the optimum parameters for the impedance matching of the TLTA with four shoring pins. Usually, the location of the arrangement of the shorting pins affects the impedance matching of the TLTA. The oblique angle of the shorting pins is added as the structural parameters for impedance matching of the low-profile TLTA. D_x and D_y are the oblique angles that are inclined to x and y axes, respectively. R_g, D_x and D_y increase as h decreases and, D_x and D_y are separately tuned.

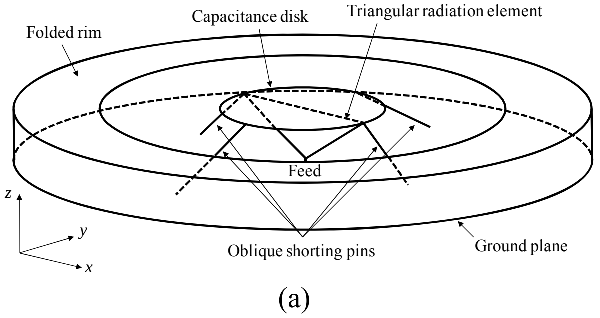

(a)

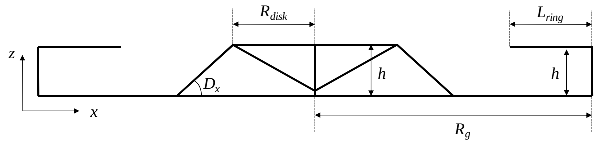

(b)

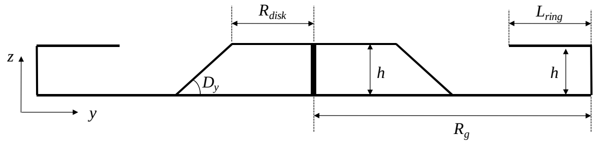

(c)

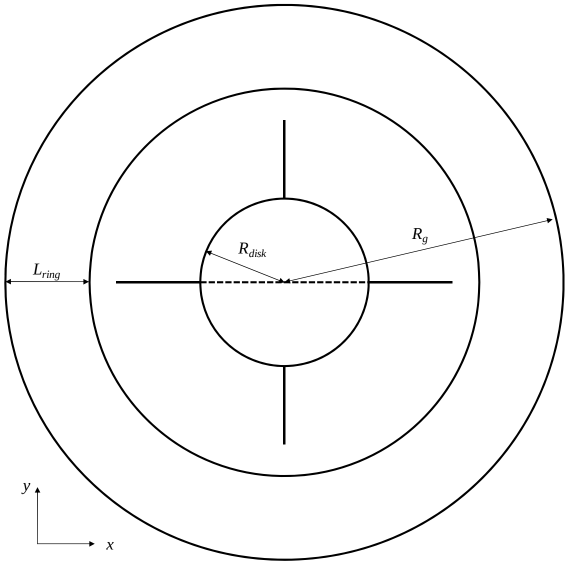

(d)

Fig. 1. Configuration of a top-loaded triangular antenna with folded rim from a (a) perspective view, (b) side view in the *ZX* plane, (c) side view in *YZ* plane, and (d) top view in *XY* plane.

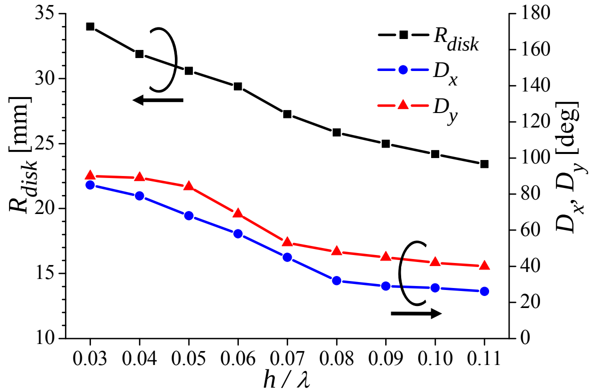

Fig. 2. Optimum parameters for impedance matching of the top-loaded triangular antenna without a folded rim.

III. LIMITATION OF BANDWIDTH ENHANCEMENT USING SIDE RIM

The side rim installed at the edge of the finite ground plane is designed for broadband at the low profile. The folded rim is eliminated from the configuration of the TLTA model as shown in Fig. 1. Figure 3 shows the S_{11} characteristics of the TLTA with/without the side rim at $h = 0.1\lambda$ and $R_g = 0.55\lambda$. The resonant frequency of the TLTA without the side rim is 1.8 GHz. When the side rim is installed, dual resonance is observed at 1.7 GHz and 2.1 GHz, and is expected to achieve broadband characteristics.

Figure 4 shows the bandwidth diagrams for various heights of the side rim and radius of the finite ground plane. The bandwidth is calculated for VSWR ≤ 2. The effect of the side rim is pronounced at $R_g = 0.44\lambda$. A sharp variation in the bandwidth is observed when $h = 0.04\text{-}0.1\lambda$, and this variation becomes maximum at $h = 0.07\lambda$. However, the variation in the bandwidth observed at $R_g = 0.48\lambda$ is less than that observed at $R_g = 0.44\lambda$. The maximum bandwidth appears at $h = 0.1\lambda$. Moreover, it shows little effect when $R_g = 0.56\lambda$. In other words, the effect of the side rim is suppressed with an increase in the size of the finite ground plane. Therefore, the bandwidth more than 45 % is observed at $0.07\ \lambda < h < 0.1\ \lambda$. When the antenna height is less than $0.04\ \lambda$, impedance matching cannot be achieved.

Figure 5 shows the maximum bandwidth characteristics of the TLTA with/without the side rim when h is varied. Both maximum bandwidth increases as h increases. The maximum bandwidth of the TLTA with the side rim becomes 13 % broader than that without the side rim at around $h = 0.1\lambda$. The arrangement of the side rim becomes less effective as h decreases and has no effect at $h < 0.04\ \lambda$.

IV. BANDWIDTH ENHANCEMENT FOR LOW-PROFILE ANTENNA USING FOLDED RIM

To achieve the broadband characteristics at $h \leq 0.05\ \lambda$, the folded rim is arranged at the edge of the TLTA, and its effect is examined. Figure 6 shows the S_{11} characteristics at $h = 0.05\ \lambda$. The first resonant frequency at around 1.7 GHz becomes the lower frequency as L_{ring} increases. And L_{ring} affects the impedance matching for the second resonant frequency at around 2.3 GHz. Since the maximum bandwidth can be obtained from the optimum radius of the finite ground plane as shown in Fig. 5, R_g and L_{ring} are adjusted to achieve broadband characteristics for the TLTA with folded rim.

Figure 7 shows the current distributions of the TLTA with the folded rim at $h = 0.05\ \lambda$ and $L_{ring} = 0.14\ \lambda$. The currents at the feeding triangular element and the folded rim flow in phase at the lower resonant frequency of 1.85 GHz and out of phase at the higher resonant frequency of 2.45 GHz, respectively.

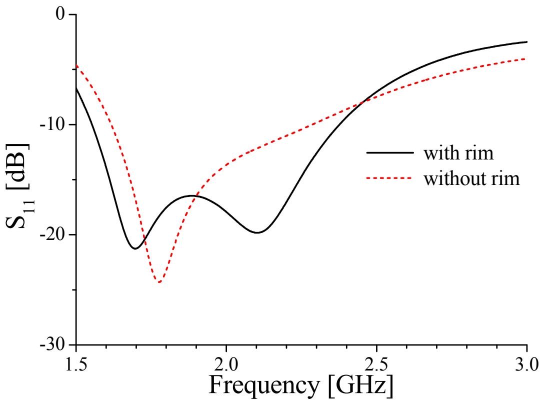

Fig. 3. The S_{11} characteristics of top-loaded triangular antenna with/without side rim.

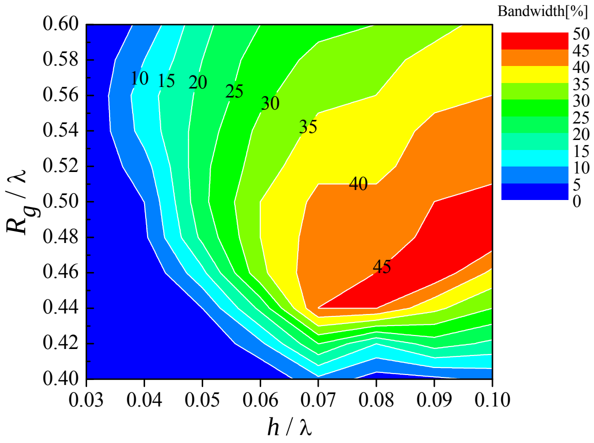

Fig. 4. Bandwidth characteristics of the top-loaded triangular antenna with side rim, when h and R_g are varied.

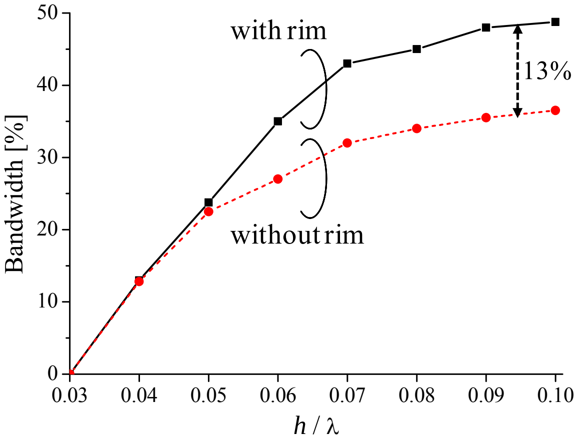

Fig. 5. Maximum bandwidth characteristics of the top-loaded triangular antenna with side rim when *h* is varied.

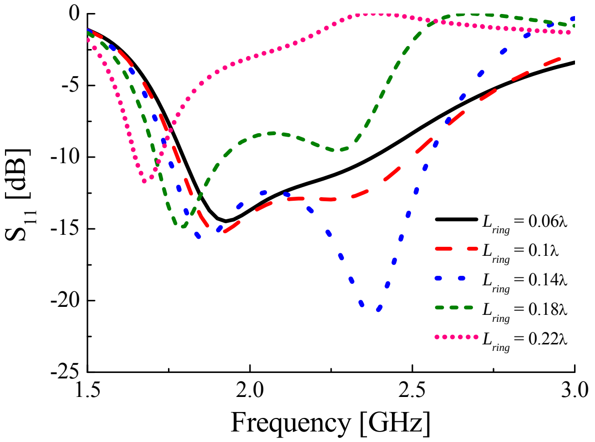

Fig. 6. The S_{11} characteristics of the top-loaded triangular antenna with folded rim at *h* = 0.05 λ.

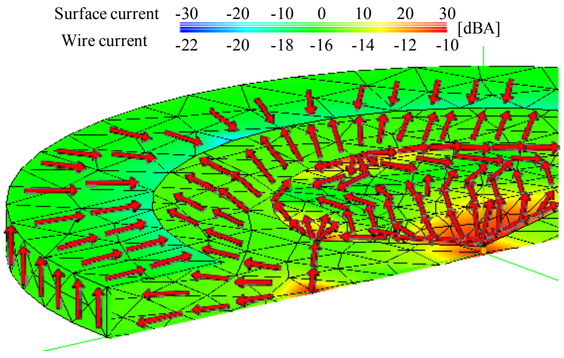

(a)

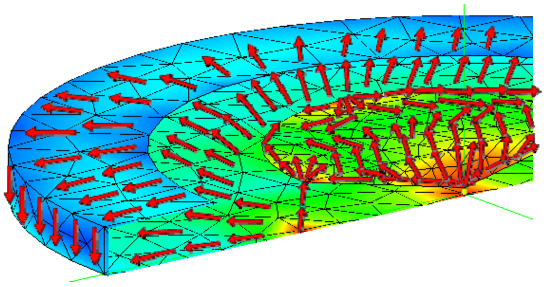

(b)

Fig. 7. Current distributions of the top-loaded triangular antenna with a folded rim at *h* = 0.05λ for (a) 1.85 GHz and (b) 2.45 GHz.

Figure 8 shows the bandwidth characteristics for the variable R_g, L_{ring}, and *h*. After adjusting R_g and L_{ring} at each *h*, the maximum values of the bandwidth are 43 %, 31 %, and 17 % at *h* = 0.05λ, 0.04 λ, and 0.03 λ, respectively. In addition, optimum values of L_{ring} can be selected only on a narrow range when R_g is small. The effect of L_{ring} becomes insensitive as R_g increases.

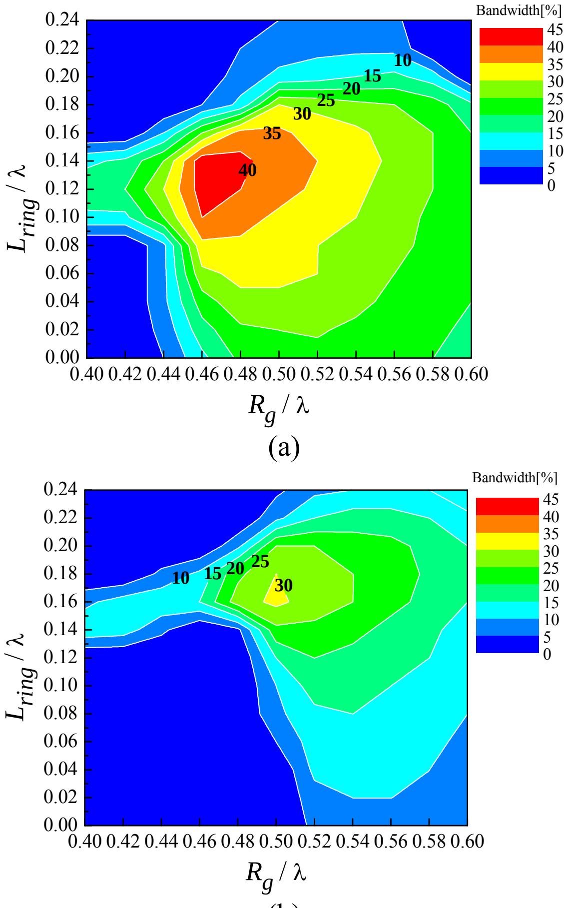

(a)

(b)

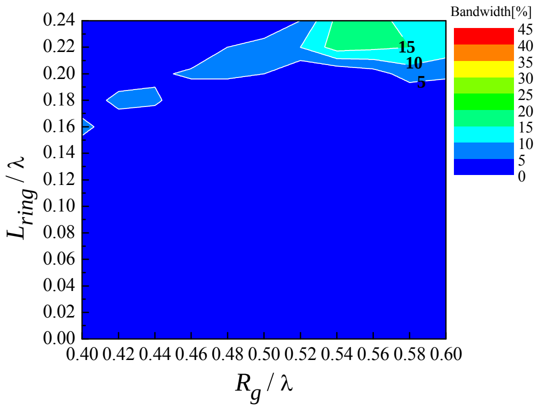

(c)

Fig. 8. Bandwidth characteristics of the top-loaded triangular antenna with folded rim when R_g and L_{ring} are varied at (a) h = 0.05 λ, (b) h = 0.04 λ, and (c) h = 0.03 λ.

V. EXPERIMENT

Figure 9 shows the photograph of the fabricated TLTA with folded rim at h = 0.03λ. Figure 10 shows the simulated and measured VSWR characteristics of the TLTA with folded rim at h = 0.05 λ, 0.04 λ, and 0.03 λ. Measured bandwidths are 42.75 %, 29.25 %, and 18.75 % at h = 0.05 λ, 0.04 λ, and 0.03 λ, respectively. The simulated and measured results agree well. Figures 11 and 12 show the simulated and measured radiation patterns of the TLTA with the folded rim on the vertical (*ZX*) and horizontal (*XY*) planes. Radiation pattern is similar to the monopolar radiation with small sized ground plane. The maximum measured gain at the center frequency are 4.25 dBi and 3.17 dBi at h = 0.05λ and 0.03λ, respectively. The omni-directional pattern is confirmed on the horizontal plane. The simulated and measured results agree well.

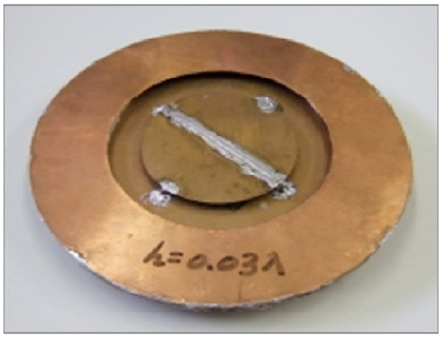

Fig. 9. Photograph of the fabricated top-loaded triangular antenna with folded rim at h = 0.03λ.

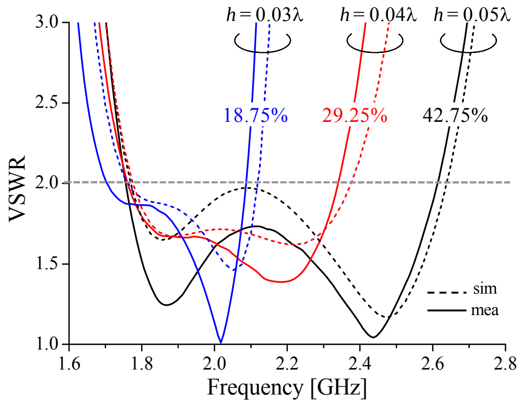

Fig. 10. Simulated and measured VSWR characteristics of the TLTA with folded rim at h = 0.05 λ, 0.04 λ, and 0.03 λ.

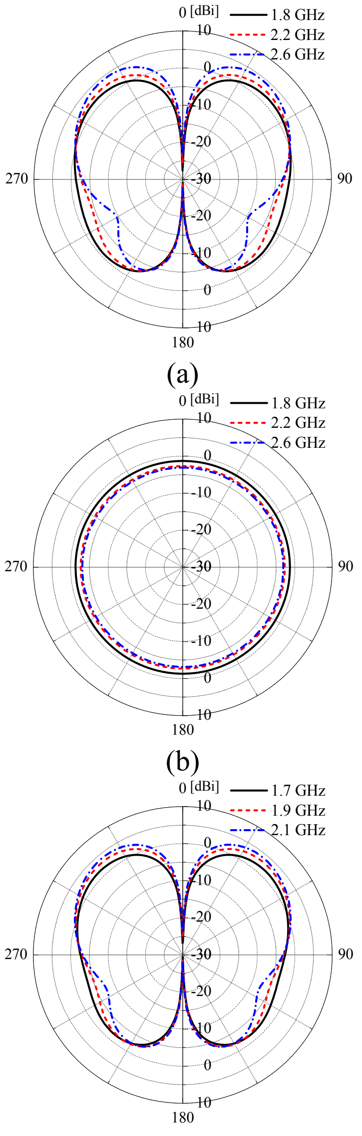

(a)

(b)

(c)

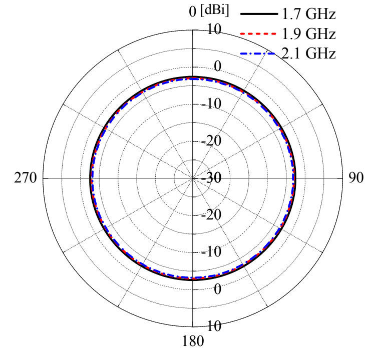

(d)

Fig. 11. Simulated radiation patterns of the top-loaded triangular antenna with folded rim on the (a) vertical and (b) horizontal planes at $h = 0.05\ \lambda$ and on the (c) vertical and (d) horizontal planes at $h = 0.03\ \lambda$.

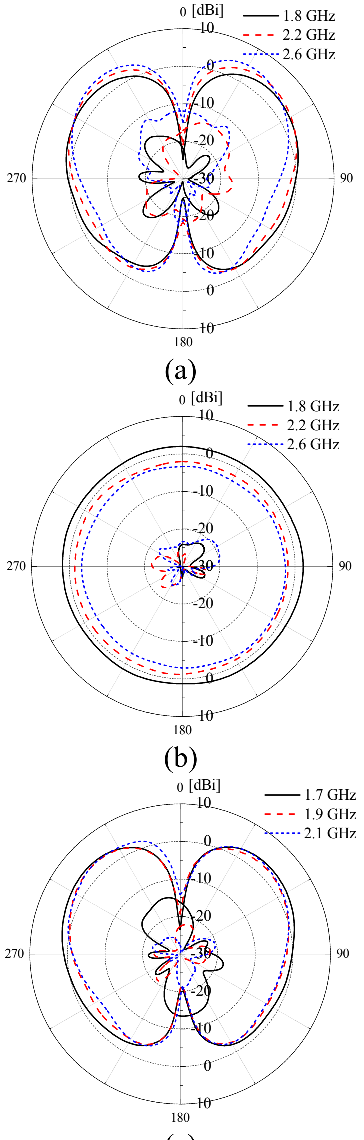

(a)

(b)

(c)

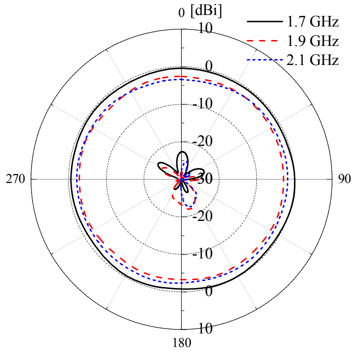

(d)

Fig. 12. Measured radiation patterns of the top-loaded triangular antenna with folded rim on the (a) vertical and (b) horizontal planes at $h = 0.05\ \lambda$ and on the (c) vertical and (d) horizontal planes at $h = 0.03\ \lambda$.

VI. CONCLUSION

This paper presents the impedance matching technique and the bandwidth characteristics of the low-profile TLTA with the folded rim. The impedance matching can be achieved by selecting the optimum parameters of the capacitance disk and the oblique shorting pins. When the folded rim is arranged, the maximum bandwidth of 43 %, 31 %, and 17 % can be achieved at $h = 0.05\ \lambda$, $0.04\ \lambda$, and $0.03\ \lambda$, respectively.

REFERENCES

[1] Y. Ebine, “Development of fiber-radio systems for cellular mobile communications,” *International Topical Meeting on Microwave Photonics*, Melbourne, Australia, vol. 1, pp. 249-252, Nov. 1999.

[2] T. Kanemoto and Y. Ebine, “A dual frequency disc loaded monopole antenna with matching short stubs,” *IEICE Technical Report*, AP2001-174, pp. 93-98, Jan. 2002.

[3] N. Goto and K. Kaneta, “Ring patch antenna for dual frequency use,” *IEEE AP-S International Symp.*, vol. 25, pp. 944-947, June 1987.

[4] M. Kamarudin, P. Hall, F. Colombel, and M. Himdi, “Integrated disc-loaded monopole array antenna and the small PIFA antennas,” *23rd Annual Review of Progress in Applied Computational Electromagnetics*, Verona, Italy, pp. 1801-1806, Mar. 2007.

[5] J. Zhao, C. Chen, and J. Volakis, “Ultra-wideband triple-ellipse inverted-hat antenna for aircraft communications,” *25th Annual Review of Progress in Applied Computational Electromagnetics*, Monterey, CA, pp. 82-87, Mar. 2009.

[6] S. Ong, A. Kishk, and A. Glisson, “Wideband and dual-band loaded monopole dielectric resonator antenna,” *19th Annual Review of Progress in Applied Computational Electromagnetics*, Monterey, CA, pp. 104-107, Mar. 2003.

[7] K. L. Lau, P. Li, and K. M. Luk, “A monopolar patch antenna with very wide impedance bandwidth,” *IEEE Trans. Antennas Propagat.*, vol. 53, no. 2, pp. 655-661, Feb. 2005.

[8] W. Kim, N. Michishita, and Y. Yamada, “Low-profile top-loaded monopole antenna with oblique shorting pins,” *39th European Microwave Conf.*, Rome, Italy, pp. 1476-1479, Sep. 2009.

[9] W. Kim, N. Michishita, and Y. Yamada, “Bandwidth characteristics of low-profile top-loaded monopole antenna with folded rim,” *International Symp. on Antennas and Propagation*, Bangkok, Thailand, pp. 365-368, Oct. 2009.

[10] W. L. Stutzman and G. A. Thiele, *Antenna Theory and Design* 2nd , pp. 66, John Wiley & Sons, Inc., 1998.

Naobumi Michishita received the B.E., M.E. and D.E. degrees in Electrical and Computer Engineering from Yokohama National University, Yokohama, Japan, in 1999, 2001, and 2004, respectively.

In 2004, he was a Research Associate at the Department of Electrical and Electronic Engineering, National Defense Academy, Kanagawa, Japan, where he is currently a Lecturer. From 2006 to 2007, he was a Visiting Scholar at the University of California, Los Angeles. His current research interests include metamaterial antenna and electromagnetic analysis.

Dr. Michishita is a member of the Institute of Electronics, Information and Communication Engineers (IEICE), Japan. He is also members of the Japan Society for Simulation Technology and the Institute of Electrical and Electronics Engineers (IEEE). He was the recipient of the Young Engineer Award presented by the IEEE Antennas and Propagation Society Japan Chapter and the IEICE, Japan (2004 and 2005).

Woo-Jin Kim received the B.Sc. degrees in Mathematics from Korea Military Academy, Seoul, in 2004. He received M.E. degrees in Electrical and Electronic Engineering from National Defense Academy, Kanagawa, Japan in 2011. He enlisted in Republic of Korea, Army in 2004. He was engaged in security for military defense. Now he is a captain of ROK army.

Yoshihide Yamada received the B.E. and M.E. degrees in Electronics from Nagoya Institute of Technology, Nagoya, Japan in 1971 and 1973, respectively. And he received the D.E. degree in Electrical Engineering from Tokyo Institute of Technology, Tokyo, Japan in 1989. In 1973, he joined the Electrical Communication Laboratories of Nippon Telegraph and Telephone Corporation (NTT). Till 1984, he was engaged in research and development of reflector antennas for terrestrial and satellite communications. From 1985, he engaged in R&D of base station antennas for mobile radio systems. In 1993, he moved to NTT Mobile Communications Network Inc. (NTT DoCoMo). In 1995, he was temporarily transferred to YRP Mobile Telecommunications Key Technology Research Laboratories Co., Ltd. At the same time, he was a guest professor of the cooperative research center of Niigata University, and a lecturer of Science University of Tokyo, both from 1996. In 1998, he changed his occupation to a professor of National Defense Academy, Kanagawa, Japan. Now, he is interested in very small antennas, aperture antennas and electromagnetic simulations of RCS. Also he is interested in measurement methods of SAR.

Prof. Yamada is a member of the Institute of Electronics, Information and Communication Engineers (IEICE) and became the Fellow in 2007. He is also members of JSST of Japan and IEEE society members of AP, VT and COMM.

UWB Square Monopole Antenna with Omni-Directional Radiation Patterns for Use in Circular Cylindrical Microwave Imaging Systems

N. Ojaroudi [1], M. Ojaroudi [2], N. Ghadimi [2], and M. Mehranpour [2]

[1] Department of Electrical Engineering
Ardabil Branch, Islamic Azad University, Ardabil, Iran
n_ojaroudi@srttu.edu

[2] Young Researchers Club
Ardabil Branch, Islamic Azad University, Ardabil, Iran
m.ojaroudi@iauardabil.ac.ir, noradin.ghadimi@gmail.com, and mehranpour.mehdi@gmial.com

Abstract **─** In this paper, a novel ultra-wideband printed monopole antenna (PMA) for the use in a circular cylindrical microwave imaging system is presented. The proposed antenna consists of a square radiating patch and a ground plane with a pair of L-shaped slots and two L-shaped conductor back plane, which provides a wide usable fractional bandwidth of more than 130 % (3.02 GHz - 15.21 GHz). By cutting two modified L-shaped slots with variable dimensions on the ground plane corners and also by inserting two L-shaped conductor back plane on the other side of the substrate, additional resonances are excited and hence much wider impedance bandwidth can be produced, especially at the higher band. The proposed antenna has an ordinary square radiating patch, therefore displays a good omni-directional radiation pattern even at higher frequencies, and also its radiation efficiency is greater than 82% across the entire radiating band. The designed antenna has a small size of 12 × 18 mm^2. Simulated and measured results are presented to validate the usefulness of the proposed antenna structure for circular cylindrical microwave imaging system.

Index Terms **-** Circular cylindrical microwave imaging systems, L-shaped conductor back plane, L-shaped slot, square monopole antenna, and UWB antenna.

I. INTRODUCTION

In general, the microwave imaging system is formed by a circular cylindrical array antenna in order to detect cancerous tissue. In this approach, circular cylindrical microwave imaging systems require small antennas with omni-directional radiation patterns and large bandwidth [1-5]. Thus, in circular cylindrical microwave imaging system, one of the key issues is the design of a compact antenna while providing wideband characteristic over the whole operating bands. It is a well-known fact that planar monopole antennas present really appealing physical features, such as simple structure, small size, and low cost. Due to all these interesting characteristics, planar monopoles are extremely attractive to be used in UWB applications, and growing research activity is being focused on them [6-11].

A simple method for designing a novel and compact microstrip-fed monopole antenna with multi resonances characteristic for microwave imaging system applications has been presented. In this paper, based on Defected Ground Structures (DGS), for bandwidth enhancement we use a pair of L-shaped slots in the ground plane. And based on the Electromagnetic Coupling Theory (ECT) [12], by using two L-shaped conductor back plane on the other side of the substrate, additional resonances are excited and hence much wider impedance bandwidth can be produced (unlike other monopole antennas

Submitted On: Apr. 28, 2012
Accepted On: Nov. 25, 2012

reported in the literature to date [6-11], this structure has an ordinary square radiating patch configuration). By obtaining these resonances, the usable upper frequency of the monopole is extended from 10.3 GHz to 15.21 GHz. The presented monopole antenna has a small size of $12\times18\ \text{mm}^2$. Good VSWR and radiation pattern characteristics are obtained in the frequency band of interest. Simulated and measured results are presented to validate the usefulness of the proposed antenna structure for circular cylindrical microwave imaging system applications.

II. ANTENNA DESIGN

The proposed monopole antenna fed by a microstrip line is shown in Fig. 1, which is printed on an FR4 substrate of thickness 1.6 mm. As shown in Fig. 1, the proposed antenna consists of a square radiating patch and a rectangular partially modified ground plane with two T-shaped parasitic structures. The basic antenna structure consists of a square patch, a feedline, and a ground plane. The square patch has a width W. The patch is connected to a feed line of width W_f and length L_f, as shown in Fig. 1. On the other side of the substrate, a conducting ground plane of width W_{sub} and length L_{gnd} is placed. The width W_f of the microstrip feedline is fixed at 2 mm. The proposed antenna is connected to a 50 Ω SMA connector for signal transmission.

Regarding Defected Ground Structures (DGS), the created slots in the ground plane provide an additional current path. Moreover, this structure changes the inductance and capacitance of the input impedance, which in turn leads to changing the bandwidth. The DGS applied to a microstrip line causes a resonant character. This generated resonant frequency can be controlled by changing the shape and size of the slot [9]. Therefore, by cutting two L-shaped slots in the ground plane and carefully adjusting its parameters, much enhanced impedance bandwidth may be achieved. Also L-shaped conductor back plane plays an important role in the broadband characteristics of this antenna because they can achieve additional resonances and improve the bandwidth [10]. In other words, the impedance bandwidth is effectively improved at the upper frequency that can be considered as a parasitic resonator electrically to the square monopole.

In this work, we start by choosing the dimensions of the designed antenna. These parameters, including the substrate, is $L_{sub} \times W_{sub}$ = 12 mm × 18 mm, or about $0.15\ \lambda \times 0.25\ \lambda$ at 4.2 GHz (the first resonance frequency). We have a lot of flexibility in choosing the width of the radiating patch. This parameter mostly affects the antenna bandwidth.

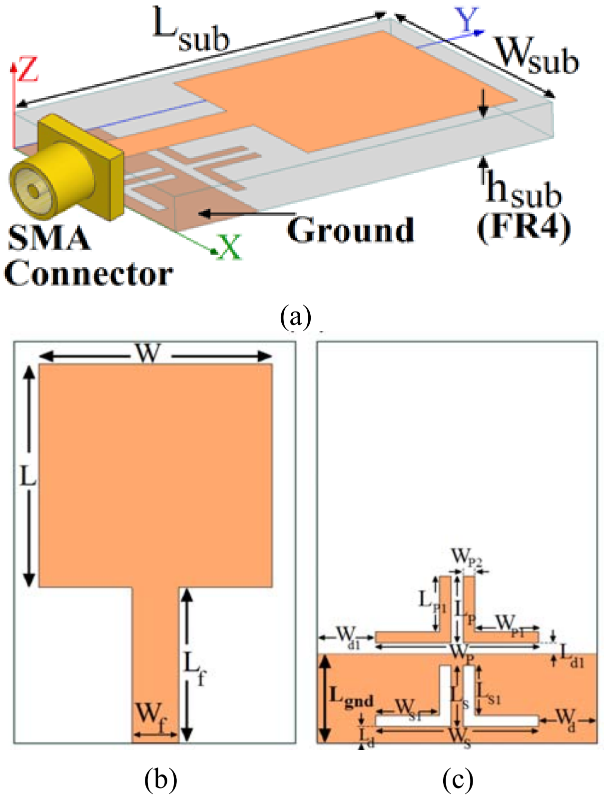

(a)
(b) (c)

Fig. 1. Geometry of the proposed microstrip-fed monopole antenna, (a) side view, (b) top view, and (c) bottom view.

As W decreases, so does the antenna bandwidth, and vice versa. Next step, we have to determine the length of the radiating patch L. This parameter is approximately λ_{lower} / 4, where λ_{lower} is the lower bandwidth frequency wavelength. λ_{lower} depends on a number of parameters such as the slot width as well as the thickness and dielectric constant of the substrate on which the antenna is fabricated [11]. The last and final step in the design is to choose the length of the resonator structure. In this design, the optimized length $L_{resonance}$ is set to resonate at $0.25\ \lambda_{resonance}$, where $L_{resonance3} = 0.5\ W_S + L_{S,}$ and $L_{resonance4} = W_{P1}$

+ L_{P1}. $\lambda_{resonance3}$ and $\lambda_{resonance4}$ correspond to new resonances frequencies at 11.7 GHz and 14.2 GHz, respectively. The final values of the presented slot antenna design parameters are specified in Table 1.

.

Table 1: The final dimensions of the designed antenna.

Param.	mm	Param.	mm	Param.	mm
W_{Sub}	12	L_{Sub}	18	W	10
L_f	7	W_f	2	W_{S1}	2.75
W_S	7	L_S	2.25	L_d	1.5
L_{S1}	1.75	W_d	2.5	W_P	5
W_{d1}	3.5	L_{d1}	0.5	L_{P1}	3
L_P	3.5	W_{P1}	1.75	W_{P2}	0.5
L	10	h	1.6	L_{gnd}	3.5

III. RESULTS AND DISCUSSIONS

The proposed microstrip monopole antenna with various design parameters were constructed, and the numerical and experimental results of the input impedance and radiation characteristics were presented and discussed. Ansoft HFSS simulations are used to optimize the design and to show the agreement between the simulation and the measurement results [13].

Figure 2 shows the structure of various antennas used for simulation studies. VSWR characteristics for ordinary square monopole antenna (Fig. 2(a)), with two L-shaped slots with (Fig. 2(b)), and the proposed antenna (Fig. 2(c)) are compared in Fig. 3. As shown in Fig. 3, in the proposed antenna configuration, the ordinary square monopole can provide the fundamental and next higher resonant radiation band at 4.8 GHz and 8.2 GHz, respectively, in the absence of the L-shaped slots and conductor back plane. The upper frequency bandwidth is significantly affected by using the L-shaped slots in the ground plane. This behavior is mainly due to the slots created in the ground plane, which provide an additional current path. Furthermore, by inserting two L-shaped conductor back plane on the ground plane the impedance bandwidth is effectively improved at the upper frequency [14-15]. It is observed that by using these modified elements, including two L-shaped slots and two L-shaped conductor back plane in the ground plane; an additional third (11.7 GHz) and fourth (14.2 GHz) resonances are excited respectively, and hence the bandwidth is increased**.** Moreover, the input impedance of the various monopole antenna structures that were shown in Fig. 2, is shown in Fig. 4 on a Smith Chart.

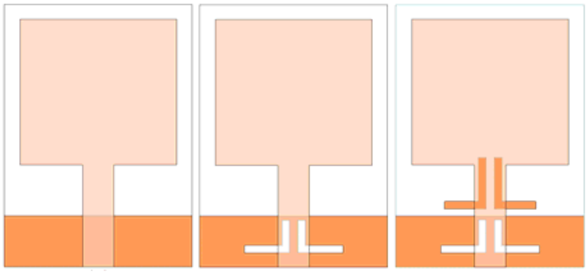
(a) (b) (c)

Fig. 2. **(**a) The basic structure (ordinary square monopole antenna), (b) antenna with two L-shaped slots in the ground plane, and (c) the proposed antenna.

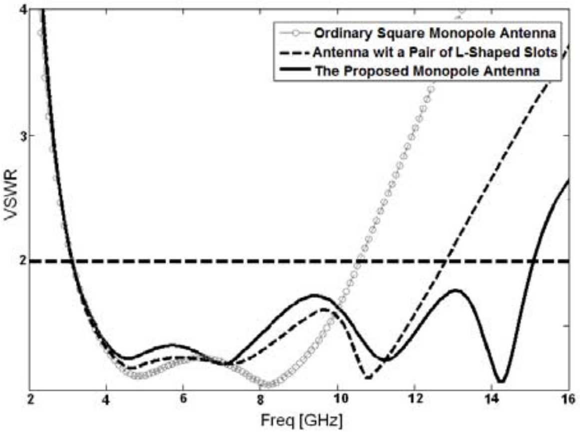

Fig. 3. Simulated VSWR characteristics for the various antenna structures shown in Fig. 2.

In order to know the phenomenon behind these additional resonances performance, the simulated current distributions on the ground plane patch for the ordinary square monopole antenna with two L-shaped slots on the ground plane at 11.7 GHz are presented in Fig. 5 (a). It can be observed in Fig. 5 (a), that the current is concentrated on the edges of the interior and exterior of the protruded L-shaped slots at 11.7 GHz. Other important design parameters of this structure are the L-shaped conductor back planes, used on the other side of the substrate. Figure 5 (b) presents the simulated current distributions on the ground plane at the forth resonance frequency (14.2 GHz). As shown in Fig. 5 (b), at the forth resonance frequency the current flows are more dominant around the L-shaped conductor back plane. The proposed antenna has a slightly higher efficiency rather than the ordinary square antenna throughout the entire radiating band, which is mainly owing to the new resonant properties. The HFSS results indicated that the proposed antenna features a good efficiency, being greater than 82 % across the entire radiating band.

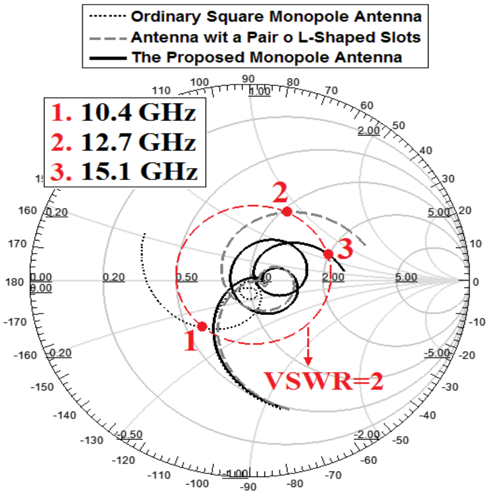

Fig. 4. Simulated input impedance on a Smith chart for the antenna structures shown in Fig. 2.

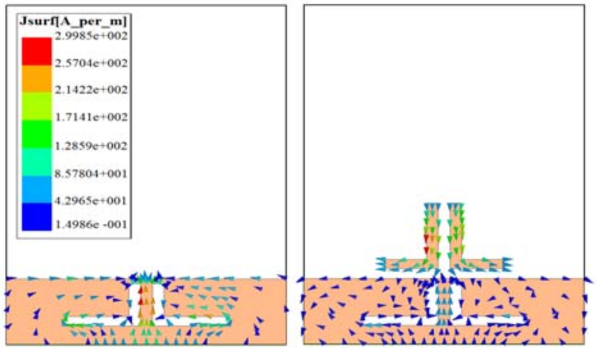

(a) (b)

Fig. 5. Simulated surface current distributions on the ground plane for, (a) the square monopole antenna with two L-shaped slots at the third resonance frequency (11.7 GHz), (b) the proposed antenna at the fourth resonance frequency (14.2 GHz).

The proposed antenna with optimal design, shown in Fig. 6, was built and tested. The measured and simulated VSWR and return loss characteristics of the proposed antenna are shown in Figs. 7 and 8, respectively. The fabricated antenna has the frequency band of 3.02 GHz to over 15.21 GHz. As shown in Fig. 7, there exists a discrepancy between the measured data and the simulated results. This could be due to the effect of the SMA port, in addition to the simulation accuracy due to the wide range of simulation frequencies. In a physical network analyzer measurement, the feeding mechanism of the proposed antenna is composed of an SMA connector and a microstrip line, whereas the simulated results are obtained using the HFSS. In HFSS by default, the antenna is excited by a wave port that it is renormalized to a 50 Ohm full port impedance, therefore this discrepancy between the measured data and the simulated results could be due to the effect of the SMA port [9]. In order to confirm the accurate VSWR characteristics of the designed antenna, it is recommended that the manufacturing and measurement process need to be performed carefully. In conclusion, as the monopole is a short radiator, the SMA connector can modify its impedance matching.

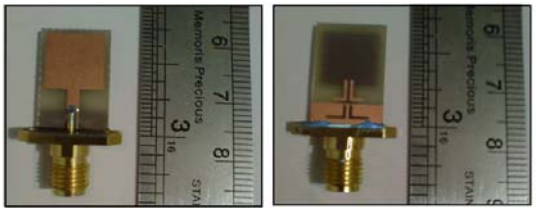

(a) (b)

Fig. 6. Photograph of the printed monopole antenna, (a) top view and (b) bottom view.

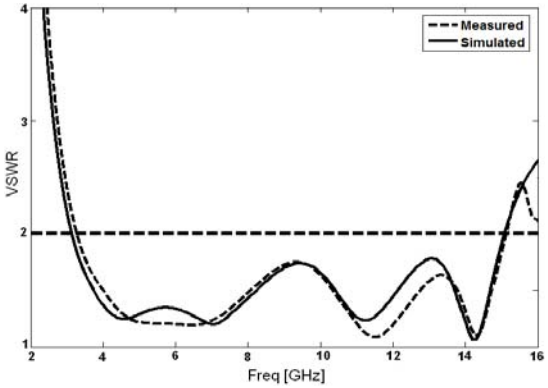

Fig. 7. Measured and simulated VSWR for the proposed antenna.

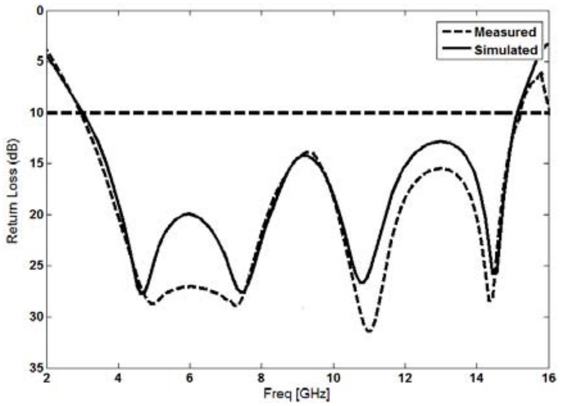

Fig. 8. Measured and simulated return loss for the proposed antenna.

Figures 9 and 10 show the measured radiation patterns at resonance frequencies, which includes the co-polarized and cross-polarized in the E-plane (Y-Z plane) and H-plane (X-Z plane). The main purpose of the radiation patterns is to demonstrate that the antenna actually radiates over a wide frequency band. It can be seen that the radiation patterns in X-Z plane are nearly omni-directional even at higher frequencies, and also the cross-polarization level is low at the four frequencies.

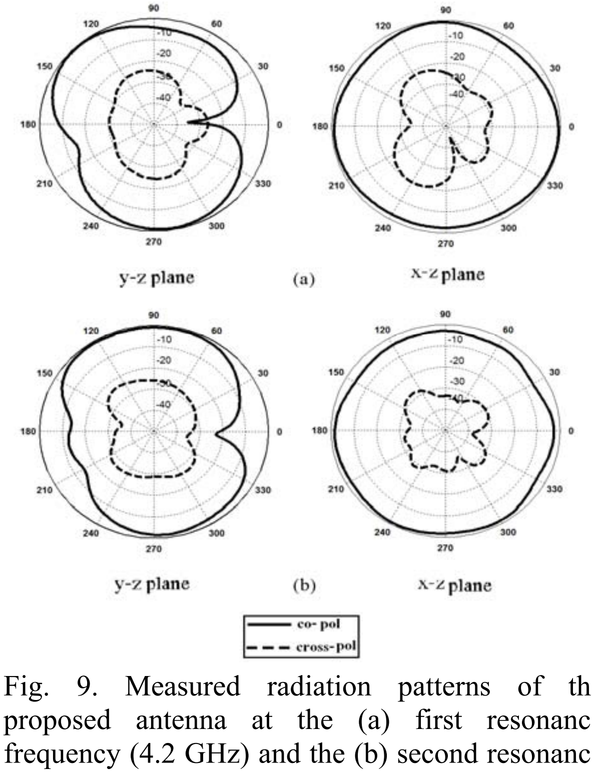

Fig. 9. Measured radiation patterns of the proposed antenna at the (a) first resonance frequency (4.2 GHz) and the (b) second resonance frequency (7.6 GHz).

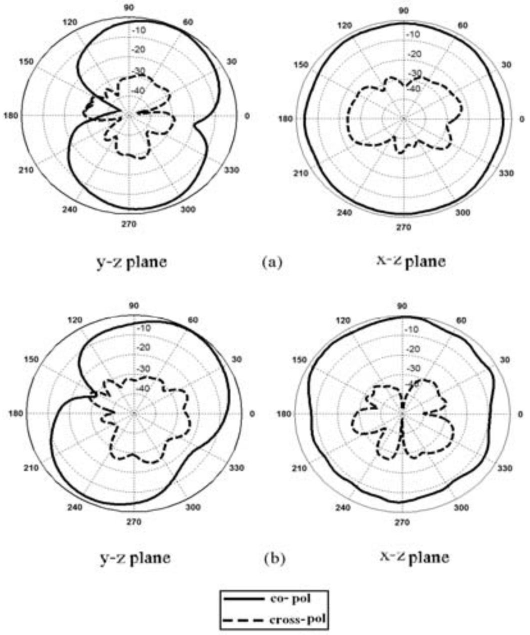

Fig. 10. Measured radiation patterns of the proposed antenna at the (a) third resonance frequency (11.7 GHz) and (b) fourth resonance frequency (14.2 GHz).

V. CONCLUSION

In this paper, a novel compact Printed Monopole Antenna (PMA) with multi-resonance characteristics has been proposed for the use in circular cylindrical microwave imaging system applications. The fabricated antenna satisfies the VSWR < 2 requirement from 3.02 GHz to 15.21 GHz. In order to enhance bandwidth we insert two L-shaped slots in the ground plane, and also by using two L-shaped conductor back plane with variable dimensions on the ground plane; additional resonances are excited and hence much wider impedance bandwidth can be produced, especially at the higher band. The designed antenna has a simple configuration with ordinary square radiating patch and small size of 12×18 mm^2. Simulated and experimental results show that the proposed antenna could be a good candidate for circular cylindrical microwave imaging system applications.

ACKNOWLEDGMENT

The authors are thankful to Microwave Technology (MWT) Company staff for their beneficial and professional help (www.microwave-technology.com).

REFERENCES

[1] E. C. Fear, S. C. Hagness, P. M. Meaney, M. Okonieweski, and M. A. Stuchluy, "Enhancing breast tumor detecting with near-field imaging," *IEEE Microwave Magazine*, pp. 48-56, March 2002.

[2] K. D. Paulsen and P. M. Meaney, "Non-active antenna compensation for fixed-array microwave imaging - Part I: model development," *IEEE Transaction on Medical Imaging*, vol. 18, pp. 496-507, June 1999.

[3] E. J. Bond, X. Li, S. C. Hagness, and B. D. Van Veen, "Microwave imaging via space-time beam forming for early detection of breast cancer," *IEEE Trans. Antennas Propag.*, vol. 51, no. 9, pp. 1690-1705, Aug. 2003.

[4] N. Ojaroudi, M. Ojaroudi, and N. Ghadimi, "UWB omni-directional square monopole antenna for use in circular cylindrical microwave imaging systems," *IEEE Antennas Wireless Propag. Lett.*, vol. 11, pp. 1350-1353, 2012.

[5] K. Halili, M. Ojaroudi, and N. Ojaroudi "Ultra wideband monopole antenna for use in a circular cylindrical microwave imaging system," *Microwave Opt. Technol. Lett.*, vol. 54, pp. 2202-2205, 2012.

[6] M. Mighani, M. Akbari, and N. Felegari, "A novel SWB small rhombic microstrip antenna with parasitic rectangle into slot of the feed line," *Applied Computational Electromagnetics Society (ACES) Journal*, vol. 27, no. 1, pp. 74-79, Jan. 2012.

[7] M. Mighani, M. Akbari, and N. Felegari, "A CPW dual band notched UWB antenna," *Applied Computational Electromagnetics Society (ACES) Journal*, vol. 27, no. 4, pp. 352-359, April 2012.

[8] R. Azim, M. T. Islam, and N. Misran, "Design of a planar UWB antenna with new band enhancement technique," *Applied Computational Electromagnetics Society (ACES) Journal*, vol. 26, no. 10, pp. 856-862, Oct. 2011.

[9] M. N. Jahromi and N. K. Barchloui, "Analysis of the behavior of Sierpinski carpet monopole antenna," *Applied Computational Electromagnetics Society (ACES) Journal*, vol. 24, no. 1, pp. 32-36, Feb. 2009.

[10] M. Mehranpour, J. Nourinia, C. Ghobadi, and M. Ojaroudi, "Dual band-notched square monopole antenna for ultrawideband applications," *IEEE Antennas Wireless and Propag. Lett.*, vol. 11, pp. 172-175, 2012.

[11] N. Ojaroudi, M. Ojaroudi, and S. Amiri, "Enhanced bandwidth of small square monopole antenna by using inverted U-shaped slot and conductor-backed plane," *Applied Computational Electromagnetics Society (ACES) Journal*, vol. 27, no. 8, pp. 685-690, August 2012.

[12] J. C. Wynn and K. L. Zonge, "Electromagnetic coupling, its intrinsic value, its removal and cultural coupling problem," *Geophysic*s, vol. 40, pp. 831-850, 1975.

[13] Ansoft High Frequency Structure Simulation (HFSS), ver. 13, *Ansoft Corporation*, 2010.

[14] B. H. Siahkal-Mahalle, N. Ojaroudi, and M. Ojaroudi, "A new design of small square monopole antenna with enhanced bandwidth by using cross-shaped slot and conductor-backed plane," *Microwave Opt. Technol. Lett.*, vol. 54, pp. 2656-2659, 2012.

[15] H. D. Chen, H. M. Chen, and W. S. Chen, "Planar CPW-fed sleeve monopole antenna for Ultra-wideband operation," *IET Microwave, Antennas Propag.* vol. 152, no. 6, pp. 491-494, Dec. 2005.

Nasser Ojaroudi was born on 1986 in Germi, Iran. He received his B.Sc. degree in Electrical Engineering from Azad University, Ardabil Branch. From 2011, he has been working toward the M.Sc. degree in Telecommunication Engineering at Shahid Rajaee Teacher Training University. Since March 2008, he has been a Research Fellow in the Microwave Technology (MWT) Company, Tehran, Iran. His research interests include ultra-wideband (UWB) microstrip antennas and band-pass filters (BPF), reconfigurable structure, and electromagnetic wave propagation.

Mohammad Ojaroudi was born on 1984 in Germi, Iran. He received his B.Sc. degree in Electrical Engineering from Azad University, Ardabil Branch and M.Sc. degree in Telecommunication Engineering from Urmia University. From 2010, he is working toward the Ph.D. degree at Shahid Beheshti University. From 2007 until now, he is a Teaching Assistant with the Department of Electrical Engineering, Islamic Azad University, Ardabil Branch, Iran. Since March 2008, he has been a Research Fellow (Chief Executive Officer) in the Microwave Technology Company (MWT), Tehran, Iran. From 2012 he is a reviewer in IEEE Transactions on Antenna and Propagations group. His research interests include analysis and design of microstrip antennas, design and modeling of microwave structures, radar systems, and electromagnetic theory. He is author and coauthor of more than 100 journal and international conference papers.

Noradin Ghadimi was born in ardabil-Iran in 1985, and received the B.Sc. degree in Electrical Engineering from the Islamic Azad University, Ardabil Branch, Ardabil, Iran, in 2009 and the M.Sc. degree in Electrical Engineering from the Islamic Azad University Ahar Branch, Ahar, Iran in 2011.His research interests include Power System Protection, modeling and analysis of Distributed Generations, renewable energy and communications systems.

Mehdi Mehranpour was born on 1986 in Meshkin Shahr, Iran. He received his B.Sc. degree in Electrical Engineering from Tabriz and Lorestan Universities in 2009, and the M.Sc. degree from Urmia University, in 2012. Since 2011, he has been a Research Fellow in the Microwave Technology Company (MWT), Tehran, Iran. His research interests are numerical methods in electromagnetic, monopole antenna, reconfigurable antenna, microstrip antennas for radar systems, equivalent circuit model of microstrip antenna, adaptive filters, and ultra-wideband (UWB) and small antennas for wireless communications.

A Compact Ultra-Wideband Antenna with Improved Triple Band-Notched Characteristics

Di Jiang, Yuehang Xu, Ruimin Xu, and Weigan Lin

School of Electronic Engineering,
University of Electronic Science and Technology of China, Chengdu, China
merryjiangdi@163.com

***Abstract* —** In order to prevent interference problem due to existing nearby communication systems within the ultra-wideband (UWB) operating frequency, a compact CPW fed triple-band-notched antenna using modified co-directional complementary split ring resonators (CSRRs) is proposed and investigated. The proposed antenna is realized by etching three modified co-directional CSRRs with different centers in the radiating patch. The measurement result shows that the proposed antenna can guarantee a wide bandwidth from 2 GHz to 16 GHz (VSWR $<$ 2) with triple unwanted band-notches successfully. The proposed antenna occupies a compact area of 25 × 27.9 mm^2 only. The antenna demonstrates omni-directional radiation patterns across almost the whole operating bandwidth, which is useful for UWB (3.1 GHz - 10.6 GHz) applications.

***Index Terms* -** Complementary split ring resonators (CSRRs), triple notched bands, and ultra-wideband antenna.

I. INTRODUCTION

Since the Federal Communications Commission (FCC)’s allocation of the frequency band 3.1 GHz - 10.6 GHz for commercial use, ultra-wideband (UWB) antennas have attracted much attention in recent years. Since the UWB approval, the technology has become one of the most promising technologies for future high data-rate wireless communication, high-accuracy radars, and imaging systems. It has the advantage of high-speed transmission, low power consumption, and simple hardware configuration compared with conventional wireless communication systems [1].

However, given the challenges encountered in the UWB antenna design, such as the system interferences, it necessitates the rejection of interference with some narrow bands for UWB applications in other communication systems, for example, the existing WLAN covering the 5.15 GHz - 5.35 GHz and 5.725 GHz - 5.825 GHz, and the C-band (3.7 GHz - 4.2 GHz) satellite communication systems [2]. To solve this problem, the existing techniques in extensive use can be classified into the following two categories: one method focuses on loading diverse parasitic elements on the antennas, such as strip near patch, stepped impedance resonators (SIRs) near the feed line, and ring-shaped patch near the ground. The other effective method is embedding various slots, such as arc-shaped slot, U-shaped slot, square-shaped slot, pi-shaped slot, H-shaped slot, and fractal slot [3]. However, these methods unavoidably exhibit some inherent defects in practical applications. Moreover, these methods usually occupy large area in designing antenna.

In this paper, we present a compact printed antenna with round slot, which has an UWB operating bandwidth with a tuneable triple-notched frequency at 3.9 GHz, 5.2 GHz and 5.9 GHz. Band-notched operations are achieved by embedding co-directional modified CSRR slots on the radiated patch. Both triple-band-notched characteristics and compact size can be achieved. The antenna has promising features, including good impedance matching performance over the whole operating frequency band, stable radiation patterns, and flexible frequency notched function.

II. ANTENNA DESIGN

The optimized co-directional CSRR antenna is depicted in Fig. 1. This antenna is printed on a 0.508 mm thick substrate RT5880 (dielectric constant ε_r = 2.2 and loss tangent tanδ = 0.0009) with dimension of

Submitted On: Oct. 11, 2012
Accepted On: Dec. 20, 2012

25 × 27.9 mm^2. The size of the inner-square (R_1, R_2, R_3) should be adjusted to determine the triple-band-notched frequency of the antenna. If other parameters are fixed, the triple-band notched frequency will increase with the decrease of R_1, R_2, and R_3. After that, the distance (C_1, C_2, and C_3) among these co-directional CSRRs should be also optimized. The radiation patch is excited using a 50 Ω CPW-feed [4-5]. The design of R_i and C_i (I = 1, 2, 3) can be easily fulfilled by commercial 3-D full-wave electromagnetic software HFSS [6]. The photography of the proposed prototype antenna is shown in Fig. 2. In order to investigate the causes of the band-notched, the surface current density of the antenna at different notched bands is presented [7]. The comparison of the surface current density between the convention structure and the proposed structure are shown in Figs. 3 and 4, respectively.

Figure 4 shows the surface current distributions at three center notched bands. The dimensions of the three co-directional complementary SRRs are corresponding to three notched bands. When the antenna is working at the center of lower notched band near 3.9 GHz, the outer complementary SRR behaves as a separator in Fig. 4 (a), which almost has no relation to the other band-notches [8]. Similarly, the middle complementary SRR operates as a second separator for the center of the middle notched band near 5.2 GHz in Fig. 4 (b). From Fig. 4 (c), the upper notched band near 5.9 GHz is ensured by the inner complementary SRR [9]. Additionally, as a certain current crowded on the ground plane near the CPW feed line would affect the antenna performance. Considering the simulation, one can find the dimensions of the ground plane, especially that has a significant effect on the triple band-notches performance, as well as the impedance bandwidth [10].

III. RESULTS AND DISCUSSION

The co-directional CSRRs can show distinct triple-band gaps due to the weaker mutual coupling between the inner and outer rings even when the triple band gaps are adjacent [11]. Thus, co-directional CSRRs is selected to obtain adjacent triple notched bands for C-band (3.7 GHz - 4.2 GHz) satellite communication systems and WLAN (5.15 GHz - 5.35 GHz and 5.725 GHz - 5.825 GHz) [12]. It is noted that the inner opening and outer opening are just co-directional [13]. Figure 5 shows the measured and simulated VSWRs versus frequency. The antenna could provide sufficiently wide impedance bandwidth covering 2 GHz - 16 GHz or more with the triple notched bands. Measured triple notched bands are 3.68 GHz - 4.25 GHz, 5.05 GHz - 5.60 GHz and 5.75 GHz - 6.22 GHz, respectively, covering C-band satellite communication systems and WLAN [14]. The measurements results show that the second notched band is a little offset compared with the simulation results, which is mainly due to the error induced by fabrication and assembly [15]. Therefore, by loading co-directional CSRRs with different centers, the co-directional CSRRs can provide good triple band-notch performance [16]. Owning to its triple band-notch structure, the co-directional complementary SRR can reduce the design space to achieve triple notched bands in comparison with the complementary edge-coupled SRR [17].

The radiation characteristics of the frequencies across the band have also been studied. Figure 6 shows the measured far-field radiation patterns of the *YZ* and *XY* plane at 3.5 GHz, 5 GHz, and 7.5 GHz. The three frequencies are chosen to be the frequency under lower notch band, the frequency between lower notch band and higher notch band, and the frequency beyond the higher notch band. Figure 6 shows the measured radiation patterns including the co- and cross-polarization in the H-plane (*XY* plane) and E-plane (*YZ* plane). The main purpose of the radiation patterns is to demonstrate that the antenna actually radiates over a wide frequency band. The pattern plots are expressed by Electric field co-polar and cross-polar components instead of the conventional method due to the measurement condition we have. However, this is also a good way to describe the radiation property of the antenna. The co-polar and cross-polar components may be smaller than ideal point source, which results in peaks lower than 0dB. Clearly, the *XY* plane patterns are close to omni-directional and the *YZ* plane patterns are monopole-like. All the obtained radiation patterns accord with those of the conventional printed UWB monopole antennas.

Figure 7 shows the measured radiation efficiency of the antenna. Due to the limitations of measurement facility, the radiation patterns above 12 GHz were not measured. The proposed antenna features efficiency between 50 % and 65% over the whole UWB frequency and lower than 10 % in the notch band. The features of the 55 % average radiation efficiency are good enough to satisfy an acceptable variation for practical power transmission [18].

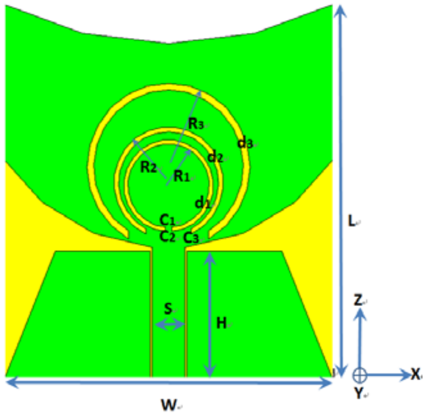

Fig. 1. Geometry of the antenna with dimensions $R_1 = 3.35$ mm, $R_2 = 4.09$ mm, $R_3 = 6.1$ mm, $d_1 = 0.3$ mm, $d_2 = 0.34$ mm, $d_3 = 0.5$ mm, $C_1 = 0.5$ mm, $C_2 = 3.35$ mm, $C_3 = 6$mm, $S = 2.5$ mm, $H = 9.8$ mm, $W = 25$ mm, and $L = 27.9$ mm.

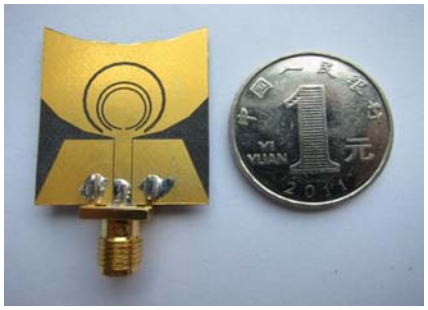

Fig. 2. Photograph of the proposed antenna.

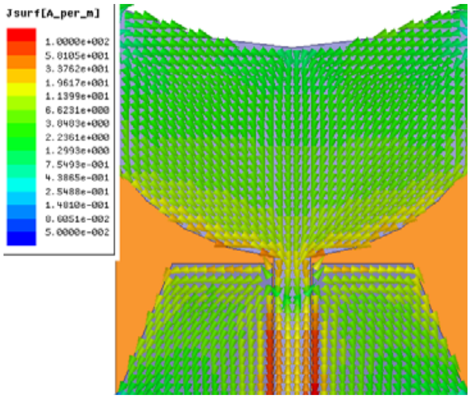

Fig. 3. Surface current distribution at 6 GHz without co-directional CSRR.

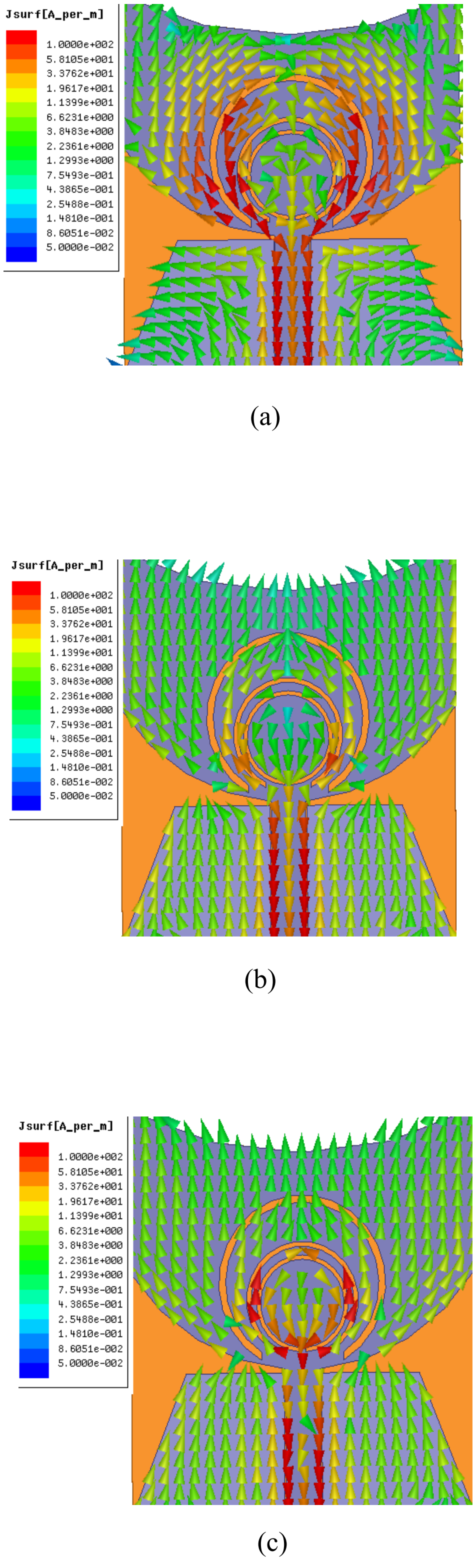

(a)

(b)

(c)

Fig. 4. Surface current distribution with co-directional CSRR at (a) 3.9 GHz, (b) 5.2 GHz, and (c) 5.9 GHz.

The gain patterns of the antenna are measured in an anechoic chamber. A fiber-optic link connected to the antenna under test has been used in order to measure the radiation pattern of our proposed compact antenna [19]. These techniques aim at limiting the alterations of the measurement coaxial cable on omni-directional radiation antennas. Figure 8 reveals its measured peak gain and simulated realized gain versus frequency. As can be seen from Fig. 8, the simulation and measured results fit each other well. It shows that the antenna gain ranges from 1.9 dBi to 7 dBi within the 2 GHz - 12 GHz frequency band. Of course, this is except that the proposed antenna gain decreases significantly to about -9.5 dBi, -7 dBi, and -5 dBi in the notched band. This confirms that the proposed antenna provides a high level of rejection to signal frequencies within the notched band [20]. Therefore, the results of the work are useful for short-range wireless communication systems.

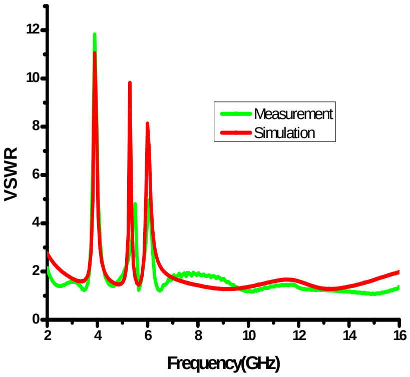

Fig. 5. Comparison of the simulated and measured VSWR of the proposed antenna.

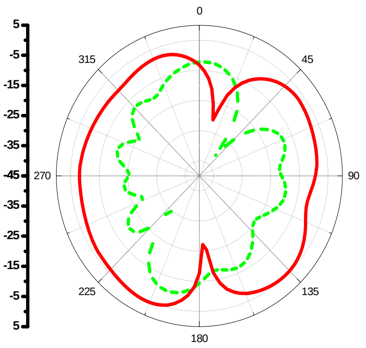

F = 3.5 GHz

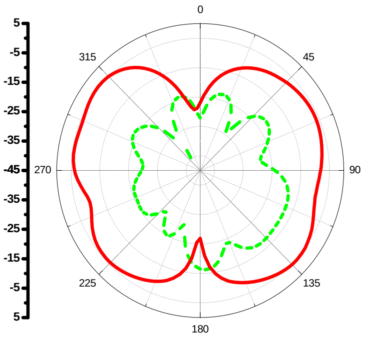

F = 5 GHz

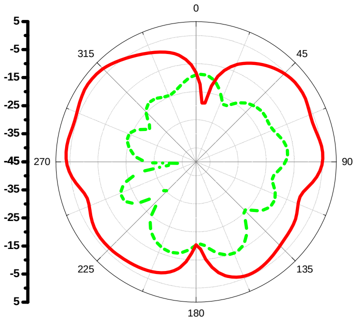

F = 7.5 GHz

(a)

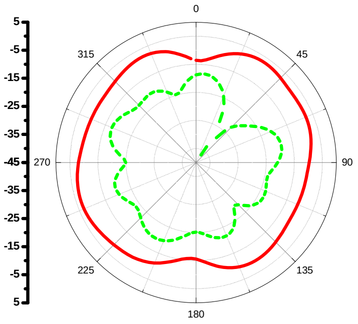

F = 3.5 GHz

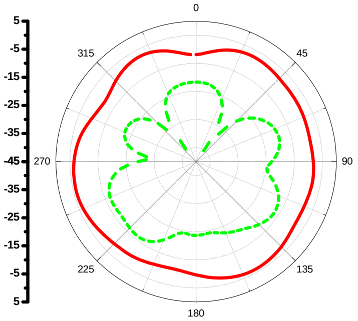

F = 5 GHz

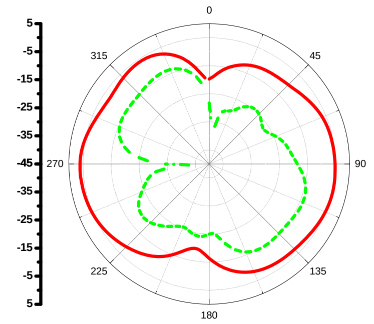

F = 7.5 GHz

(b)

Co-polar: ▬ **Cross-polar:** ▬ ▬

Fig. 6. Measured radiation patterns at the (a) *YZ* plane and (b) *XY* plane.

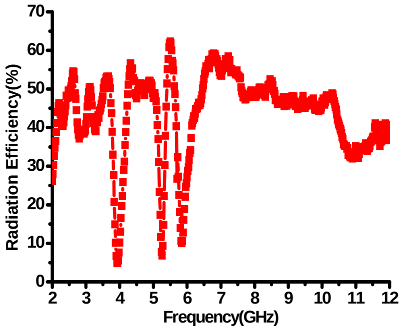

Fig. 7. Measured radiation efficiency of the proposed antenna.

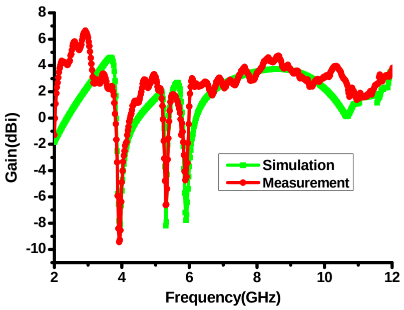

Fig. 8. Comparison of the simulated and measured gain of the proposed antenna.

IV. CONCLUSION

In this paper, a novel CPW-fed compact planar monopole UWB antenna with triple notched bands is proposed. By loading co-directional CSRRs with different centers, narrower and stronger band-notched properties as well as small design space size for the frequency band rejection function are achieved. Furthermore, broad bandwidth and good monopole-like radiation patterns are obtained with a rather compact antenna size. Also, the prototype has been constructed and measured to show a good agreement with the simulated results. Therefore, the results of the work are useful for short-range wireless communication systems.

ACKNOWLEDGMENT

This work is supported by the National Natural Science Foundation of China (Grant No.61106115, 60971037) and the Fundamental Research Funds for the Central Universities (ZYGX2011J018).

REFERENCES

[1] Z. N. Chen, N. Yang, Y. X. Guo, and M. Y.W. Chia, “An investigation into measurement of handset antennas,” *IEEE Trans. Instrum. Meas.*, vol. 54, pp. 1100-1110, June 2005.

[2] Y. Li, W. Li, and W. Yu, “A switchable UWB slot antenna using SIS-HSIR and SIS-SIR for multi-mode wireless communications applications,””*Appl. Comp. Electro. Society (ACES) Journal*, vol. 27, no. 4, pp. 340-351, April 2012.

[3] L. Liu, Y. Z. Yin, C. Jie, J. P. Xiong, and Z. Cui, “A compact printed antenna using slot-type CSRR for 5.2 GHz / 5.8 GHz band-notched UWB application,” *Microw. Opt. Technol. Lett.*, vol. 50, no. 12, pp. 3239-3242, Dec. 2008.

[4] X. L. Ma, W. Shao, and G. Q. He, “A novel dual narrow band-notched CPW-fed UWB slot antenna with parasitic strips,” *Appl. Comp. Electro. Society (ACES) Journal*, vol. 27, no. 7, pp. 581-586, July 2012.

[5] Z. L. Zhou, L. Li, and J. S. Hong, “A novel compact monopole antenna with triple high quality rejected bands for UWB applications,” *Appl. Comp. Electro. Society (ACES) Journal*, vol. 27, no. 8, pp. 654-659, August 2012.

[6] Ansoft High Frequency Structure Simulation (HFSS), ver. 10 Ansoft Corp, 2005.

[7] B. H. Siahkal-Mahalle, M. Ojaroudi, and N. Ojaroudi, “Enhanced bandwidth small square monopole antenna

with band-notched functions for UWB wireless communications," *Appl. Comp. Electro. Society (ACES) Journal*, vol. 27, no. 9, pp. 759-765, Sep. 2012.

[8] M. Ojaroudi, N. Ojaroudi, and Y. Ebazadeh, "Dual band-notch small square monopole antenna with enhanced bandwidth characteristics for UWB applications," *Appl. Comp. Electro. Society (ACES) Journal*, vol. 27, no. 5, pp. 420-426, May 2012.

[9] A. Valizade, C. Ghobadi, J. Nourinia, N. Ojaroudi, and M. Ojaroudi, "Band-notch slot antenna with enhanced bandwidth by using Ω-shaped strips protruded inside rectangular slots for UWB applications," *Appl. Comp. Electro. Society (ACES) Journal*, vol. 27, no. 10, pp. 816-822, Oct. 2012.

[10] F. Falcone, T. Lopetegi, M. A. G. Laso, J. D. Baena, J. Bonache, M. Beruete, R. Marqués, F. Martín, and M. Sorolla, "Babinet principle applied to the design of metasurfaces and metamaterials," *Phys. Rev. Lett.*, vol. 93, pp. 197401, 2004.

[11] M. Mighani, M. Akbari, and N. Felegari, "A CPW dual band notched UWB antenna," *Appl. Comp. Electro. Society (ACES) Journal*, vol. 27, no. 4, pp. 352-359, April 2012.

[12] J. Ding, Z. Lin, Z. Ying, and S. He, "A compact ultra-wideband slot antenna with multiple notch frequency bands," *Microw. Opt. Technol. Lett.*, vol. 49, no. 12, pp. 3056-3060, Dec. 2007.

[13] G. Zhang, J. S. Hong, B. Z. Wang, and G. Song, "Switched band-notched UWB/WLAN monopole antenna," *Appl. Comp. Electro. Society (ACES) Journal*, vol. 27, no. 3, pp. 256-260, March 2012.

[14] Y. D. Dong, W. Hong, Z. Q. Kuai, C. Yu, Y. Zhang, J. Y. Zhou, and J. Chen, "Development of ultrawideband antenna with multiple band-notched characteristics using half mode substrate integrated waveguide cavity technology," *IEEE Trans. Antennas Propag.*, vol. 57, no. 12, pp. 2894-2902, Dec. 2009.

[15] K. S. R yu and A. A. Kishk, "UWB antenna with single or dual band- notches for lower WLAN band and upper WLAN band," *IEEE Trans. Antennas Propag.*, vol. 57, no. 12, pp. 3942-3950, Dec. 2009.

[16] X. N. Low, Z. N. Chen, and T. S. P. See, "An UWB dipole antenna with enhanced impedance and gain performance," *IEEE Trans. Antennas Propag.*, vol. 54, no. 10, pp. 2959-2966, Oct. 2009.

[17] A. Nouri and G. R. Dadashzadeh, "A compact UWB band-notched printed monopole antenna with defected ground structure" *IEEE Antennas and Wireless Propag. Lett.*, vol. 10, pp. 1178-1181, 2011.

[18] C.-M. Wu, Y-L. Chen, and W.-C. Liu, "A compact ultrawideband slotted patch antenna for wireless USB dongle application" *IEEE Antennas and Wireless Propag. Lett.*, vol. 11, pp. 596-599, 2012.

[19] M. T. Partovi, N. Ojaroudi, and M. Ojaroudi, "Small slot antenna with enhanced bandwidth and band-notched performance for UWB applications," *Appl. Comp. Electro. Society (ACES) Journal*, vol. 27, no. 9, pp. 772-778, Sep. 2012.

[20] A. M. Montaser, K. R. Mahmoud, and H. A. Elmikati, "Integration of an optimized E-shaped patch antenna into laptop structure for bluetooth and notched-UWB standards using optimization Techniques," *Appl. Comp. Electro. Society (ACES) Journal*, vol. 27, no. 10, pp. 786-794, Oct. 2012.

Di jiang received the B.Sc. degree in Communication Engineering from the Gui Lin University of Electronic Technology (GLIET), China, in 2004, and is currently pursuing the Ph.D. degree in Electromagnetic Field and Microwave Technology at the University of Electronic Science and Technology of China(UESTC), Chengdu, China. His research interest includes miniature antenna, RF circuit, and metamaterial design and its application.

Yuehang Xu received the B. Sc. Degree, Master Degree, and Ph.D degree in 2004, 2007, and 2010, respectively in Electromagnetic Field and Microwave Technology from the University of Electronic Science and Technology of China (UESTC), respectively. He was a visiting scholar in Columbia University working on graphene RF devices during Sep. 2009 to Sep. 2010. He has been a lecture in UESTC since 2010. His research interests include wide band-gap semiconductor material and graphene based RF devices.

Ruimin Xu received the Ph.D. degree in Electrical Engineering from the University of Electronic Science and Technology of China (UESTC), Chengdu, China .At present as a university of electronic science and technology extremely high frequency complex system, deputy director of the national defense key discipline laboratory. The main research fields including microwave millimeter-wave circuits and systems, microwave monolithic integrated circuit.

Ganwei Lin. Chinese communist party members, Chinese academy of sciences, University of Electronic Science and Technology of China, professor, doctoral supervisor. China electronics association, member of IEEE microwave theory and technology to Beijing branch chairman.

Band-Notched Split-Ring Resonators Loaded Monopole Antenna for Ultrawideband Applications

Jing Zhang, Hongchun Yang, and Hongyan Liang

Department of Applied Physics
University of Electronic Science and Technology of China, Chengdu, 610054, China
doris0903@vip.qq.com, 2351563593@qq.com, and lianghongyan530@163.com

Abstract **─** A compact printed ultrawideband (UWB) monopole antenna with triple band-notched characteristics is presented. By adding a Split-Ring Resonator (SRR) on the radiating patch, the notched band in 3.3 GHz - 3.7 GHz for the WIMAX system is achieved. Furthermore, the proposed approach that utilizes the folded rectangular SRR structure is proven to be an effective way for band-notched designs. The antenna exhibit good band stop characteristics to reject the WLAN bands (5.15 GHz - 5.825 GHz bands) and downlink of X-band satellite communication systems (7.25 GHz - 7.75 GHz bands). The VSWR, gain, and radiation patterns of the proposed antenna are presented, which prove that the designed antenna is a good candidate for various UWB applications.

Index Terms - Band-notched, split-ring resonator, and UWB antenna.

I. INTRODUCTION

Because of the advantages such as compact size, light weight, low profile, and low cost [1], the planar monopole ultra-wideband (UWB) antennas are usually used for high-data-rate wireless communication [2], high-accuracy radar [3-4], and subsurface sensing applications [5]. However, electromagnetic interference (EMI) problems are quite serious for UWB systems since there are several other wireless narrowband standards that already occupy frequencies in the UWB band, such as worldwide interoperability for microwave access (WIMAX) operating in 3.3 GHz - 3.7 GHz, wireless local area network (WLAN) operating in 5.15 GHz - 5.825 GHz, and downlink of X-band satellite communication systems in 7.25 GHz - 7.75 GHz. An additional requirement for UWB antennas is to reject certain frequencies within the ultra-wide passband [6-9].

Recently, various band-notched designs have been developed and several UWB antennas with frequency band-notched function have been reported [10-16]. The most popular approach is cutting several slots on the patch or in its ground plane [17-21], the slots using U-shaped, and C-shaped or arc-shaped. In [22], an embedded slot with the length of about a quarter of the guided wavelength at the desired notch frequency tuning stub in a monopole is also proposed.

As for the structure of the broadband planar antenna introduced in this paper, the new antenna’s impedance bandwidth covers the bands of 3.1 GHz - 10.6 GHz, which is released by the Federal Communications Commission (FCC). An SRR is embedded in the patch to reject the WIMAX bands (3.3 GHz - 3.7 GHz bands). Two pair of SRRs nearby the feeding microstrip are designed to achieve the WLAN bands (5.15 GHz - 5.825 GHz bands) and the downlink of X-band satellite communication systems (7.25 GHz - 7.75 GHz bands). Measured results of the fabricated antenna prototype verify simulations with reasonably good agreements.

II. ANTENA DESIGN

The configuration of the proposed antenna is shown in Figs. 1 and 2. The final optimized dimensions are offered in Table 1. Basically, the antenna consists of a radiating monopole with an arc-shaped edge, a 50 Ω microstrip feeding mechanism, a simple rectangular ground plane on the back side of the substrate, an SRR embedded

Submitted On: Oct. 8, 2012
Accepted On: Dec. 25, 2012

in the radiating patch, and two folded rectangular SRRs nearby the feeding microstrip.

A. Baseline UWB Design

As shown in Fig. 3 (a), the UWB monopole antenna with 25 × 29 × 0.508 mm^3 dimensions is fabricated on the Rogers Duroid 5880 board material substrate. The substrate is of thickness 0.508 mm and relative permittivity $\varepsilon_r = 2.2$, loss tangent of $\tan\delta = 0.0009$. The monopole is fed by a 50 Ω microstrip line. On the back side of the substrate, the ground plane with length of 13 mm only covers the section of the microstrip feed line. The VSWR of the antenna is shown in Fig. 3 (b). It indicates that the working bandwidth of the antenna covers the entire UWB band (3.1 GHz - 10.6 GHz) under the condition of VSWR < 2.

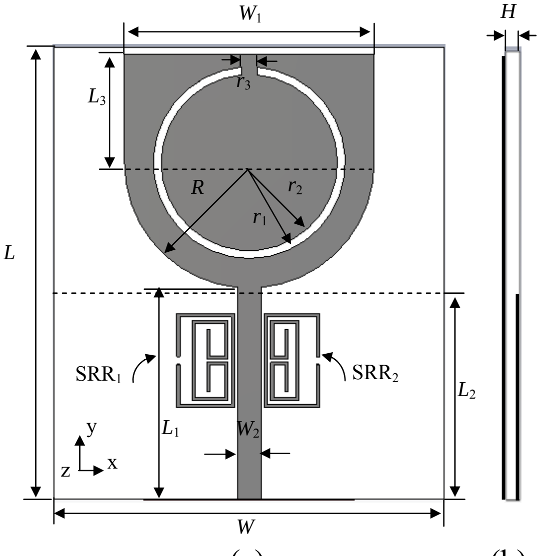

(a) (b)

Fig. 1. Geometry of the antenna (a) top view and (b) side view.

B. Single-Notch UWB Antenna Design

In order to reduce the EMI with the WIMAX band, the antenna with an SRR covering the interval 3.3 GHz - 3.6 GHz is desired. The proposed single-notched UWB antenna is illustrated in Fig. 4 (a). It is found that the parameters of $r_1 = 6.15$ mm and the size of its gap $r_3 = 0.5$ mm play critical roles in defining the band-notched frequency. Figure 5 shows that the band-notched frequency can be improved. It can be seen that a greater r_1 causes lower band-notched frequency. For instance, obviously the band-notched frequency increases from 3.36 GHz to 3.60 GHz as r_3 is varied from 0.2 mm to 0.8 mm.

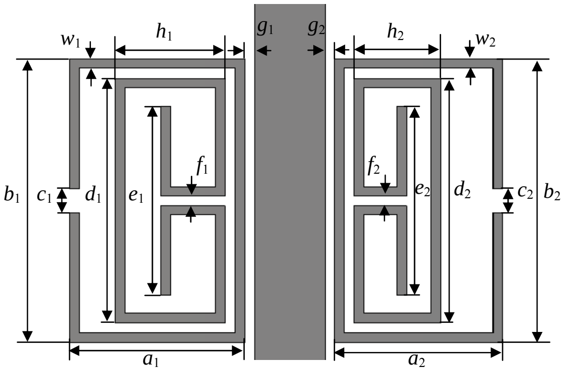

Fig. 2. Geometry of the SRR$_1$ (left side) and SRR$_2$ (right side).

Table 1: Optimal dimension of the design antenna.

Parameter	mm	Parameter	mm	Parameter	mm
L	29	r_2	5.6	w_1	0.2
L_1	13.6	r_3	0.5	a_2	3.55
L_2	13	a_1	3.7	b_2	6
L_3	7	b_1	6	c_2	0.5
W	25	c_1	0.5	d_2	5.17
W_1	16	d_1	5.1	e_2	4
W_2	1.5	e_1	4	f_2	0.2
H	0.508	f_1	0.2	g_2	0.2
R	8	g_1	0.2	h_2	1.82
r_1	6.15	h_1	2.3	w_2	0.2

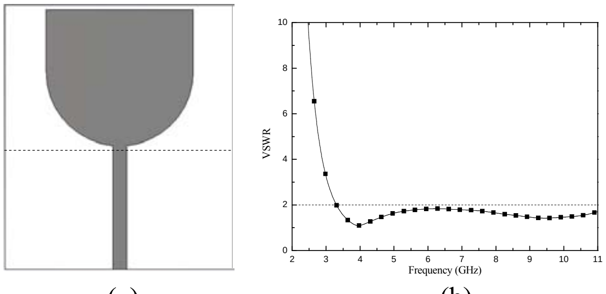

(a) (b)

Fig. 3. (a) Basic structure of monopole antenna and (b) the simulated VSWR.

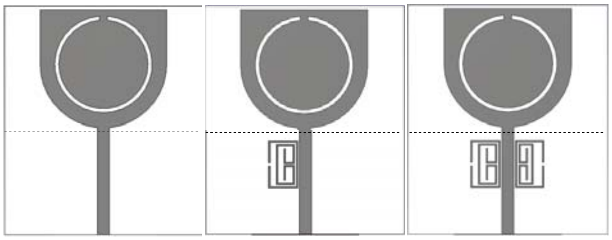

(a) (b) (c)

Fig. 4. (a) Basic structure with an open circuit slot, (b) basic structure with SRR_1, and (c) basic structure with both, SRR_1 and SRR_2.

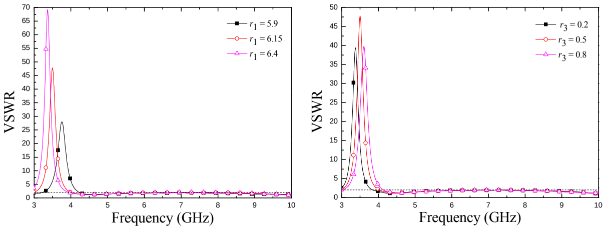

(a) (b)

Fig. 5. Simulation results with some important parameters: (a) Impact of parameter r_1 changes and (b) impact of parameter r_3 changes.

C. Tri-Band-notched UWB Antenna Design

As shown in Fig. 4 (b) and (c), SSR_1 and SSR_2 are designed nearby the feeding microstrip to achieve the notched-band of WLAN and the downlink of X-band satellite communication systems. The simulation results suggest that the notched bands of 5.15 GHz - 5.35 GHz and 7.15 GHz - 7.35 GHz are determined by SRR_1. Moreover, the notched bands of 5.65 GHz - 5.85 GHz and 7.55 GHz - 7.75 GHz are determined by SSR_2 synthetically. As an example, Figs. 6 and 7 show the optimization procedure of two of the notched-bands.

The notched-band of 5.15 GHz - 5.35 GHz is mainly decided by the dimensions of the inner part of SRR_1 shown in Fig. 4 (b), especially the parameter of h_1. Figure 6 (c) indicates that the notched-band drifts to higher frequency obviously as the h_1 is decreasing. However, as shown in Fig. 6 (a) and (b), the notched-band just drifts slightly while the parameters such as a_1 and c_1 of the external part of SRR_1 is changing. Figure 6 (d) shows that the notched-band also drifts slightly and the value of VSWR increases significantly as the parameter g_1 is changing. It can be explained by the coupling effects between the SRR and the feeding microstrip.

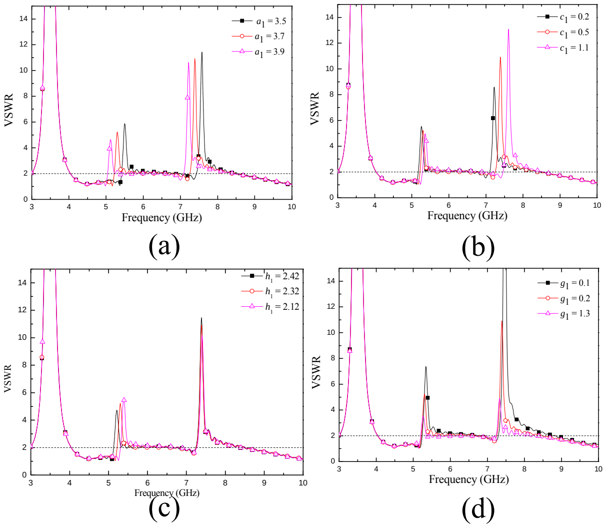

(a) (b)

(c) (d)

Fig. 6. Simulation results with some important parameters: (a) Impact of parameter a_1 changes, (b) impact of parameter c_1 changes, (c) impact of parameter h_1 changes, and (d) impact of parameter g_1 changes.

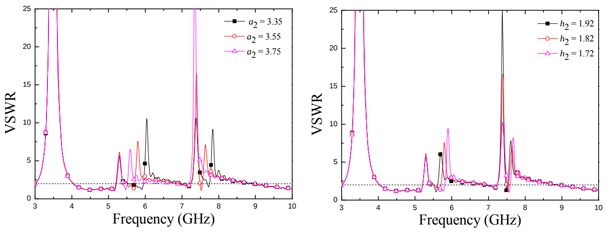

(a) (b)

Fig. 7. Simulation results with some important parameters. (a) Impact of parameter a_2 changes. (b) Impact of parameter h_2.

The notched-band of 7.15 GHz - 7.35 GHz is mainly decided by the dimensions of the external SRR_1 shown in Fig. 4 (b), especially the parameter of a_1 and c_1. Figure 6 (a) and (b) indicate that the notched-band drifts to lower frequency obviously as the a_1 is increasing and c_1 decreasing. Figure 6 (c) indicates that the parameter h_1 of the inner SRR just affects the notched-band slightly. Taking the optimization into account significantly, the notched-band of 5.15 GHz - 5.35 GHz and 7.15 GHz - 7.35 GHz can be achieved while the parameters of a_1, c_1, h_1 and g_1 are assigned as shown in Table 1. In a similar way, the parameters of a_2 and h_2 can also be optimized. As shown in Fig. 7, one can notice that the band-stop frequency of SSR_1 and SSR_2 did not affect each other, the notched-band of 5.15 GHz - 5.35 GHz and 7.15 GHz - 7.35GHz stay the same while the parameter a_2 and h_2 are optimized.

III. RESULT AND DISSCUSSION

Figure 8 shows the photograph of the proposed antenna. The simulated results are offered by the commercial software (CST MWS) based on the Finite Integration Technology (FIT). The measured curves are performed by an Agilent E5071C network analyzer. Figure 9 shows the simulated and measured VSWR of the proposed band-notched antenna. The working bandwidth covers the full frequency range from 2.8 GHz to 11.8 GHz except for the three notched-bands of 3.3 GHz - 3.7 GHz for the WIMAX system, 5.15 GHz - 5.825 GHz for the WLAN, and 7.25 GHz - 7.75 GHz for the downlink of the X-band satellite communication systems.

The simulated current distributions at 3.5 GHz, 5.25 GHz, 5.75 GHz, and 7.4 GHz of the proposed antenna are shown in Fig. 10. The simulated and measured radiation patterns of the E-plane (yz-plane) and H-plane (xz-plane) at 4 GHz, 6.5 GHz, and 9 GHz are plotted in Fig. 11, respectively. It indicates that the radiation patterns of the H-plane are nearly omni-directional over the working bandwidth except for the three notched-bands. The radiation pattern is similar to that formed by a typical monopole antenna. The simulated and measured gain at the operating bandwidth is shown in Fig. 12. The simulated results are in good agreement with the measured results within the experimental errors.

Fig. 8. Photograph of the fabricated antenna prototype.

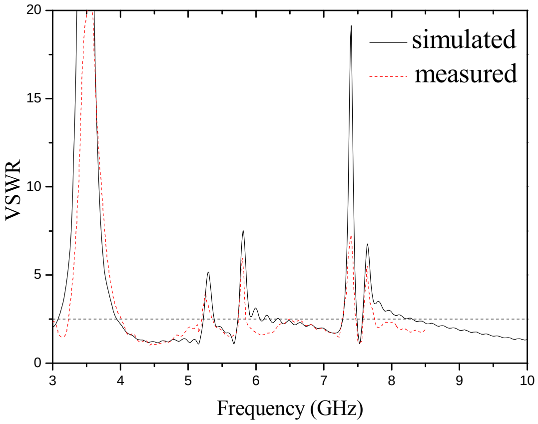

Fig. 9. Simulated and measured VSWR of the proposed antenna.

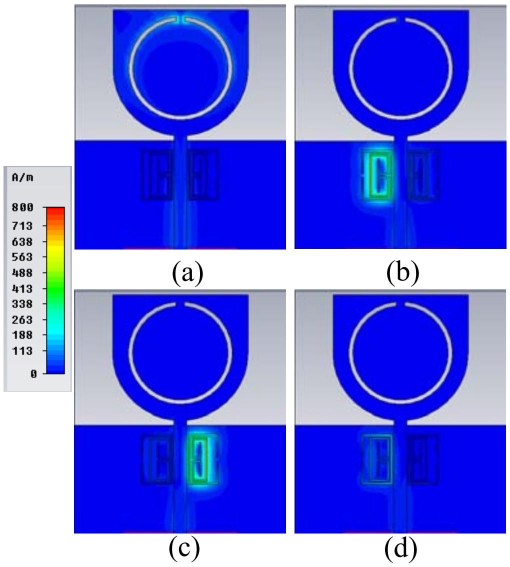

(a) (b)

(c) (d)

Fig. 10. Simulated surface current distributions on the radiating patch for the proposed antenna at (a) 3.5 GHz, (b) 5.25 GHz, (c) 5.75 GHz, and (d) 7.4 GHz.

IV. CONCLUSION

In this paper, a novel compact printed monopole antenna with three band-notched characteristics used for UWB applications has been presented and analyzed in detail. By successfully using SRRs elements and adjusting the parameters, the antenna has not only triple band-notched characteristics but also good omni-directional radiation patterns at the frequencies of interest. The antenna was fabricated and measured, showing good results and good agreement between simulations and measurements. It provides a simple and practical method in the notched-bands antenna designing.

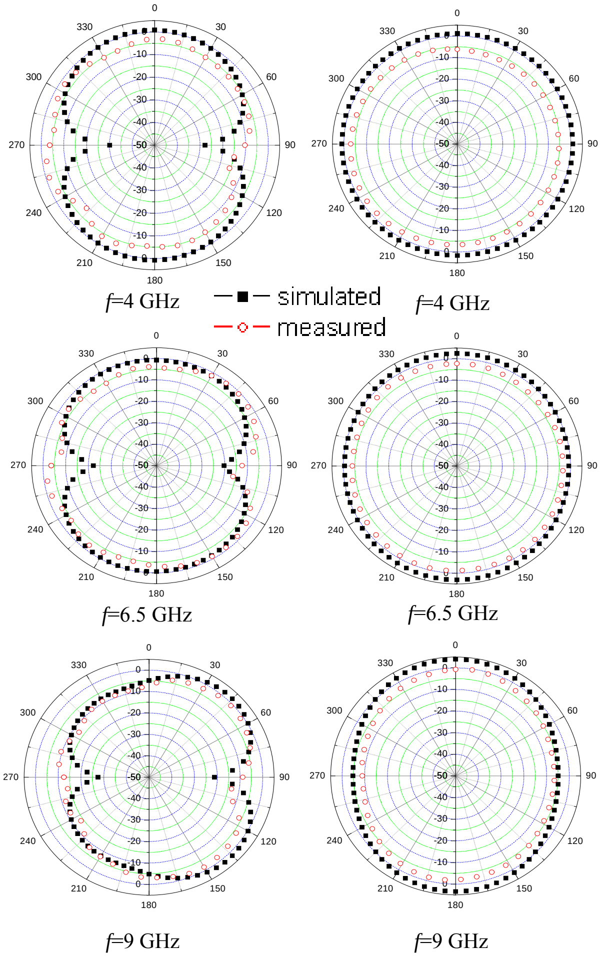

f=4 GHz *f*=4 GHz

f=6.5 GHz *f*=6.5 GHz

f=9 GHz *f*=9 GHz

Fig. 11. Simulated and measured radiation patterns in the E-plane (left side) and H-plane (right side) of the proposed antenna.

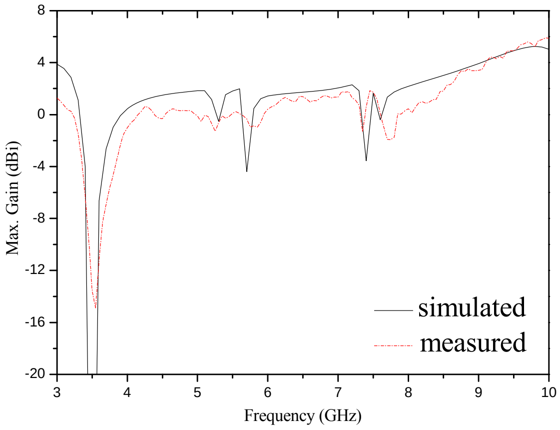

Fig. 12. Simulated and measured gain of the proposed antenna.

ACKNOWLEDGMENT

This work is supported by the International Cooperation Project (Grant 052011JYZ031).

REFERENCES

[1] Z. N. Chen, T. S. P. See, and X. M. Qing, "Small printed ultrawide-band antenna with reduced ground plane effect," *IEEE Trans. Antennas Propag.*, vol. 55, no. 2, pp. 383-388, Feb. 2007.

[2] M. J. Ammann and Z. N. Chen, "Wideband monopole antennas for multiband wireless systems," *IEEE Antennas Propag. Mag.*, vol. 45, no. 2, pp. 146-150, Apr. 2003.
W. S. Chen and K. Y. Ku, "Band-rejected design of the printed open slot antenna for WLAN/WiMAX operation," *IEEE Trans. Antennas Propag.*, vol. 56, no. 4, pp. 1163-1169, Apr. 2008.

[3] J. Zhang, H.-C. Yang, and D. Yang, "Design of a new high-gain circularly polarized antenna for Inmarsat communications," *IEEE Antennas Wireless Propag. Lett.*, vol. 11, pp. 350-353, 2012.

[4] S. W. Su and K. L. Wong, "Printed band-notched ultra-wideband quasi-dipole antenna," *Microwave Opt. Technol. Lett.*, vol. 48, no. 3, pp. 418-420, March 2006.

[5] Y. D. Dong, W. Hong, Z. Q. Kuai, and J. X. Chen, "Analysis of planar ultrawideband antennas with on-ground slot band-notched structures," *IEEE Trans. Antennas Propag.*, vol. 57, no. 7, pp. 1886-1893, July 2009.

[6] L. Peng and C.-L. Ruan, "UWB band-notched monopole antenna design using electromagnetic-bandgap structures," *IEEE Trans. on Microwave Theory and Technique*, vol. 59, no. 4, Apr. 2011.

[7] M. Ojaroudi, S. Yzdanifard, N. Ojaroudi, and R. A. Sadeghzadeh, "Band-notched small square-ring antenna with a pair of T-shaped strips protruded inside the square ring for UWB applications," *IEEE Antennas Wireless Propag. Lett* , vol. 10, pp. 227-230, 2011.

[8] O. Ayop, M. K. A. Rahim, M. R. Kamarudin, M. Z. A. Abdul Aziz, and M. Abu, "Dual band electromagnetic band gap structure incorporated with ultra-wideband antenna," *IEEE Antennas and Propagation Symposium*, April, 2010.

[9] Y. Li, W. Li, and W. Yu, "A switchable UWB slot antenna using SIS-HSIR and SIS-SIR for multi-mode wireless communications applications," *Applied Computational Electromagnetics Society (ACES) Journal*, vol. 27, no. 4, pp. 340-351, April 2012.

[10] D. S. Javan and O. H. Ghouchani, “Cross slot antenna with U-shaped tuning stub for ultra wideband applications,” *Applied Computational Electromagnetics Society (ACES) Journal*, vol. 24, no. 4, pp. 427-432, August 2009.

[11] W. C. Weng, “Optimal design of an ultra-wideband antenna with the irregular shape on radiator using particle swarm optimization,” *Applied Computational Electromagnetics Society (ACES) Journal*, vol. 27, no. 5, pp. 427-434, May 2012.

[12] R. Rouhi, C. Ghobadi, J. Nourinia, and M. Ojaroudi, “Ultra-wideband small square monopole antenna with band-notched function,” *Microwave Opt. Technol. Lett.*, vol. 52, no. 9, pp. 2065-2069, Sep. 2010.

[13] C.-C. Lin, P. Jin, and R. W. Ziolkowski, “Single, dual and tri-band-notched ultrawideband (UWB) antennas using capacitively loaded loop (CLL) resonators,” *IEEE Trans. Antennas Propag*., vol. 60, no. 1, Jan. 2012.

[14] M. Ojaroudi, N. Ojaroudi, and Y. Ebazadeh, “Dual band-notch small square monopole antenna with enhanced bandwidth characteristics for UWB applications,” *Applied Computational Electromagnetics Society (ACES) Journal*, vol. 27, no. 5, pp. 420-426, May 2012.

[15] A. T. Mobashsher, M. T. Islam, and N. Misran, “Wideband compact antenna with partially radiating coplanar ground plane,” *Applied Computational Electromagnetics Society (ACES) Journal*, vol. 26, no. 1, pp. 73-81, January 2011.

[16] M. Mehranpour, J. Nourinia, C. Ghobadi, and M. Ojaroudi, “Dual band-notched square monopole antenna for ultrawideband applications,” *IEEE Antennas and wireless propagation letters*, vol. 11, 2012.

[17] M. A. Antoniades and G. V. Eleftheriades, “A compact multiband monopole antenna with a defected ground plane,” *IEEE Antennas Wireless Propag. Lett*, vol. 7, 2008.

[18] J. William and R. Nakkeeran, “A new UWB slot antenna with rejection of WiMax and WLAN bands,” *Applied Computational Electromagnetics Society (ACES) Journal*, vol. 25, no. 9, pp. 787-793, Sep. 2010.

[19] M. Mighani, M. Akbari, and N. Felegari, “A CPW dual band-notched UWB antenna,” *Applied Computational Electromagnetics Society (ACES) Journal*, vol. 27, no. 4, pp. 352-359, April 2012.

[20] X. L. Ma, W. Shao, and G. Q. He, “A novel dual narrow band-notched CPW-fed UWB slot antenna with parasitic strips,” *Applied Computational Electromagnetics Society (ACES) Journal*, vol. 27, no. 7, pp. 581-586, July 2012.

[21] T. D. Nguyen, D. H. Lee, and H. C. Park, “Design and analysis of compact printed triple band-notched UWB antenna,” *IEEE Antennas Wireless Propag. Lett*., vol. 10, 2011.

Jing Zhang received the B.Sc. degree in Electronic Engineering from the University of Electronic Science and Technology of China (UESTC), Chengdu, China, in 2009, and is currently working toward the M.S. degree in radio physics at the Institute of Applied Physics, UESTC. Her research interests include electrically small antennas and borehole radar design and measurement.

Hong-chun Yang received his B.Sc. degree from Sichuan Normal University (1989), his M.S. (1997) degrees in Physics from Sichuan University (SCU), and Ph.D. degree in physics from the University of Electronic Science and Technology of China (UESTC) Chengdu, China. From 2003 to 2010, he was an Associate Professor with UESTC. Since 2010, he has been a Professor with the Institute of Applied Physics, UESTC. His research interests include millimeter-wave techniques, EM scattering, antenna theory, EM missiles, and UWB electromagnetics.

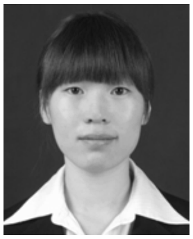

Hongyan Liang received the B.Sc. degree in Science and Technology of Electronic Information from the University of Electronic Science and Technology of China (UESTC), Chengdu, China, in 2010, and is currently working toward the M.S. degree in radio physics at the Institute of Applied Physics, UESTC. Her research interests include electrically small antennas and borehole radar design and measurement.

A Novel Bandpass Filters Using Complementary Split Ring Resonator Loaded Half Mode Substrate Integrated Waveguide

Di Jiang, Yuehang Xu, Ruimin Xu, and Weigan Lin

Fundamental Science on EHF Laboratory
University of Electronic Science and Technology of China, Chengdu, China
merryjiangdi@163.com, yhxu@uestc.edu.cn, rmxu@uestc.edu.cn, and wglin@uestc.edu.cn

***Abstract* —** A half mode substrate integrated waveguide with hexagon shaped complementary split-ring resonators (CSRRs) etched on the top of the waveguide is presented in this paper. The simulated results show that extra low insertion loss of about -0.1 dB and the return loss of -10 dB can be achieved. The proposed structure allows the implementation of a forward wave below the characteristic cutoff frequency of the waveguide. By changing the radius of the hexagon shaped CSRR, which is incorporated on top of the waveguide, the pass frequency band can be tuned easily. Finally, a compact band pass filter is fabricated and validated.

***Index Terms* -** Complementary split-ring resonator (CSRR) and half mode substrate integrated waveguide (HMSIW).

I. INTRODUCTION

The rectangular waveguide acting as an effective transmission line has already been widely used in the microwave and millimeter wave systems for many years. Recently, some new planar waveguide structures called substrate integrated waveguide (SIW) as well as laminated waveguide or post-wall waveguide were proposed and applied to develop many high-quality microwave and millimeter wave components [1]. Since SIW can be fabricated using the standard print circuit board (PCB) process, it is low-lost, mass-productive and easily integrated with planar circuits. In recent research, a split-ring resonator has been designed in a way to be embedded in thin substrates. It is shown that an SIW can be miniaturized when it is loaded by these embedded SRRs. However, sometime the sizes of the SIW blocks may be too large for practical circuits, and affect the integration [2]. To overcome such drawbacks, an improved guided wave structure, called "half model substrate integrated waveguide (HMSIW)" is proposed.

When SIW is used only with the dominant mode, the maximum E-field is at the vertical center plane along the propagation direction, so the center plane can be considered as an equivalent magnetic wall. If an SIW is divided into two parts along this plane, each can support a half of the field structure independently because of the large width-to-height ratio [3]. The substrate should be extended only a little bit in the horizontal direction to enclose any possible but negligible radiating energy or fringing field. The HMSIW can easily achieve low insertion loss, high power capacity in planar configuration, and also reduce the size in significant way [4]. This advantage is very important for highly integrated circuits and systems.

On the other hand, since the left-handed behaviors have been experimentally verified by Smith in 2001, there have been growing interests in the development and characterization of artificial structures with negative permittivity and permeability. Up to now, two types of structures have been proposed to realize such metamaterials, which have not been observed in nature. One is the periodic structure containing metallic strips and split ring resonators (SRR) [5], shown in Fig. 1 (a). The strips and resonators can be designed to exhibit negative ε and μ simultaneously in the same frequency band, and therefore the effective refraction index becomes less than zero. The CSRR is the negative image of the SRR, which can provide a negative effective permittivity in the

Submitted On: June 15, 2012
Accepted On: Nov. 25, 2012

vicinity of its resonant frequency, shown in Fig. 1 (b). Some special designs have also been proposed to replace the strip-resonator structure mentioned above, such as the Ω-shaped or S-shaped unit, which can broaden the left-handed bandwidth and lower the material loss obviously. These types have attracted a great deal of interest for the design of negative permeability and left-handed (LH) effective media. Another kind of structure is the planar LC network, composed of series capacitors and shunt inductors [6]. A number of applications have been realized in the microwave circuit design like filters, leaky wave antennas, and nonlinear phase shifters. The planar structures also include the left-handed transmission line (LHTL) implemented using microstrip lines, coplanar waveguides or finlines, which are loaded with different SRR structures [7].

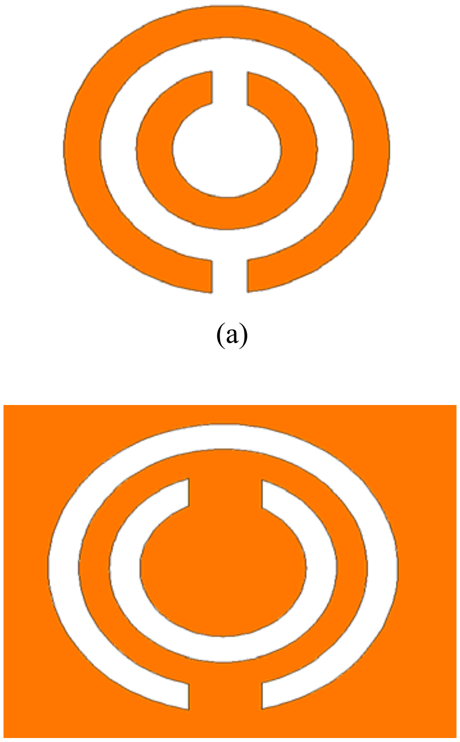
(a)

(b)

Fig. 1. The geometries of (a) SRR and (b) CSRR (orange region is metal, white region is substrate).

In this paper, the HMSIW is used for the design of the bandpass filter. This paper presents a new type of planar filter based on HMSIW technology for low microwave frequency band. An S-band filter is simulated by using HFSS software and fabricated with a single layer PCB process [8]. The filter operates at the center frequency of 3.05 GHz with the fractional bandwidth of around 7 %. Compared with SIW BPF, the HMSIW BPF with nearly half reduction in size has a wider stop band due to the HMSIW intrinsically cannot support the $TE_{2m,n}$ modes as well as TM modes [9]. The measured results, which show good agreement with the simulated results, are provided [10].

II. FILTER DESIGN

As we know, the electric field within HMSIW is orthogonal to the top and bottom surfaces of HMSIW, it is thus appropriate to etch the CSRR cells either on the top surface of HMSIW or bottom plane, which can guarantee that CSRR are properly excited. The behavior of the complementary structure excited by an axial electric field will be similar to that of the original SRR excited by an axial magnetic field. However, it is better to etch the CSRR cells on the top surface to preserve the integrity of the bottom plane, which is usually required in practical engineering [11]. The resultant HMSIW-CSRR bandpass filter is illustrated in Fig. 2, which is implemented in a substrate with thickness of 0.508 mm and dielectric constant 2.2. The orange part is a metallic conductor on HMSIW top plane and blue part is non-metallic [12]. The size of the inner-square (R_1, R_2) should be adjusted to determine the resonance frequency of CSRR resonators [13]. If other parameters are fixed, the resonance frequency will increase with the decrease of R_1 and R_2. If R_1 and R_2 are fixed, the resonance frequency could be also enhanced by increasing the slit width of squares (g). For the convenience of optimization work, the width of squares (d_1, d_2) and distance between squares are set to be the same as (g). This resonance structure will bring a sharp stop band. After that, the distance (C_1, C_2) between these two CSRRs should be also optimized. These optimization works were managed by using the commercial 3-D electromagnetic software HFSS. The proposed filter consists of a transmission line of HMSIW, a CSRR on HMSIW, and a transition between microstrip and HMSIW as shown in Fig. 2. The two symmetrical hexagon shaped slots are etched on the circuit board.

The topology of the proposed structure is shown in Fig. 3, which is divided into three parts. The proposed filter consists of a transmission line of HMSIW, a CSRR array on HMSIW, and a transition between microstrip and HMSIW [14]. The left and right parts are HMSIW-microstrip tapered transition including a segment of 50 Ω microstrip, a segment of tapered microstrip, and the discontinuity between microstrip and HMSIW. The tapered microstrip is used to excite the waveguide mode and match the impedance with HMSIW [15]. The middle part is an etched hexagon shaped CSRR cells on the top surface. The arrays of the metallized vias are designed to mimic the effect of the electric wall for the waveguide modes.

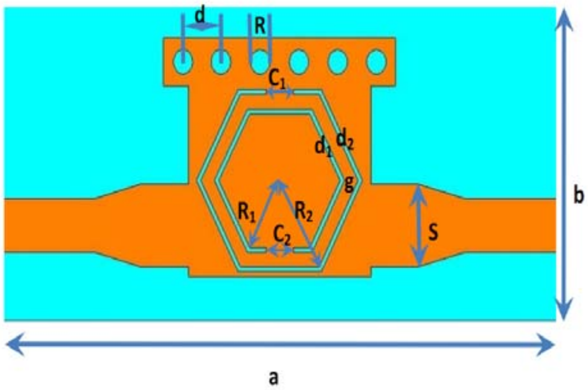

Fig. 2. Geometry of broadband bandpass filter, with dimensions $R_1 = 2.98$ mm, $R_2 = 3.27$ mm, $d_1 = 0.35$ mm, $d_2 = 0.15$ mm, $C_1 = 0.2$ mm, $C_2 = 0.2$ mm, $g = 0.13$ mm, $R = 0.5$ mm, $d = 0.7$ mm, $b = 6$ mm, $a = 20$ mm, and $S = 2.35$ mm.

As shown in Fig. 3, the impedance of each resonator for the wave propagating in transverse direction, can be calculated considering the loading at the center and using the well known transmission line formula,

$$Z_{in} = Z_0 \frac{Z_l + jZ_0 \tan(\beta_u l)}{Z_0 + Z_l \tan(\beta_u l)} \qquad (1)$$

where Z_o is the characteristic impedance and β_u is the phase constant (losses of the transmission line are assumed to be zero) of the transmission line, Z_L is the loading impedance, and l is the line length. The transmission line is approximated either by the microstrip line or other transmission line depending on the width-height ratio of the line and the dielectric material [16].

The propagation constant, γ for the infinite periodic structure is [17],

$$\cosh(\gamma a) = \cos(\beta_u a) + j\frac{Z}{2Z_0}\sin(\beta_u a). \qquad (2)$$

Z_o is the characteristic impedance and Z is the impedance of the CSRR resonance, and the phase constant γ in equation (2) are all the same as those of the resonators. With $\gamma = \alpha + \beta$, equation (2) can be rearranged as follows,

$$\cosh(\alpha a)\cos(\beta a) + j\sin(\alpha a)\sin(\beta a) = \cos(\beta_u a) + j\frac{Z}{2Z_0}\sin(\beta_u \alpha)\,. \qquad (3)$$

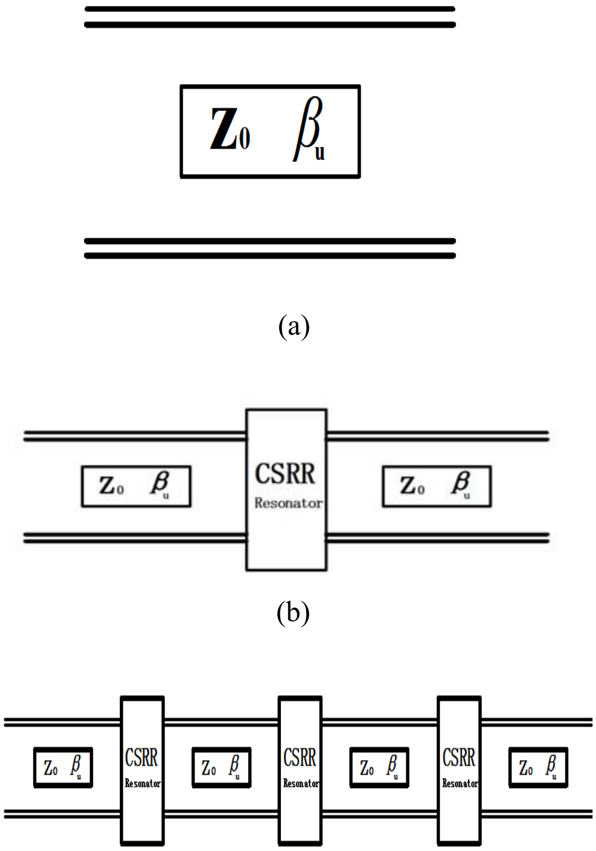

(a)

(b)

(c)

Fig. 3. Equivalent circuit of transmission line (a) loss-less ideal transmission Line, (b) equivalent circuit of a unit circuit representing HMSIW-CSRR resonator structure, and (c) equivalent circuit of periodic circuit representing HMSIW-CSRR structure.

Since the right hand side of equation (3) is real, as impedance is imaginary for loss-less resonators (as assumed), either $\beta = 0$, or $n\pi/a$, where “a” is the structure period. Condition $\alpha = 0$ corresponds to a non-attenuated, propagating wave on the periodic structure, and defines the pass-band of the structure. Equation (3) reduces to

$$\cos(\beta a) = \cos(\beta_u a) + j\frac{Z}{2Z_0}\sin(\beta_u \alpha) \quad , \qquad (4)$$

which can be solved for β if the magnitude of the right hand side is less than or equal to unity. Condition $\beta = 0$, $n\pi/a$ in equation (3) is given as

$$\cos(\alpha a) = \cos(\beta_u a) + j\frac{Z}{Z_0}\sin(\beta_u \alpha) \quad . \qquad (5)$$

As known, within the passband, the propagation constant is zero or $n\pi/a$, within the passband, the propagation constant β can be obtained from equation (5) at different frequencies. Based on the above concepts and the design principles of half mode substrate integrated waveguide, we can get the initial HMSIW-CSRR resonator parameters. A full-wave simulation is needed for the reason that the inductive and capacitive values for any periodic structure are not entirely independent because of the coupling effects.

III. SIMULATED AND MEASURED RESULTS

Figure 4 shows the simulated and measured results distributions at different frequencies. The simulated resonant frequency is 3.05 GHz. The simulations are in agreement with the measurements except 100 MHz frequency offset. The CSRR filter at 3.15 GHz has an insertion loss less than 3.5 dB and a return loss more than 10 dB for a 200 MHz bandwidth, and the minimum insertion loss is 3 dB. The discrepancy between the measured and simulated results is probably owing to the fabrication tolerance of the prototype and may be caused by the soldering effects of an SMA connector, which have been neglected in our simulations, even mainly due to lack precision of filter processing and assembly of the deviation caused due to the loss tangent of the substrate and the tolerance in manufacturing [18]. The width of microstrip transmission line is 1.5 mm. However, the manufacture microstrip transmission line usually has a certain tolerance. The used substrate in the simulation model is for ideal homogeneous materials (high purity, performance good consistency, and high surface finish). But in fact, there are certain tolerances in permittivity and thickness (details can be found in RT5880 datasheet), which are critical for designing center frequency. Also, there are tolerances in the fabrication of the microstrip by using the photolithography process, which can change the center frequency. Moreover, the RT5880 is of a 0.508 mm thickness and is of relatively soft and easy deformation. In order to fix the substrate with filter circuit on the measurement fixture, a process with epoxy is used. This process makes the substrate out of flatness while ideal model used in the simulation. However, these factors are difficult to be considered in the simulation.

It is important to note that the two resonance frequencies of the resonator, which are mainly determined by the CSRRs, can be arbitrarily controlled, making it possible to work on arbitrary pass band locations [19]. Figure 5 shows the different transmission responses by scaling the size of the CSRRs. The PCB layout of the filter is shown in Fig. 6, in which the thickness of the Rogers 5880 is 0.508 mm with dielectric substrate 2.2. It can be reduced by nearly half of the structure size compared with the standard SIWs structure operating at the same frequency. It can easily be integrated into any other planar circuits, and can achieve high performance once integrated as, the losses caused by the tapered transitions and SMA connectors would be removed [20].

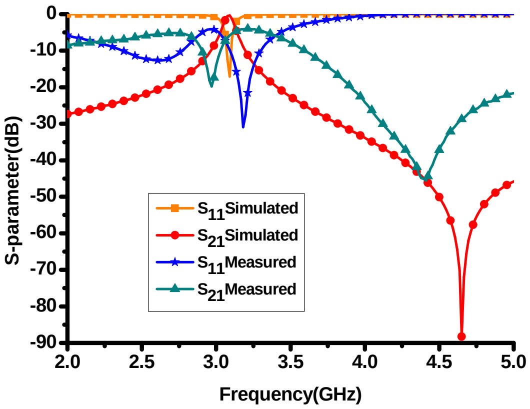

Fig. 4. Comparison of S-parameters between simulation and measured of CSRR-HMSIW BPF.

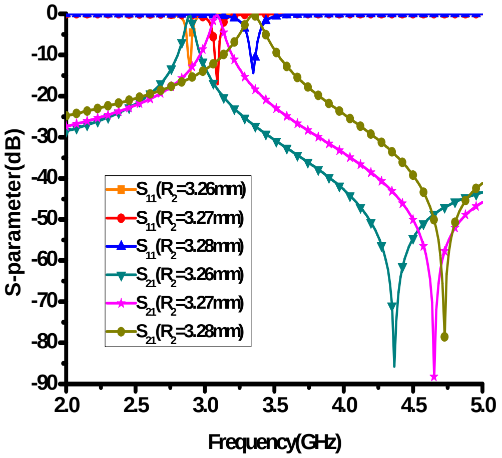

Fig. 5. S-parameters of different radius of CSRR.

(a)

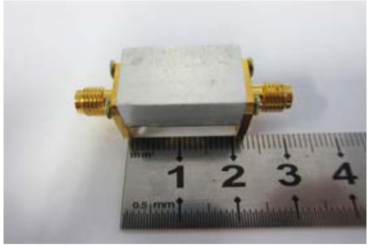

(b)

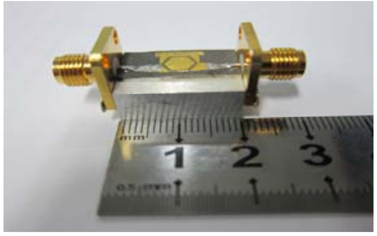

(c)

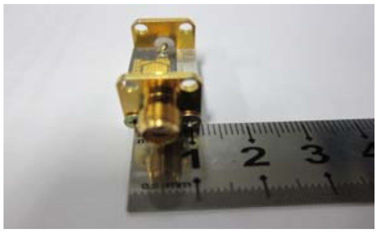

(d)

Fig. 6. The photograph of the fabricated filter; (a) top view, (b) bottom view, (c) front view and (d) side view.

IV.CONCLUSION

We have investigated the possibility of designing left-handed transmission line based on the half mode substrate integrated waveguide (HMSIW) technology. The hollow waveguide behave as a onedimensional plasma below the cut-off frequency of the dominant mode, and we have constructed a closed hexagon CSRR structure on the waveguide top produce magnetic response at the same frequency band. Therefore, the proposed structure has negative effective permittivity and effective permeability simultaneously and can guide electromagnetic waves in a left-handed way. The frequency responses have been simulated for HMSIW loaded with closed hexagon CSRR to determine the corresponding left-handed pass band. The pass band has a sharp rejection and relatively low insertion loss, which may find potential applications in microwave and millimeter wave integrated circuits like widening the bandwidth filters.

ACKNOWLEDGMENT

This work is supported by National Natural Science Foundation of China (Grant No. 61106115 and 60971037) and the Fundamental Research Funds for the Central Universities (ZYGX2011J018 and ZYGX2010X004).

REFERENCES

[1] R. Rezaiesarlak, M. Salehi, and E. Mehrshahi, “Hybrid of moment method and mode matching technique for full-wave analysis of SIW circuits,” *Appl. Comp. Electro. Society (ACES) Journal*, vol. 26, no. 8, pp. 688-695, August 2011.

[2] Z. C. Hao, W. Hong, J. X. Chen, X. P. Chen, and K. Wu, “Compact super-wide bandpass substrate integrated waveguide (SIW) filters,” *IEEE Trans.*

Microw. Theory Tech., vol. 53, no. 9, pp. 2968-2977, Sep. 2005.

[3] W. Shao and J. L. Li, "Design of a half-mode SIW high-pass filter," *Appl. Comp. Electro. Society (ACES) Journal*, vol. 26, no. 5, pp. 447-451, May 2011.

[4] Z. Hao, W. Hong, H. Li, H. Zhang, and K. Wu, "A broadband substrate integrated waveguide (SIW) filter," *IEEE AP-S Int. Dig.*, vol. 1B, pp. 598-601, July 2005.

[5] W. Hong, Y. Wang, Q. H. Lai, and B. Liu, "Half mode substrate integrated waveguide: A new guided wave structure for microwave and millimeter wave application," *Proc. Joint 31st Int. Conf. Infr. Millim. Waves and 14th Int. Conf. Terahertz Electron.*, Shanghai, China, Sep. 18-22, 2006.

[6] D. Deslandes and K. Wu, "Accurate modeling, wave mechanism, and design consideration of a substrate integrated waveguide," *IEEE Trans. Microw. Theory Tech.*, vol. 54, no. 6, pp. 2516-2526, June 2006.

[7] Y. Q. Wang, W. Hong, Y. D. Dong, B. Liu, H. J. Tang, J. X. Chen, X. X. Yin, and K. Wu, "Half mode substrate integrated waveguide (HMSIW) bandpass filter," *IEEE Microw. Wireless Compon. Lett.*, vol. 17, no. 4, pp. 265-267, Apr. 2007.

[8] B. Liu, W. Hong, Y. Q. Wang, Q. H. Lai, and K. Wu, "Half mode substrate integrated waveguide (HMSIW) 3 dB coupler," *IEEE Microw. Wireless Compon. Lett.*, vol. 17, no. 1, pp. 22-24, Jan. 2007.

[9] V. G. Veselago, "Electrodynamics of substances with simultaneously negative values of sigma and mu," *Soviet Phys. Uspekhi-Ussr*, vol. 10, pp. 509, 1968.

[10] J. B. Pendry, A. J. Holden, W. J. Stewart, and I. Youngs, "Extremely low frequency plasmons in metallic structures," *Phys. Rev. Lett.*, vol. 76, pp. 4773-4776, 1996.

[11] J. B. Pendry, A. J. Holden, D. J. Robbins, and W. J. Stewart, "Magnetism from conductors and enhanced nonlinear phenomena," *IEEE Trans. Microw. Theory Tech.*, vol. 47, no. 11, pp. 2075-2084, Dec. 1999.

[12] M. Gil, J. Bonache, J. Selga, J. García, and F. Martín, "Broadband resonant-type metamaterial transmission lines," *IEEE Microw. Wireless Compon. Lett.*, vol. 17, no. 2, Feb. 2007

[13] M. Tang, S. Xiao, D. Wang, J. Xiong, K. Chen, and B. Wang, "Negative index of reflection in planar metamaterial composed of single split-ring resonators," *Appl. Comp. Electro. Society (ACES) Journal*, vol. 26, no. 3, pp. 250-258, March 2011.

[14] J. Wang, W. Hong, H.-J. Tang, Y. Zhang, Y.-D. Dong, and K. Wu, "UWB bandpass filter with multiple frequency notched bands," *IEEE MTT-S Int. Microwave Workshop Series on Art of Miniaturizing RF and Microwave Passive Components*, Chengdu, China, pp. 106-109, Dec. 2008.

[15] X.-C. Zhang, Z.-Y. Yu, and J. Xu, "Novel band-pass substrate integrated waveguide (SIW) filter based on complementary split ring resonators (CSRRs)," *Progr. Electromagn. Rese.*, vol. 72, pp. 39-46, 2007.

[16] L.-S. Wu, X.-L. Zhou, Q.-F. Wei, and W.-Y. Yin, "An extended doublet substrate integrated waveguide (SIW) bandpass filter with a complementary split ring resonator (CSRR)," *IEEE Microw. Wireless Compon. Lett.*, vol. 19, no. 12, pp. 777-779, Dec. 2009.

[17] A. Taflove, *Computational Electrodynamics: The Finite-Difference Time-Domain Method*, Artech House Publications, 1995.

[18] Y.-D. Dong, T. Yang, and T. Itoh, "Substrate integrated waveguide loaded by complementary split-ring resonators and its applications to miniaturized waveguide filters," *IEEE Trans. Microw. Theory Tech.*, vol. 57, no. 9, pp. 2211-2223, Sep. 2009.

[19] G. E. Al-Omair, S. F. Mahmoud, and A. S. AlZayed, "Lowpass and bandpass filter designs based on DGS with complementary split ring resonators," *Appl. Comp. Electro. Society (ACES) Journal*, vol. 26, no. 11, pp. 907-914, Nov. 2011.

[20] E. Mehrshahi and M. Salehi, "A simple technique for propagation characteristics of substrate integrated waveguide," *Appl. Comp. Electro. Society (ACES) Journal*, vol. 25, no. 8, pp. 690-695, August 2010.

Di jiang received the B.Sc. degree in Communication Engineering from the Gui Lin University of Electronic Technology (GLIET), China, in 2004, and is currently pursuing the Ph.D. degree in Electromagnetic Field and Microwave Technology at the University of Electronic Science and Technology of China (UESTC), Chengdu, China. His research interest includes miniature antenna, RF circuit, and metamaterial design and its application.

Yuehang Xu received the B.Sc. Degree, Master Degree, and Ph. D degree in 2004, 2007, and 2010, respectively in Electromagnetic Field and Microwave Technology from the University of Electronic Science and Technology of China (UESTC), respectively. He was a visiting scholar in Columbia University working on graphene RF devices during Sep. 2009 to Sep. 2010. He has been a associate professor in UESTC since 2011. His research interests include wide band-gap semiconductor material and graphene based RF devices.

Ruimin Xu received the Ph.D. degree in Electrical Engineering from the University of Electronic Science and Technology of China (UESTC), Chengdu, China. At present as a University of Electronic Science and Technology extremely high frequency complex system, deputy director of the national defense key discipline laboratory. The main research fields including microwave millimeter-wave circuits and systems, microwave monolithic integrated circuit.

Ganwei Lin. Chinese communist party members, Chinese academy of sciences, University of Electronic Science and Technology of China, professor, doctoral supervisor. China electronics association, member of IEEE microwave theory and technology to Beijing branch chairman.

Design of Broadband Single Layer Printed Reflectarray Using Giuseppe Peano Fractal Ring

Mohsen Maddahali and Keyvan Forooraghi

Faculty of Electrical and Computer Engineering
Tarbiat Modares University, Tehran, Iran
madahali@modares.ac.ir and keyvan_f@modares.ac.ir

Abstract **─** In this paper, a broadband single-layer microstrip reflectarray element composed of a Giuseppe Peano fractal ring and a square ring is presented and investigated. The proposed element has been validated by comparing the simulation results with those obtained by measurement in a waveguide simulator. By using this type of cell element, a wideband single layer reflectarray is designed, fabricated, and tested. Measured results demonstrate 1 dB gain bandwidth of 17 % over the frequency range of 12.25 GHz - 14.5 GHz.

Index Terms- Aperture efficiency, Giuseppe Peano fractal, microstrip antenna, reflectarray, and TE and TM waves.

I. INTRODUCTION

Microstrip reflectarray antenna has been proposed as a major alternative for parabolic reflector antenna since 1991[1]. The reflectarray idea combines certain characteristics of reflector and array antenna, respectively. The reflectarray consist of an array of patches that convert spherical waves produced by the feed into plane waves to form a main beam in a given direction. Reflectarray antennas have several advantages such as low manufacturing cost and simple mechanical design, but they suffer from narrow frequency bandwidth, which is due to differential spatial phase error in large reflectarray and narrow band operation of each array elements. To overcome these limitations, a lot of researches have been made in recent years [2-15]. In [5-7], a multilayer reflectarray composed of two or three stacked array with rectangular patches of variable size with 1 GHz bandwidth, and 400˚ phase variation has been introduced. Another example, in [8] a single-layer microstrip reflectarray element composed of a rectangular patch and a rectangular ring has been introduced. Using these elements, a prime-focus 45-element linear reflectarray operating at 10 GHz has been designed. In [9] a wideband reflectarray using artificial impedance surface with 1 dB gain bandwidth of 20 % has been proposed. The other worthwhile ideas are a broadband reflectarray design with a combination of cross and rectangular loop element [10] or a reflectarray design based on aperture coupled patches with a true time delay line [11].

In this paper, a wideband reflectarray element with a 600˚ phase variation range in 11.5 GHz - 14.5 GHz has been designed exploiting Giuseppe Peano fractal ring. Fractal structures can give rise to miniaturized wideband antenna. The proposed structure is described in section II along with the definition of parameters and demonstration of the simulation results. In order to validate the simulated results, the fractal ring element is fabricated and tested in a waveguide simulator. Measured results will be shown in section III. In section IV, using these elements, a one layer reflectarray is designed to operate at 13.5 GHz. The overall size of this antenna is 250 mm × 250 mm (11.25 λ_0 × 11.25 λ_0).

II. THE STRUCTURE AND PHASE CHARACTERISTIC OF THE PROPOSED ELEMENT

The recursive procedure of the Giuseppe Peano fractal is shown in Fig. 1, which is applied to the edge of the square patch up to the first iteration as depicted in Fig. 2 [12].

Submitted On: Oct. 2, 2012
Accepted On: Dec. 26, 2012

Fig. 1. Initiator and generator of the Giuseppe Peano fractal.

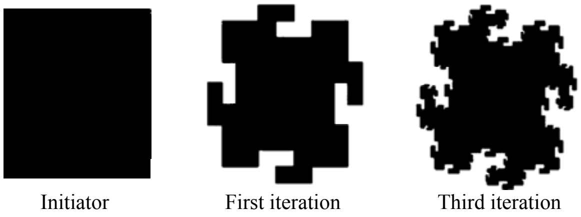

Initiator First iteration Third iteration

Fig. 2. Giuseppe Peano fractal as applied to the edges of the metallic patches.

Using this fractal, a fractal ring element has been designed and shown in Fig. 3. The proposed structure consists of one Giuseppe Peano fractal ring in combination of a square ring. In this layout, the fractal ring layer is etched on a 5 mil thick Rogers RT/Duroid 5880 with a dielectric constant of 2.2 and a loss tangent of 0.0009. A 3.125 mm thick layer of ECCOSTOCK PP-2 low-loss foam ($\varepsilon_r=1.03$) is stacked beneath the ring layer for bandwidth enhancement and wider phase range purposes. The configuration of the proposed fractal ring microstrip antenna is depicted in Fig. 3 with the following optimized parameters: $w_1 = w_2 = 0.2$ mm, $t_1 = 3.175$ mm, $t_2 = 0.127$ mm, $l_2 = l_1 - 1.5\, w_1$, $l_3 = 2/7\, l_1$, and l_1 change to produce proper phase. For the center frequency of 13.5 GHz, 12 mm (0.54 λ_0) period square unit cell is chosen in order to avoid the formation of grating lobes in the array's radiation pattern.

The scattering matrix of the structure has been obtained using high-frequency structure simulator software (HFSS) [13] and a unit-cell approach with the master-slave boundary to emulate an infinite periodic structure as shown in Fig. 4. The reflection phase and reflection amplitude of the fractal ring element on the top surface of the patch for different fractal side are shown in Figs. 5 and 6, respectively. As shown in both figures, a 600° phase variation range and a maximum of 0.8 dB loss can be achieved with the change in the fractal length from 3.5 mm to 9.1 mm. As the phase variation range increases, a higher efficiency can be attained. Furthermore, a parallel phase variation in the whole band has been achieved for this particular combination for the fractal and the square ring, using a cell size of 12 mm .

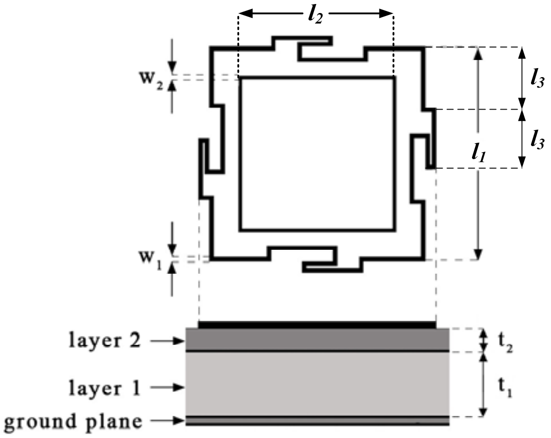

Fig. 3. Periodic unit cell of the proposed element.

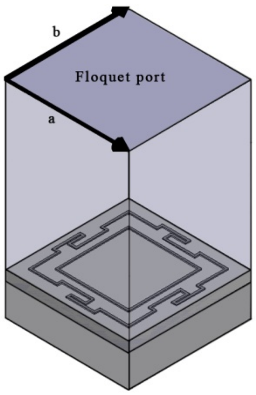

Fig. 4. Rectangular unit cell of HFSS simulation using floquet port.

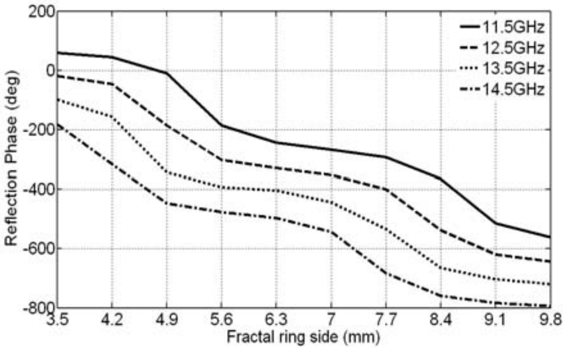

Fig. 5. The reflection phase at normal incidence for a periodic array of fractal ring on a grounded substrate versus the fractal ring side at four frequencies on the top surface of the patch.

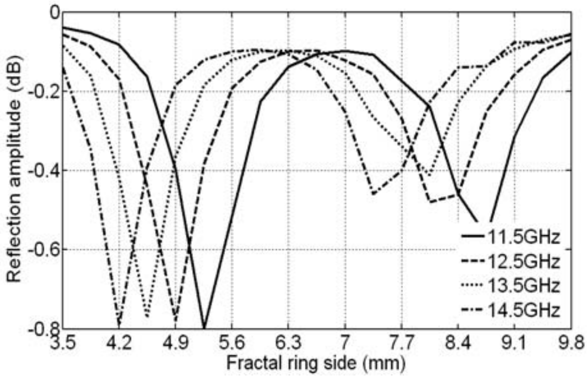

Fig. 6. The reflection amplitude at normal incidence for a periodic array of fractal ring on a grounded substrate versus the fractal ring side at four frequencies on the top surface of the patch.

Figure 7 shows the phase of the reflected wave versus the fractal ring side of a radiating element when a plane wave impinges with different angles of incidence. This structure was simulated using HFSS with floquet port and master slave boundary. As shown in Fig. 7, there is a small variation as the incident angle changes. Thus, the effect of the incident angle in designing of the reflectarray is negligible.

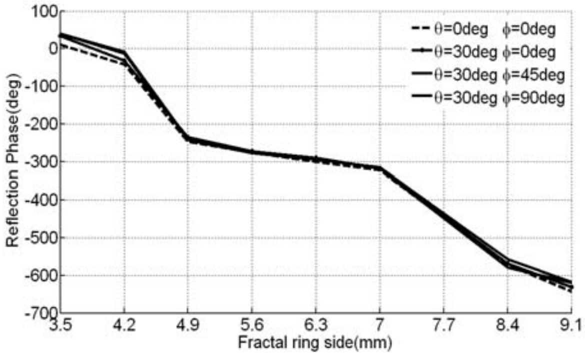

Fig. 7. Phase of the reflected wave versus fractal ring side for plane wave excitation with different incident angle at a center frequency of 13.5 GHz.

III. VALIDATION IN WAVEGUIDE SIMULATOR

To validate the simulation result, five elements has been fabricated and tested using waveguide simulator technique [14]. In this technique, the radiating elements were inserted into a waveguide section, and the reflection is measured in the excitation port. The simulations were obtained by defining the corresponding geometry in HFSS. The measurement setup for Ku band is shown in Fig. 8. In this approach, the cell size is 15.8 mm × 7.9 mm equal to WR62 dimensions. The length of the fractal ring is changed from 3.5 mm to 6.3 mm, as shown in Figs. 9 and 10, respectively. As can be seen, the agreement between the simulation and the measurement result is good. The reason of a small discrepancy between results is due to the tolerance in the manufacturing process and also due to the difference between the real losses of the material and the nominal value.

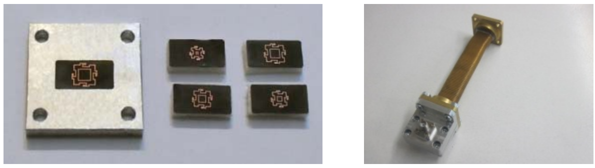
(a) (b)

Fig. 8. Waveguide simulator (a) five fabricated unit cells and (b) WR62 waveguide.

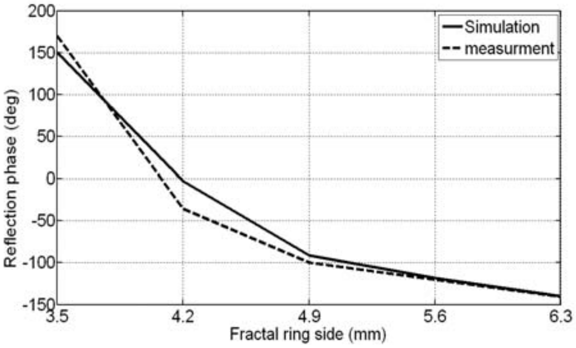

Fig. 9. Simulated and measured reflection phase for varying fractal ring side at a center frequency of 13.5 GHz and 44.68^0 incidence angle.

IV. REFLECTARRAY ANTENNA DESIGN AND PERFORMANCE

First step to design a reflectarray is determining the phase pattern on the reflectarray surface. The required phase delay at element *n* to achieve a reflected beam in a given direction (θ_0, ϕ_0) is

$$\phi_l = K_0[d_l - sin\theta_0(x_l cos\varphi_0 + y_l sin\varphi_0)], \quad (1)$$

where (x_l, y_l) are the coordinate of element *n*, K_0 is the wave number, d_l is the distance from the phase center of the feed to the element *n*, and (θ_0, ϕ_0) is the main beam direction. For example, for a reflectarray with 441 elements arranged in a square grid of 21 × 21 elements and *f/D* ratio equal 1, the phase distribution required for each element to generate a pencil beam at boresight is shown in Fig. 11. The required phase range is 600^0, which is achievable using the proposed cell.

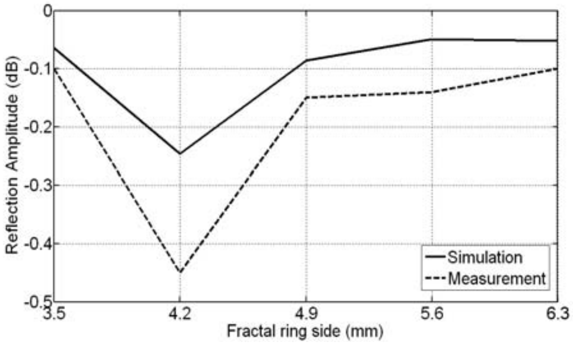

Fig. 10. Simulated and measured reflection amplitude for varying fractal ring side at a center frequency of 13.5 GHz and 44.68^0 incidence angle.

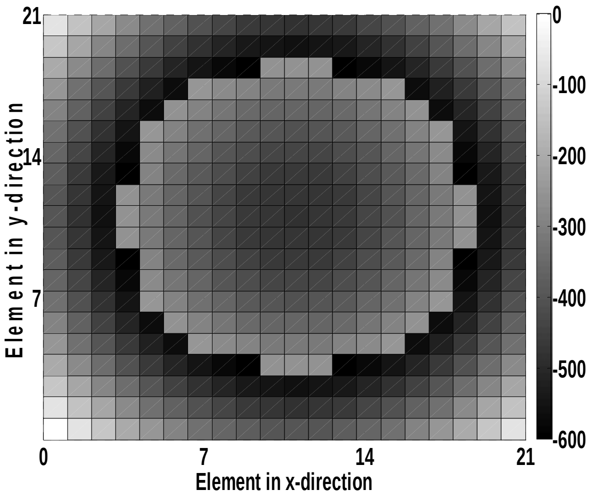

Fig. 11. Required phase distribution on the reflectarray surface to generate a pencil beam pointing on boresight.

Using the above equation, a 250 mm square center-fed reflectarray using the aforementioned cell elements was designed and fabricated as shown in Fig. 12.

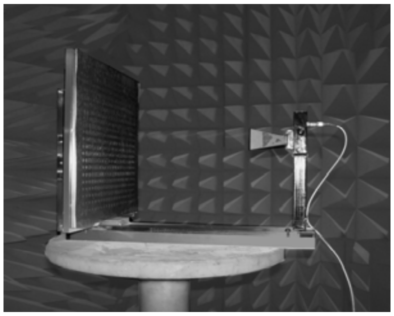

Fig. 12. Photographs of the one layer proposed reflectarray.

In order to illuminate the reflectarray, a standard linear polarity ATM horn 62-441-6 was selected. The measured gain for this horn at 13.5 GHz is 15 dB. The co- and cross-polarized radiation patterns at the center frequency of 13.5 GHz are shown in Figs. 13 and 14, respectively. As shown in these figures, the isolation between the co- and cross-polarized in the E- and H-Planes is better than 25 dB in the boresight direction and the side lobe level is around 13 dB.

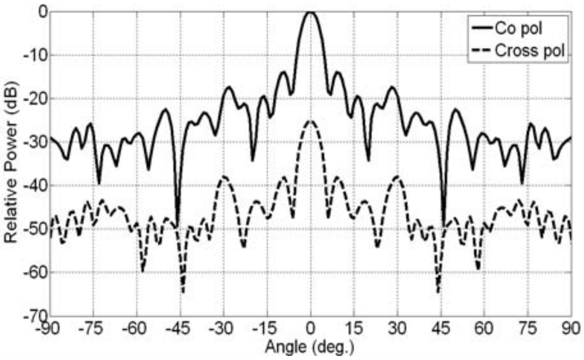

Fig. 13. Simulated vertical E-plane radiation pattern of a reflectarray at 13.5 GHz.

The measured gain over the frequency range from 11 GHz to 16 GHz is shown in Fig. 15, which demonstrates a 1 dB gain bandwidth close to 17 %. This is considered an excellent result. The aperture efficiency was computed as the ratio of measured gain to the maximum directivity [15]. The efficiency of this reflectarray is about 50 %. To attain higher efficiency one should reduce the blockage attributed to the feed antenna, the spillover effect due to the feed illuminating areas outside of the reflectarray, the feed's non-uniform illumination across the reflectarray's aperture, and the diffracted fields from the edges.

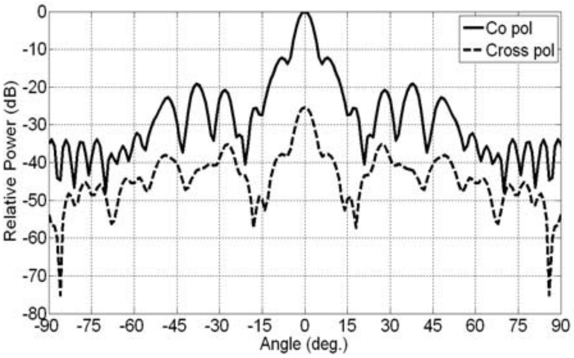

Fig. 14. Simulated horizontal H-plane radiation pattern of a reflectarray at 13.5 GHz.

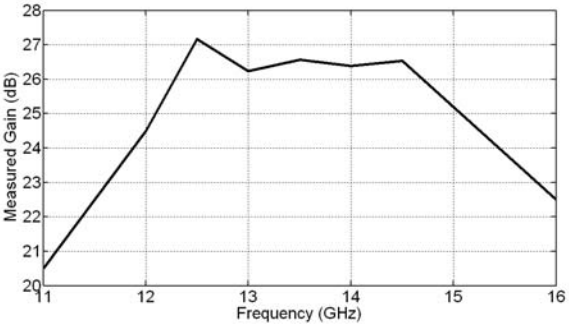

Fig. 15. Measured gain of the prototype reflectarray versus the frequency range.

V. CONCLUSION

A single layer microstrip reflectarray element with fractal and square ring elements has been designed and analyzed. Compared with other reflectarray elements, this element can produce a phase variation range exceeding 600^0. By using these elements a 441 element reflectarray operating at 13.5 GHz with 1 dB gain bandwidth of 17 % has been designed and tested. Good agreement between the simulation and measured result has been observed.

ACKNOWLEDGMENT

The authors thank the Iranian Telecommunication Research Center for its financial support under project contract number 11677/500.

REFERENCES

[1] J. Huang, "Microstrip reflectarray," *IEEE AP-S/URSI Symp.*, London, Canada, pp. 612-615, June 1991.

[2] S. H. Yusop, N. Misran, M. T. Islam, and M. Y. Ismail, "Design of high performance dual frequency concentric split ring square element for broadband reflectarray antenna," *Applied Computational Electromagnetics Society (ACES) Journal*, vol. 27, no. 4, pp. 334-339, April 2012.

[3] G. Zhao and Y. Jiao, "Design of broadband dual-polarization contoured-beam reflectarray for space applications," *28th Annual Review of Progress in Applied Computational Electromagnetics (ACES)*, pp. 790-794, Columbus, Ohio, April 2012.

[4] B. Devireddy, A. Yu, F. Yang, and A. Z. Elsherbeni, "Gain and bandwidth limitations of reflectarrays," *Applied Computational Electromagnetics Society (ACES) Journal*, vol. 26, no. 2, pp. 170-178, Feb. 2011.

[5] J. A. Encinar, "Design of two-layer printed reflectarrays using patches of variable size,"*IEEE Transactions on Antennas and Propagation*, vol. 49, no. 10, pp. 1403-1410, Oct. 2001.

[6] J. A. Encinar and J. A. Zornoza, "Broadband design of three-layer printed reflectarrays," *IEEE Transactions on Antennas and Propagation*, vol. 51, no. 7, pp. 1662- 1664, July 2003.

[7] F. –C. Tsai and M. E. Bialkowski, "Designing a 161-element Ku-band microstrip reflectarray of variable size patches using an equivalent unit cell waveguide approach," *IEEE Transactions on Antennas and Propagation*, vol. 51, no. 10, pp. 2953-2962, Oct. 2003.

[8] Q.-Y. Li, Y.-C. Jiao, and G. Zhao, "A novel microstrip rectangular patch/ring combination reflectarray element and its application," *IEEE Antennas and Wireless Propagation Letters*, vol. 8, pp. 1119-1122, Oct. 2009.

[9] D. M.Pozar, "Wideband reflectarrays using artificial impedance surfaces," *Electronics Letters*, vol. 43, no. 3, pp. 148-149, Feb. 2007.

[10] M. R. Chaharmir and J. Shaker, "Broadband reflectarray with combination of cross and rectangle loop elements," *Electronics Letters*, vol. 44, no. 11, pp. 658-659, May 2008.

[11] E. Carrasco, M. Barba, and J. A. Encinar, "Design and validation of gathered elements for steerable-beam reflectarrays based on patches aperture-coupled to delay lines," *IEEE Transactions on Antennas and Propagation*, vol. 59, no. 5, pp. 1756-1761, May 2011.

[12] H. Oraizi and S. Hedayati, "Miniaturized UWB monopole microstrip antenna design by the combination of Giuseppe Peano and Sierpinski

carpet fractals," *IEEE Antennas and Wireless Propagation Letters*, vol. 10, pp. 67-70, 2011.

[13] "Ansoft HFSS," "The 3D, Electromagnetic, Finite-Element Simulation Tools for High-Frequency Design," Available: http://www.ansoft.com.

[14] P. W. Hannan and M. A. Balfour, "Simulation of a phased-array in waveguide," *IEEE Transactions on Antennas and Propagation*, vol. 13, pp. 342-353, May 1965.

[15] D. M. Pozar, S. D. Targonski, and H. D. Syrigos, "Design of milimeter wave microstrip reflectarrays," *IEEE Transactions on Antennas and Propagation*, vol. 45, pp. 287-296, Feb. 1997.

Mohsen Maddahali received the B.Eng. degree in Electronics and Telecommunications from the Isfahan University of Technology, Isfahan, Iran, in August 2005 and the M.Sc. degree in Electrical Engineering from Tarbiat Modares University, Tehran, Iran in August 2008. He is currently working toward the Ph.D. degree at Tarbiat Modraes University. His research interests include characterization of reflectarray elements, microstrip and slot array and phase array antenna.

Keyvan Forooraghi was born in Tehran, Iran. He received the M.Sc. from the Technology Licentiate and PhD from Chalmers University of Technology, Gothenburg, Sweden in 1983, 1988, and 1991 respectively, all in Electrical Engineering. He was a researcher at the Department of Network Theory during 1992-1993. He joined the department of electrical engineering at Tarbiat Modares University (TMU) in 1993 where he currently is a professor and lectures on electromagnetic, antenna theory and design, and microwave circuits. His research interests include computational electromagnetic, waveguide slot antenna design and microstrip antennas.

Enhanced Bandwidth Small Square Slot Antenna with Circular Polarization Characteristics for WLAN/WiMAX and C-Band Applications

Mohammad Ojaroudi [1], Nasser Ojaroudi [2], and Noradin Ghadimi[1]

[1] Young Researchers Club
Ardabil Branch, Islamic Azad University, Ardabil, Iran
m.ojaroudi@iauardabil.ac.ir and noradin.ghadimi@gmail.com

[2] Department of Electrical Engineering
Ardabil Branch, Islamic Azad University, Ardabil, Iran
n_ojaroudi@srttu.edu

Abstract **─** This article proposes a novel printed slot antenna with circular polarization characteristics using an L-shaped slot in the ground plane and an L-shaped radiating stub with a pair of Γ-shaped slits for simultaneously satisfying wireless local area network (WLAN), worldwide interoperability for microwave access (WiMAX), and C-Band applications. The operating frequencies of the proposed antenna are 5.2/5.8 GHz, which covers WLAN system, 5.5 GHz for WiMAX system, and 4 GHz for C-Band system. The desired resonant frequencies are obtained by adjusting the length of Γ-shaped slits in the both sides of tapered microstrip feed-line. The measured results show good agreement with the numerical prediction. The designed antenna has a small size of 20 × 20 mm^2.

Index Terms **─** Circular polarization performance, Γ-shaped slit, and printed square slot antenna.

I. INTRODUCTION

Circular polarization is one of the common polarization schemes used in current wireless communication systems, such as radar and satellite systems. This is due to the fact that it can provide better mobility and weather penetration than linear polarization microstrip patch antenna [1], spiral antenna [2], dielectric resonator antenna [3], and slot antenna [4], which are some of the typical types of circularly polarized (CP) antennas. The operation principle of these CP antennas is to excite two orthogonal field components with equal amplitudes.

In this paper, a new printed square slot antenna with single-feed circular polarization characteristics, for WLAN/WiMAX and C-Band applications is presented. First by inserting an L-shaped slot on the ground plane, additional resonances are excited and the bandwidth is improved that achieves a fractional bandwidth with dual resonance performance of more than 45%. In the proposed structure, wide band circular polarization function is provided by cutting an L-shaped slot on the ground plane and a pair of Γ-shaped slits in the corners of the L-shaped radiating stub. The size of the designed antenna is smaller than the slot antennas with circular polarization function reported recently [1-4].

II. ANTENNA DESIGN

The proposed square slot antenna fed by a microstrip line is shown in Fig. 1, which is printed on an FR4 substrate of thickness 0.8 mm, and permittivity 4.4. By cutting a novel slot of suitable dimensions at the ground plane, circular polarization can be constructed. The truncated ground plane and L-shaped radiating stub with two Γ-shaped slits are playing an important role in the circular polarization characteristics of this antenna. This is because they can adjust the electromagnetic coupling effects between the feed-

Submitted On: June 11, 2012
Accepted On: Dec. 25, 2012

line and the ground plane, and improves its impedance bandwidth without any cost of size or expense [4]. Based on electromagnetic coupling, the modified L-shaped radiating stub with a pair of Γ-shaped slits act as an impedance matching element to control the impedance bandwidth of the proposed antenna. Because it can creates additional surface current paths in the antenna and thus additional resonances are excited and much wider impedance bandwidth can be produced [5].

In this work, we start by choosing the aperture length L_s+L_{s1}. We have a lot of flexibility in choosing this parameter. The length of the aperture mostly affects the antenna bandwidth. As L_s+L_{s1} decreases, so does the antenna BW and vice versa. At the next step, we have to determine the aperture width W_s+W_{s1}. The aperture width is approximately $\lambda_s/2$, where λ_s is the slot wavelength. The wavelength λ_s depends on a number of parameters such as the slot width as well as the thickness and dielectric constant of the substrate on which the slot is fabricated. The last and final step in the design is to choose the length of the Γ-shaped slits resonators. A good starting point is to choose it to be equal to $\lambda_m/4$, where λ_m is the guided wavelength in the microstrip line. In this design, the optimized length $L_{resonance}$ is set to resonate at $0.25\lambda_{resonance}$, where $L_{resonance1} = W_{L1} + W_{L2} + L_L$ and $L_{resonance2} = W_{L3} + W_{L4} + L_{L1} + L_f$. $\lambda_{resonance1}$ and $\lambda_{resonance2}$ correspond to the first resonance frequency (4 GHz) and the second resonance frequency (5.3 GHz), respectively. The final values of presented slot antenna design parameters are specified in Table 1.

Table 1: The final dimensions of the designed antenna.

Param.	mm	Param.	mm	Param.	mm
W_S	8	L_S	6	W_{S1}	8
L_{S1}	7	W_f	0.5	W_{f1}	2
W_L	4	L_L	8	W_{L1}	3
L_{L1}	2	W_{L2}	4	W_{L3}	2
W_{L4}	2	L_g	2	W_g	3

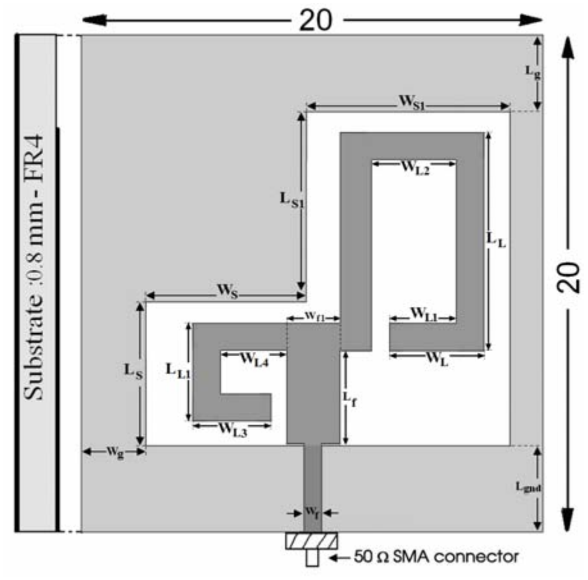

Fig. 1. Geometry of the proposed microstrip-fed slot antenna.

III. RESULTS AND DISCUSSIONS

In this Section, the slot antenna with various design parameters were constructed, and the numerical and experimental results of the input impedance and axial ratio characteristics are presented and discussed. The parameters of this proposed antenna are studied by changing one parameter at a time and fixing the others. The simulated results are obtained using the Ansoft simulation software high-frequency structure simulator (HFSS) [6].

Figure 2 shows the structure of the various antennas used for wide-band impedance and circular polarization performance simulation studies. Return loss and axial ratio characteristics for ordinary square slot antenna with an L-shaped radiating stub and ground plane with a rectangular slot (Fig. 2 (a)), a ground plane with an L-shaped slot (Fig. 2 (b)), and L-shaped radiating stub with a pair of Γ-shaped slits and ground plane with an L-shaped slot (Fig. 2 (c)) are all compared in Fig. 3. As shown in Fig. 3 (a) and (b), in order to generate dual resonance characteristics (4/5.3 GHz), and to improve the circular polarization bandwidth, we use two L-shaped slits in the corners of the radiating stub. Also, by cutting an L-shaped slot in the ground plane a wide band circular polarization function is achieved that cover all the 5.2/5.8 GHz WLAN, 5.5 GHz WiMAX and 4-GHz C band.

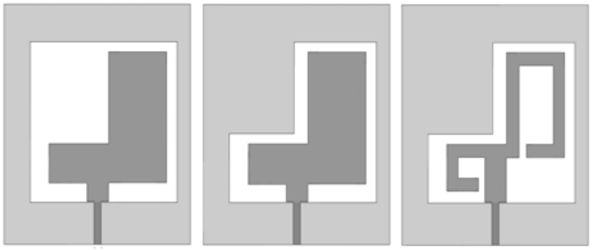
(a) (b) (c)

Fig. 2. The ordinary square slot antenna with an L-shaped radiating stub (a) and ground plane with a rectangular slot, (b) and ground plane with an L-shaped slot, (c) with a pair of Γ-shaped slits and ground plane with an L-shaped slot.

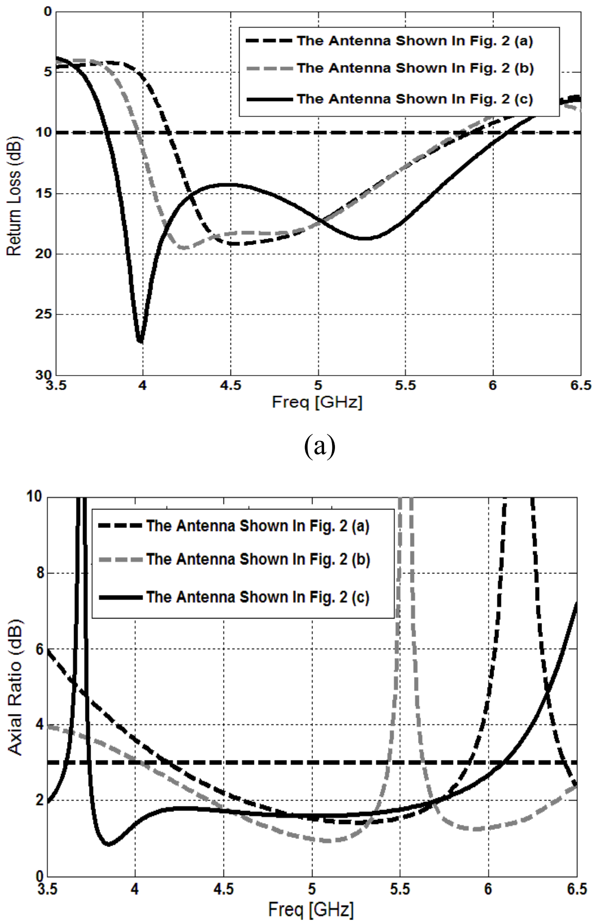

(a)

(b)

Fig. 3. Simulated (a) return loss characteristics and (b) axial ratio for the antennas shown in Fig. 2.

To understand the phenomenon behind this dual resonances performance, the simulated current distribution on the radiating stub for the proposed antenna at the new resonance frequencies of 4 GHz and 5.3 GHz are proposed at Fig. 4 (a) and (b), respectively. It can be observed from Fig. 4 (a) and (b) that the current is concentrated at these frequencies on the edges of the interior and exterior of the modified Γ-shaped folded microstrip arms. Therefore, the antenna impedance changes at these frequencies due to the resonance properties of the proposed structure.

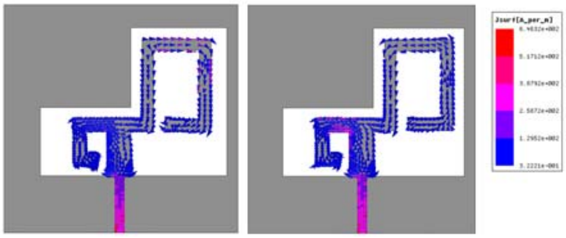
(a) (b)

Fig. 4. Simulated surface current distributions for the proposed antenna shown in Fig. 1 at, (a) 4 GHz (first resonance frequency) and (b) 5.3 GHz (second resonance frequency).

In order to investigate the effects of Γ-shaped slits size on the proposed antenna, the simulated return curves with different values of Γ-shaped slits lengths are plotted in Fig. 5. As shown in Fig. 5, when W_L increases from 2 mm to 4.8 mm, the first resonance frequency is varied from 4.3 GHz to 3.8 GHz. From these results, we can conclude that the first resonance frequency is controllable by changing the W_L. Also, as the W_{L3} increases from 1.3 mm to 2.8 mm, the second resonance frequency is varied from 5.1 GHz to 5.5 GHz. Therefore, the second resonance frequency is controllable by changing the W_{L3}.

In this study, to achieve the circular polarization characteristics, we use two Γ-shaped folded microstrip arms in the radiating stub and an L-shaped slot on the ground plane, as displayed in Fig. 1. By changing the dimension of these open stub structures, we can achieve the RHCP and RLCP characteristics. The simulated RHCP and RLCP curves at 4 GHz and 5.3 GHz are presented in Fig. 6 (a) and (b), respectively. These figures confirm that the proposed antenna is capable of supporting both RHCP and RLCP modes at these frequencies. The proposed slot antenna with final design, as shown in Fig. 7, was built and tested.

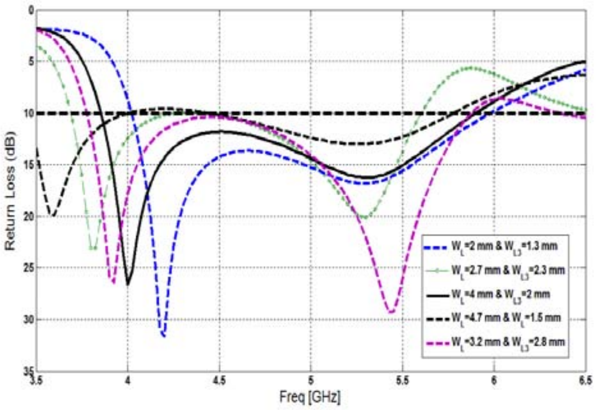

Fig. 5. Simulated return loss characteristics of the proposed antenna with different values of W_L and W_{L3}.

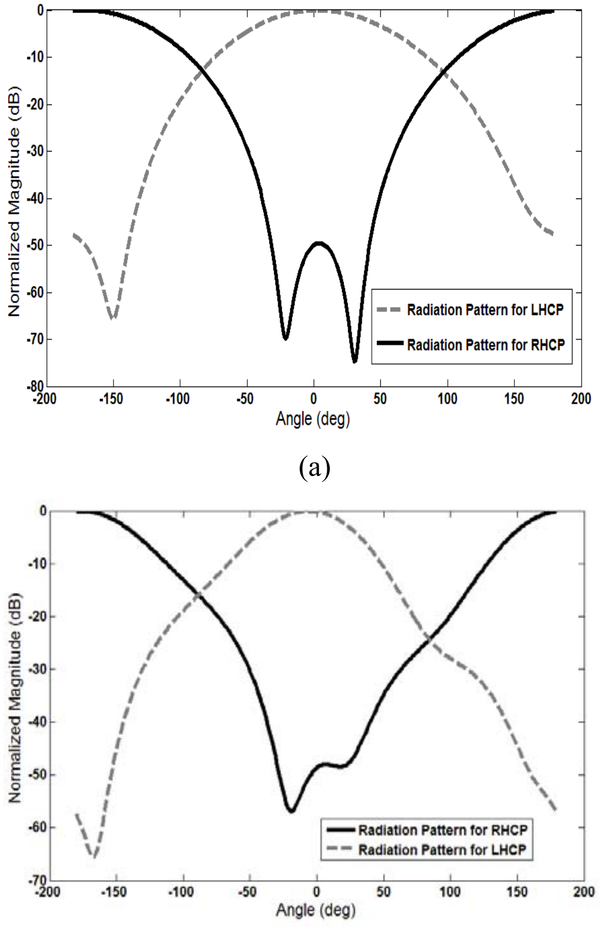

(a)

(b)

Fig. 6. Simulated circularly-polarized radiation patterns at (a) 4 GHz (first resonance frequency) and (b) 5.3 GHz (second resonance frequency).

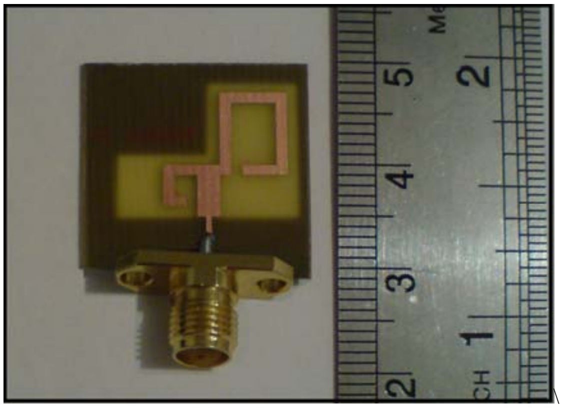

Fig. 7. Photograph of the realized printed slot antenna.

Figure 8 (a) and (b) shows the measured and simulated return loss and axial ratio characteristics of the proposed antenna, respectively. As shown in Fig. 8 (a) and (b), the fabricated antenna has the frequency band of 3.73 GHz to over 6.07 GHz with circular polarization characteristics 3.72 GHz - 6.05 GHz. As shown in Fig. 8, there exists a discrepancy between the measured data and the simulated results. This could be due to the effect of the SMA port. In order to confirm the accurate return loss and axial ratio characteristics for the designed antenna, it is recommended that the manufacturing and measurement process need to be performed carefully.

Figure 9 shows measured maximum gain of the designed antenna in dBi, in the Z-axis direction. A two-antenna technique is used to measure the radiation gain. As shown in Fig. 9, the measured maximum gain has a variation similar to other slot antennas gain at WLAN/ WiMAX and C-band frequencies [7].

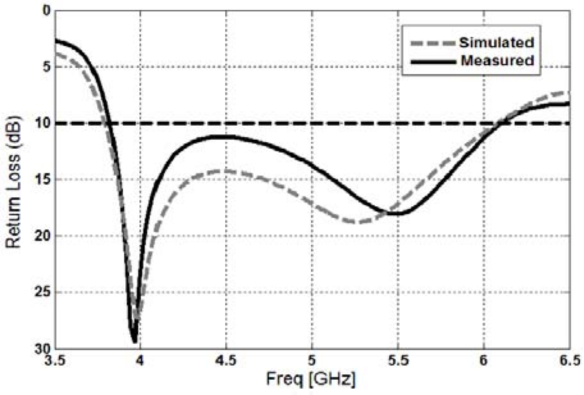

(a)

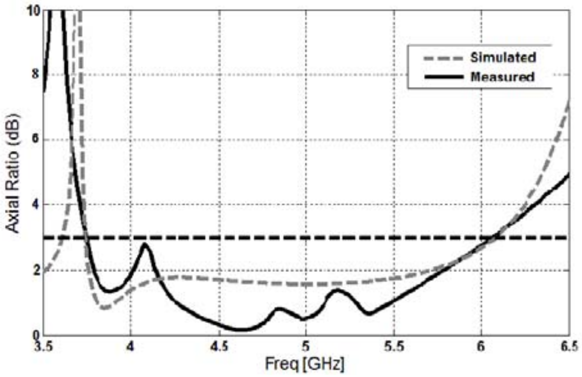

(b)

Fig. 8. Measured and simulated (a) return loss characteristics and (b) axial ratio characteristics for the proposed antenna.

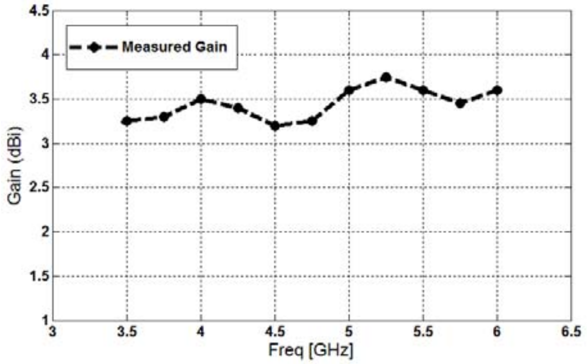

Fig. 9. Measured maximum gain of the proposed antenna.

IV. CONCLUSION

In this paper, a novel square slot antenna with circular polarization characteristics for WLAN/WiMAX and C-band applications is presented. The proposed antenna can operate from 3.73 GHz to 6.07 GHz with circular polarization characteristics around 3.72 GHz - 6.05 GHz. The designed antenna has a small size. Simulated and experimental results show that the proposed antenna could be a good candidate for WLAN/WiMAX and C-band applications.

ACKNOWLEDGMENT

The authors are thankful to Microwave Technology (MWT) Company staff for their beneficial and professional help (www.microwave-technology.com).

REFERENCES

[1] K. L. Wong, F. S. Chang, and T. W. Chiou, “Low-cost broadband circularly polarized probe-fed patch antenna for WLAN base station,” *IEEE Antennas Propag. Soc. Int. Symp.*, vol. 2, pp. 526–529, 2002.

[2] J. D. Kraus, *Antennas*, 2nd ed. New York: McGraw-Hill, 1988, ch. 7.

[3] S. Yazdanifard, R. A. Sadeghzadeh, and M. Ojaroudi, “Ultra-wideband small square monopole antenna with variable frequency band notch function,” *Progress in Electromagnetics Research C*, vol. 15, pp. 133-144, 2010.

[4] G. Beigmohammadi, C. Ghobadi, J. Nourinia, and M. Ojaroudi, “Small square slot antenna with circular polarisation characteristics for WLAN/WiMAX applications,” *Electronics Letters*, vol. 46, no. 10, pp. 672-673, 2010.

[5] M. Ojaroudi and A. Faramarzi, “Multi-resonance small square slot antenna for Ultra-wideband applications,” *Microwave and Optical Tech. Letters*, vol. 53, no. 9, Sep. 2011.

[6] Ansoft High Frequency Structure Simulation (HFSS), ver. 13, *Ansoft Corporation*, 2010.

[7] M. -J. Chiang, T. -F. Hung, and S. -S Bor, “Dual-band circular slot antenna design for circularly and linearly polarized operations,” *Microwave and Optical Tech. Letters.*, vol. 52, no. 12, pp. 2717-2721, Dec. 2010.

Mohammad Ojaroudi was born on 1984 in Germi, Iran. He received his B.Sc. degree in Electrical Engineering from Azad University, Ardabil Branch and M.Sc. degree in Telecommunication Engineering from Urmia University. From 2010, he has been working toward the Ph.D. degree at Shahid Beheshti University. From 2007 until now, he is a Teaching Assistant with the Department of Electrical Engineering, Islamic Azad University, Ardabil Branch, Iran. Since March 2008, he has been a Research Fellow (Chief Executive Officer) in the microwave technology company (MWT), Tehran, Iran. His research interests include analysis and design of microstrip antennas, design and modeling of microwave structures, radar systems, and electromagnetic theory.

Nasser Ojaroudi was born on 1986 in Germi, Iran. He received his B.Sc. degree in Electrical Engineering from Islamic Azad University, Ardabil Branch. From 2011, he is working toward the M.Sc. degree in Telecommunication Engineering at Shahid Rajaee Teacher Training University. Since March 2008, he has been a Research Fellow in the Microwave Technology (MWT) Company, Tehran, Iran. His research interests include ultra-wideband (UWB) microstrip antennas and band-pass filters (BPF), reconfigurable structure, design and modeling of microwave device, and electromagnetic wave propagation. He is author and coauthor of more than fifty journal and international conference papers.

Noradin Ghadimi was born in Ardabil-Iran in 1985, and received the B.Sc. degree in electrical engineering from the Islamic Azad University, Ardabil Branch, Ardabil, Iran, in 2009 and the M.Sc. degree in electrical engineering from the Islamic Azad University Ahar Branch, Ahar, Iran, in 2011. His research interests include Power System Protection, modeling and analysis of Distributed Generations, renewable energy and communications systems.

Eccentricity Compensation in Switched Reluctance Machines via Controlling Winding Turns/Stator Current: Theory, Modeling, and Electromagnetic Analysis

E. Afjei[1], M. R. Tavakoli[1], and H. Torkaman[2]

[1] Faculty of Electrical and Computer Engineering
Shahid Beheshti University, G. C. Tehran, Iran
E_Afjei,@sbu.ac.ir

[2] Faculty of Electrical and Computer Engineering
Power and Water University of Technology, Tehran, Iran
E_Afjei@sbu.ac.ir and H_Torkaman@sbu.ac.ir

Abstract **─** In this paper, a new eccentricity compensation method for Switched Reluctance Machines (SRMs) is presented. In this regard, the dependency of radial force (RF) on variation of number of turns for stator coils and fault level is demonstrated analytically and principle of the new compensation strategy is introduced as well. This strategy is implemented on an SRM utilizing Finite Element Method (FEM) under different fault conditions. This approach is accomplished through switching among the various arrangements in the number of turns for the coils on the stator poles; hence, unbalanced magnetic force (UMF) is controlled without additional auxiliary coils. Simultaneously, regulating the stator currents guarantees the motor torque is not diminished. This comprehensive approach is suitable for different types and structures of SRMs and will compensate or control eccentricities in a wide range of eccentricity faults namely 10%-70% while motor performance is not impaired.

Index Terms - Electromagnetics characteristics, eccentricity compensation, finite element analysis, fault control, and switched reluctance machines.

I. INTRODUCTION

SRM has been a charming choice for industrial and household applications due to its advantageous characteristics such as simplicity in winding and manufacturing, durability, and rotor permissible temperature [1, 2].

SRM air gap is considered to be uniform for ideal operation, which is smaller compared to other types of machines [3]. When there are uneven air gaps between stator and rotor poles eccentricity fault will happen [4]. Eccentricity fault results in excessive vibration, noise, bearing wear, and UMF. They change flux pattern and flux density distribution and accordingly causes some errors in motor control, rotor position estimation, and also considerable effects on produced torque [5, 6].

In the fabrication process a relative eccentricity between the stator and rotor axes up to 10% is common [7] and therefore the faulty conditions are assigned to those of more than this value, which must be controlled or compensated to prevent motor from irreparable damages. In this regard, in [8] artificial intelligence like Neuro-Fuzzy controller is suggested to compensate manufacturing inaccuracies namely eccentricity. This strategy is simulated for a 6/4 SRM and minimizes the torque ripple; however, a reduction in average torque is expected.

A remedial strategy for eccentricity via controlling current in each coil proposed in [9]. It puts forward that, to control eccentricity the current magnitude of each coil should be controlled separately. And through augmenting and mitigating current intensity in the facing poles reduces the UMF. In [10], eccentricity effects in a 12/8 SRM has been reduced by some modifications in stator windings. It shows that if in every phase, the four poles be connected such that

Submitted On: June 5, 2012
Accepted On: Dec. 26, 2012

they create two parallel paths with neighboring coils in series with an equalizer, the UMF will be lessened significantly. This strategy seems useful in 33 % eccentricity but it is not analyzed that for higher degrees of eccentricity this scheme will be such helpful too or not. Also this winding configuration is just suitable for those other SRMs, which have four stator poles per phase but no other configurations. The possibility of different winding methods and their features under various type of faults in a 6/4 SRM has been reported in [11]. It proposes six winding configurations and discusses their main characteristics under open circuit and short circuit conditions and then different detection possibilities are suggested but obviously the focus is not on mechanical faults like off-center rotor. The substantial effect of parallel stator winding on reduction of UMF in eccentric rotor in induction and synchronous machines has been discussed and evaluated in [12, 13].

As it can be seen in available papers in the literature, little portion is dedicated to eccentricity compensation in SRMs. Considering that each of these mentioned methods are intended for a particular SRM design, a more comprehensive strategy is needed to satisfy different motor structures.

In the previous works, authors have assessed SE (static eccentricity) [14], DE (dynamic eccentricity) [15], ME (mixed eccentricity) [16], and AE (axial eccentricity) [17] in the SRM. In this paper, a novel approach is proposed to compensate eccentricity in SRM. In this method by changing the arrangement of stator winding turns, not only UMF will be mitigated significantly, but also the motor torque will be kept around its nominal value, which is accomplished by controlling the stator current.

II. PROBLEM STATEMENT

One of the common faults in SRM is eccentricity. Eccentricity faults change SRM characteristics through making the produced magnetic field and flux distribution non-uniform. This asymmetry leads to an unbalanced flux density in front of two opposite poles of one excited phase, which results in a huge UMF acting on the rotor. This phenomenon brings about excessive vibration, noise, bearing wear, and irreparable damages.

UMF is the difference between two large RFs produced by two facing coils. These RFs are exerted on the opposite rotor poles, so through counterbalancing the ampere-turns in every two facing coils, UMF could be mitigated. This idea is accomplished by modifying arrangements of number of turns in each coil and regulating the stator current.

It is needed first that the relation among the RFs and motor torque with number of turns and stator current be investigated. Thus, in section III a linear model for RFs is presented and then the analytical model of the new method is demonstrated.

III. ANALYTICAL MODEL OF THE NEW METHOD

A precise model is needed for the physical motor simulation to incorporate the essential dynamics of the motor [18-21]. In literatures such as [22] a very detailed analytical model for RF is presented. However, here a simplified and linear analytical model is employed to predict the RFs on individual stator poles and the UMF on the rotor. These expressions will be derived just for those rotor positions where the rotor and stator overlap. In this model it is assumed that all of the magnetic energy is stored in the air gap where the B-H curve is given by,

$$\vec{B} = \mu_o \vec{H} \tag{1}$$

where μ_0 is the permeability of air, B is flux density, and H is magnetic field intensity, which can be calculated using the following equation,

$$\vec{H} = \frac{Ni}{g} \tag{2}$$

where N is the number of turns, i is the magnitude of current in each stator coil and g is the radial air gap length in the case of uniform air gap in healthy motor. Also, the flux equation can be given by,

$$\varphi = B.A \quad . \tag{3}$$

The symbol A is the surface of overlapping region of rotor and stator poles (Fig. 1), which can be evaluated using the following equation,

$$A = l_r r_r \theta \tag{4}$$

where r_r is the radius of rotor so $r_l\theta$ is the arc for overlapping region and l_r is the length of the rotor. By considering equations (1) to (4), the flux linkage can be defined as follow,

$$\lambda = N\varphi = \frac{\mu_o N^2 A}{g} i = \frac{\mu_o N^2 (l_r r_r \theta)}{g} i \ . \qquad (5)$$

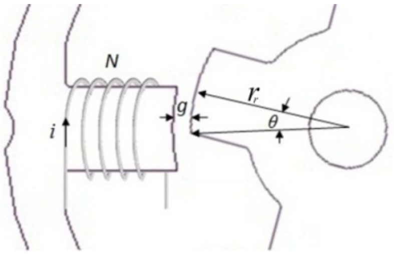

Fig. 1. Configuration of SRM for one pole.

The co-energy (W_f') for each pole due to λ is given by

$$W_f' = \oint \lambda \, di = \oint \frac{\mu_o N^2 A}{g} i \, di = \frac{\mu_o N^2 (l_r r_r \theta)}{2g} i^2 \ . \qquad (6)$$

The RF produced by every pole can be obtained from the rate of change in co-energy with respect to the air gap. So the RF (F_r) will be easily derived by

$$F_r = \frac{\partial W_f'}{\partial g} = -\frac{\mu_o N^2 (l_r r_r \theta)}{2g^2} i^2 \ . \qquad (7)$$

Torque will be achieved by the rate of change in co-energy with respect to the rotor position, as follows,

$$T = \frac{\partial W_f'}{\partial \theta} = \frac{\mu_o N^2 l_r r_r}{2g} i^2 \ . \qquad (8)$$

The unbalanced RFs acting on the rotor are calculated assuming that stator poles on opposite side of the machine are independent and this is the reason that electromagnetic energy has been computed per pole instead of per phase. Supposing an SE fault which means, rotor is off-center from stator symmetrical axes (Fig. 2) the degree of eccentricity will be given by,

$$\varepsilon = \left(\frac{\Delta}{g}\right) \times 100\% \qquad (9)$$

where Δ is the displacement of the rotor. Thus, the RF produced by poles 1 and 2 can be derived respectively by,

$$F_{r1} = \left.\frac{\partial W_f'}{\partial g}\right|_{g+\Delta} , \ F_{r2} = \left.\frac{\partial W_f'}{\partial g}\right|_{g-\Delta} \ . \qquad (10)$$

Furthermore, the UMF on the rotor is the sum of these forces

$$UMF = F_{r1} + F_{r2} \ . \qquad (11)$$

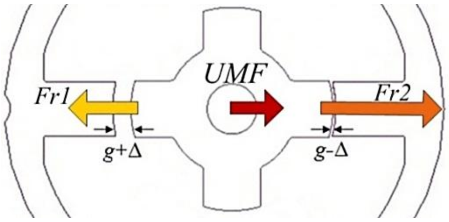

Fig. 2. Rotor is displaced from its symmetrical axes.

Due to the opposite direction of fluxes in two poles in one phase (i.e., λ is leaving one pole and entering into the other one) F_{r1} is exerted in the reverse direction with respect to F_{r2} on the rotor (Fig. 2). In the healthy condition, the magnitudes of these forces are equal so the overall force on the rotor is nearly zero, in other words, there is no UMF. But as it was shown up to here eccentricity causes that these RFs have different magnitudes and therefore the UMF will arise. It seems reasonable if it was possible to somehow balance the RFs on the opposite side of rotor the UMF will be diminished significantly. To nullify UMF there are two choices: a) augmenting the MMF on the pole where air gap has been increased (pole 1 in Fig. 2) or b) mitigating MMF on the opposite pole where air gap has been decreased (pole 2 in Fig. 2). Even a combination of both approaches is also possible.

Considering Fig. 2, let us develop equation (11) to see how analytically is possible to reduce this force

$$\begin{aligned} UMF &= F_{r1} + F_{r2} \\ &= \frac{\mu_o N_1^2 (l_r r_r \theta)}{2(g+\Delta)^2} i^2 - \frac{\mu_o N_2^2 (l_r r_r \theta)}{2(g-\Delta)^2} i^2 \\ &\begin{cases} g-\Delta & in\ front of\ Coil 1 \\ g+\Delta & in\ front of\ Coil 2 \end{cases} \ . \end{aligned} \qquad (12)$$

By rearrangement, UMF will be given by,

$$\begin{aligned} UMF &= \frac{1}{2} \frac{\mu_o (l_r r_r \theta_o) i^2}{(g-\Delta)^2 (g+\Delta)^2} \\ &\times \left(\left(N_1^2 - N_2^2\right)\left(g^2 + \Delta^2\right) - 2g\Delta\left(N_1^2 + N_2^2\right) \right) \ . \end{aligned} \qquad (13)$$

Equation (13) shows that displacement (Δ) directly affects UMF. There is no straight method to reach the degree of eccentricity but the occurrence of eccentricity and where it was happened is completely diagnosable. Thus, due to the dependence of RF on number of turns and current intensity in each coil, it is possible to diminish faults effects. Controlling currents means that two opposite coils of one phase must be energized separately, in other words, there must be either an electrical source for each one or having an independent set of power switches for each pole, which however, increases the total cost.

Assuming like most of typical SRMs, two opposite coils of one phase are connected in series, and considering i constant, equation (13) will be rewritten as,

$$UMF = K\left(\left(N_1^2 - N_2^2\right)\left(g^2 + \Delta^2\right) - 2g\Delta\left(N_1^2 + N_2^2\right)\right) \tag{14}$$

where K is given by,

$$K = \frac{1}{2}\frac{\mu_o\left(l_r r\theta_o\right)i^2}{\left(g-\Delta\right)^2\left(g+\Delta\right)^2} \,. \tag{15}$$

The symbol K depends on motor dimensions and cannot be zero. Noting equation (14) for an SRM in healthy condition where,

$$\begin{cases}\Delta = 0\\ N_1 = N_2\end{cases} \,. \tag{16}$$

UMF will be equal to zero. But in eccentric conditions for a typical SRM where,

$$\begin{cases}\Delta \neq 0\\ N_1 = N_2\end{cases} \,. \tag{17}$$

It is not possible for UMF to be zero. Supposing the possibility of changing the number of turns and developing equation (14) UMF will be zero on condition that

$$\begin{gathered} UMF = K\left(\left(N_1^2 - N_2^2\right)\left(g^2 + \Delta^2\right) - 2g\Delta\left(N_1^2 + N_2^2\right)\right) = 0\\ \left(N_1^2 - N_2^2\right)\left(g^2 + \Delta^2\right) - 2g\Delta\left(N_1^2 + N_2^2\right) = 0\\ \frac{N_2}{N_1} = \left(\frac{g-\Delta}{g+\Delta}\right) = 1 - \left(\frac{2\Delta}{g+\Delta}\right) \,. \end{gathered} \tag{18}$$

Assuming an SE fault (Fig. 2), equation (18) implies that if the turn's ratio between coils 2 and 1 be modified like this, UMF will be about zero. The advantage of this method here is that in the case of eccentricities faults there is no need to get the SRM removed from the production line to fix it anymore. There is the feasibility of remedial actions during SRM operation.

To modify turns ratio, it is possible to increase the number of turns in coil 1 (N_1), or decrease the number of turns in coil 2 (N_2). Increasing the number of turns means the existence of some additional windings that are idle in the healthy operation of motor, which requires some changes in its design structure and consequently all of these demand extravagant money. Thus, here the focus is just on decreasing the number of turns.

Considering equation (18), assuming coil 1 has 120 turns and is constant, the relationship between number of turns in coil 2 (N_2) and degree of eccentricity (ε) in order to cancel UMF is obtained and plotted in Fig. 3. As it can be seen in this figure there is a nonlinear relation between N_2 and ε.

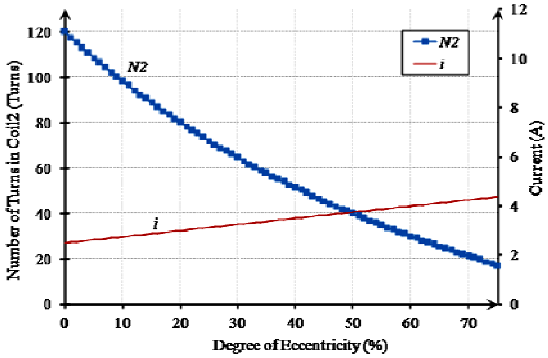

Fig. 3. The number of turns and stator current to nullify UMF and keeping the toque at its rated value, respectively for different degrees of eccentricity.

From Fig. 3, two noteworthy points can be deduced: a) to compensate high degrees of eccentricities, N_2 must be decreased very much; this is not possible because it will ruin the symmetrical structure of the motor. If the difference between the number of turns in adjacent poles becomes very much so the resultant MMF of these poles will vary greatly and consequently causes extra vibration indeed. Therefore, 40 % of the total number of turns is supposed to be the maximum number of turns to be decreased, which is 50 turns here. b) Another point is that according equation to (8) the torque produced by each stator pole has direct relation with square of the number of turns and current intensity,

$$T \propto N^2 \times i^2 \,. \tag{19}$$

Thus, regarding the reduction in the number of turns and assuming i constant, the overall torque will be lessened, which means the performance of motor will be deteriorated and that is not acceptable. Thus, to keep the torque at its nominal value i must be intensified. To develop an analytical model, let's start with equation (8),

$$T_1 = \frac{\mu_o N^2 l_r r_r}{2g} i^2 \quad . \tag{20}$$

This is the torque produced by one stator pole. The overall torque as a result of two facing poles in one phase in healthy condition will be given by

$$T_h = T_1 + T_2 = \frac{\mu_o N^2 l_r r_r}{g} i^2 \quad . \tag{21}$$

The above equation is for healthy operation of motor but in eccentric condition the torque will be given by

$$T_e = T_1 + T_2 = \frac{\mu_o {N_1}^2 l_r r_r}{2(g+\Delta)} i^2 + \frac{\mu_o {N_2}^2 l_r r_r}{2(g-\Delta)} i^2 \tag{22}$$

As it was mentioned earlier, the objective is that while N_2 is decreased to compensate eccentricity, the torque remains unchanged ($T_e \approx T_h$) or in acceptable range. So it can be accomplished through increasing i, equalizing equations (21) and (22)

$$T_e = T_h$$

$$\frac{\mu_o {N_1}^2 l_r r_r}{2(g+\Delta)} i_e^2 + \frac{\mu_o {N_2}^2 l_r r_r}{2(g-\Delta)} i_e^2 = \frac{\mu_o N^2 l_r r_r}{g} {i_h}^2 \tag{23}$$

Where i_h is the stator current in healthy condition and i_e is the stator current in eccentric condition. Let us suppose during a fault the number of turns in coil 1 is kept constant at its design number ($N_1 = N$) and number of turns in coil 2 is modified according to equation (18). So considering these assumptions, equation (23) will be simplified to,

$$\frac{i_e}{i_h} = 1 + \frac{\Delta}{g} \quad . \tag{24}$$

This equation emphasizes in order to maintain torque at a constant level while number of turns is decreased in eccentric condition the current must be increased, which is also demonstrated by Fig. 3. At this point this question may be raised that intensifying current to increase torque might augment UMF as well, and of course considering the assumption that in developing equation (18), i was supposed to be constant. It is essential to mention that this will not happen. As it is shown in section V when N_2 is decreased to 70 turns at its maximum reduction level, current must be increased from 2.5A to 3A, it is demonstrated by simulation that the effects of this addition will be negligible. In this section the theory of the new method was proved. The following section is dedicated to the analysis of the proposed compensation strategy.

IV. THE NEW COMPENSATION STRATEGY

To create the possibility of modifying the number of turns for each coil, a switching box is designed which has three power switches. These switches must be able to operate at the rated motor current, which is only 2.5A and the high frequency switching is not needed, so they can be any ordinary and cheap switch. Different combinations of these switches will produce different arrangement of number of turns. The configuration of the switching box for one phase is shown in Fig. 4. It must be mentioned that only one switching box is required for the proposed method. When a fault is diagnosed in one phase afterwards the pole, which its MMF should be reduced will be specified, and finally the terminal of the switching box will be connected to the windings of this coil of the faulty phase.

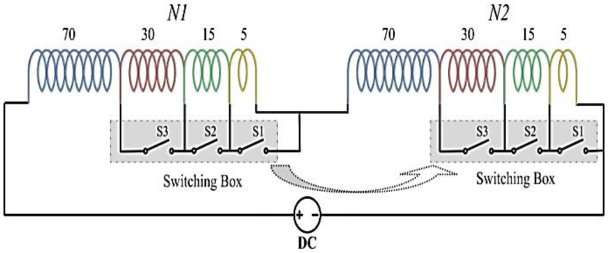

Fig. 4. Configuration of the switching box in phase.

In table 1 the complete combinations of a switching box and the resulting number of turns are listed. In healthy operation of motor the number of turns is 120 turns and all the switches are OFF (state 0). Each switch, which is turned ON means that the corresponding coil is removed (Fig. 4). So via different combination of switches, eight different number of turns are obtainable. Depending on the degree of eccentricity, the right state must be chosen. It is obvious that besides decreasing the number of turns, the current intensity must be increased to keep the torque at its nominal value. To do so, an algorithm has been used which its flowchart is shown in Fig. 5.

Table 1: Combinations of a switching box (0 : OFF and 1 : ON).

State	S3	S2	S1	Number of Turns
0	0	0	0	120
1	0	0	1	115
2	0	1	0	105
3	0	1	1	100
4	1	0	0	90
5	1	0	1	85
6	1	1	0	75
7	1	1	1	70

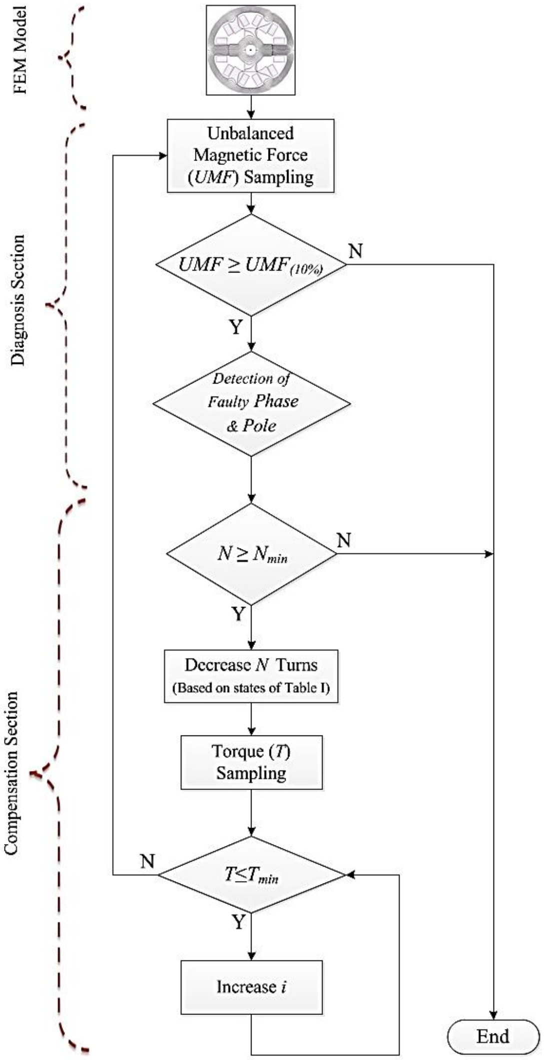

Fig. 5. Compensation strategy flowchart.

Based on the previous work of the authors, in this algorithm, UMF is sampled based on the proposed index in [23], if it is greater than UMF (10 %) it will be diagnosed as a fault. Now, the faulty phase must be determined and of course the pole, which its ampere-turn must be mitigated and should be specified too. This is viable via the procedure proposed in [24]. Because of tolerances in manufacturing and assembly process, a 10 % eccentricity is assumed to be natural and is not identified as a fault. Thus, the aim of compensation is to get back to this condition in case of eccentricities more severe than 10 %.

Now that it is clear which coil is going to be modified, in the next step it is examined that the number of turns in this coil has reached to its minimum level or not? For this motor the maximum number of turns is 120 and the minimum number is 70 turns. So at this point it is possible to go to the next step i.e., “Decrease *N* turns” because currently the number of turns is 120. In this stage, the switching box is changed to its next state (i.e., changing from state 0 to state 1) and accordingly decreases the number of turns to 115 turns. Moving to the following step, the torque must be sampled. If the torque is less than its minimum level, which is 90 % of the nominal value the current must be increased. In this stage current is augmented 0.1 A each time up until the torque reaches to the minimum level. The reason behind this minimum level is that due to the variations in manufacturing process and alterations from nominal load conditions it is not mostly possible to reach motor nominal torque, so 90 % is supposed to be the healthy performance of the motor. After restoring the torque, UMF is sampled again and if it is greater than UMF (10 %) the same procedure is followed once more. It is worth noting that in case of 40 % eccentricities and higher the number of turns reaches to its minimum (70 turns) and UMF is not less than its minimum value yet, then here the fault is compensated partially and procedure is terminated.

V. NEW METHOD IMPLEMENTATION ON SRM AND FEM RESULTS

A workbench of the test for a 6/4 SRM has been established utilizing FEM. Each phase winding consists of 120 turns with a current magnitude of 2.5A. This motor is driven for different conditions to assess the UMF in different percentages of eccentricities. Figure 6 shows UMF for different levels of eccentricities as a function of rotor position which varies from 0 to 44 degrees meaning a rotation from fully unaligned position to fully aligned position.

It is worth noting that the possibility of increasing the number of turns was simulated too. 30 turns were added to SRM windings to use for augmenting the number of turns in case of faults, but the results showed that due to the very nonlinear characteristics of SRM, comparing decreasing and increasing the number of turns, decreasing the number of turns is much more effective in nullifying UMF. Thus here the focus is just on the control of decreasing the number of turns.

Considering Fig. 7, it is inferred that due to nonlinear features of SRM, by increasing the stator current in the range of 2.5A to 3A at the worst condition, UMF will be augmented merely 5 %, which is not any of importance. The simulation results for two degrees of eccentricities namely 30% and 70 % are analyzed.

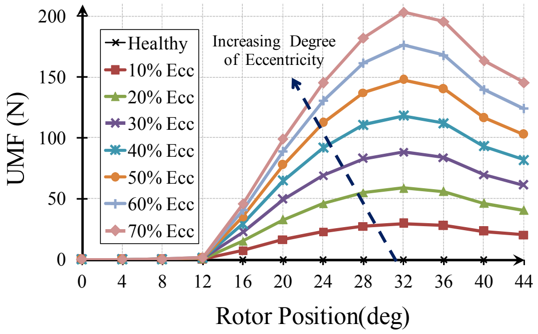

Fig. 6. UMF as a function of rotor position for different eccentricity degrees.

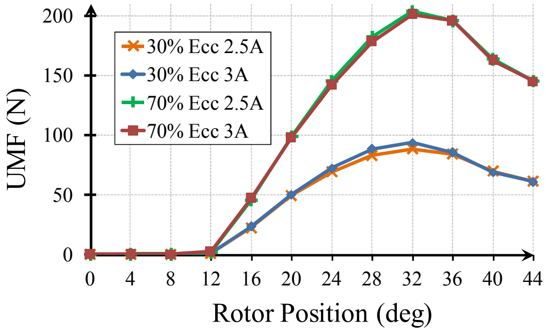

Fig. 7. Influence of increasing current on UMF.

A. 30% ECCENTRICITY

In case of 30 % eccentricity, the algorithm outcome is that the number of turns must be decreased to 75 turns (state 6) to mitigate UMF below UMF (10 %), and to keep torque at 90 % of its nominal value the current must be increased to 2.9A. UMF and torque, before and after compensation are plotted in Fig. 8 and 9. Considering Fig. 8, it is inferred that via this compensation strategy UMF at its peak value is reduced from 88 *N* to 21 *N*. It means more than 75% reduction in UMF. As it is evident the eccentricity effects are compensated completely (i.e., UMF is less than UMF (10 %)). According to Fig. 9 it is shown that via increasing the current intensity up to 2.9 A the torque is kept at 90 % of its value in healthy operation. At its peak value the torque has been decreased from 0.27 to 0.24 *Nm*. It is nearly a 10 % reduction, which is acceptable.

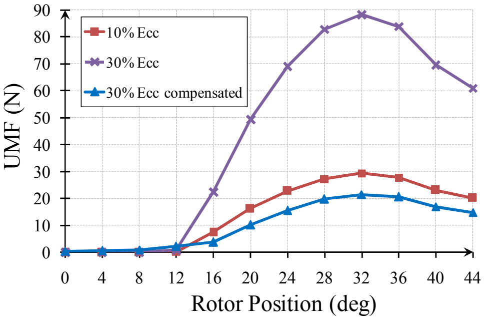

Fig. 8. UMF after implementation of the compensation strategy for 30 % fault.

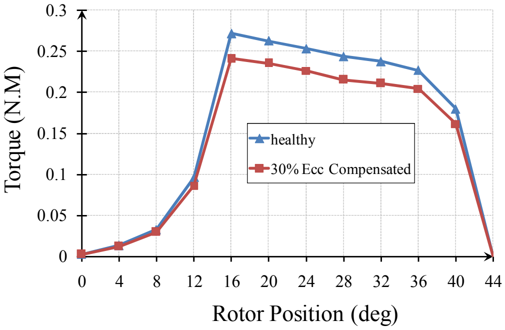

Fig. 9. Comparing torque for healthy condition and compensated 30 % eccentricity.

Fig. 10 (a) and (b) show the flux density in 30 % eccentricity before and after compensation, respectively. By examining this figure it is deduced that in the compensated motor as a result of the proposed method, flux density is balanced clearly in poles 1 and 2, which leads to a significant reduction in UMF. But it is worth noting that by increasing the source current, flux density is magnified less than 5 %, which is not concerning regarding to magnetic saturation.

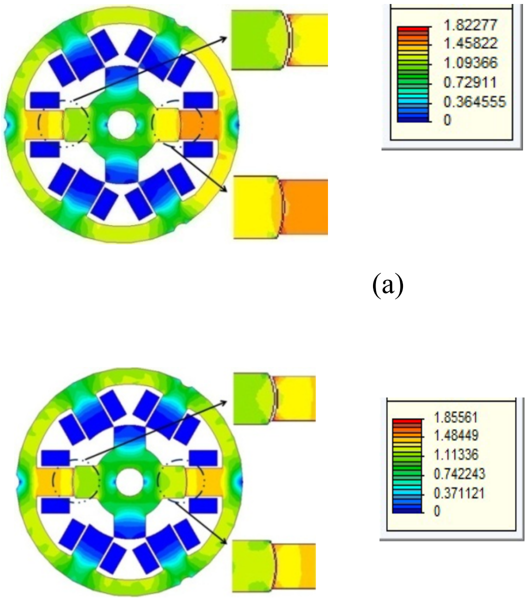

(a)

(b)

Fig. 10. Flux density in eccentric motor under 30% fault: a) before compensation and b) after compensation.

Fig. 11 (a) and (b) show the flux paths in 30% eccentricity before and after compensation in the aligned position, respectively. As it can be observed, after compensation flux leakages in adjacent poles are diminished significantly. In Fig. 12 the flux linkages for coils 1 and 2 in three conditions namely healthy motor, before and after compensation in 30 % eccentricity is shown. As it was predictable in healthy condition flux linkages for both coils are the same, of course with opposite direction. Under 30% eccentricity fault, the flux linkages are still nearly the same. It is reasonable that due to the very close flux linkages in coils 1 and 2, which have quite different air gaps the RFs will vary completely. By applying a compensation strategy the number of turns in coil 1 is not modified so its flux linkage will not alter so much but as its current is magnified it is augmented a little. But the scenario for coil 2 is totally different. As a result of 45 turns reduction in coil 2, the flux linkage must be decreased significantly, which can be seen clearly. As a result of this deduction, RF produced by coil 2 is mitigated so much, and somehow equalizes to RF produced by coil 1 and correspondingly UMF is nullified.

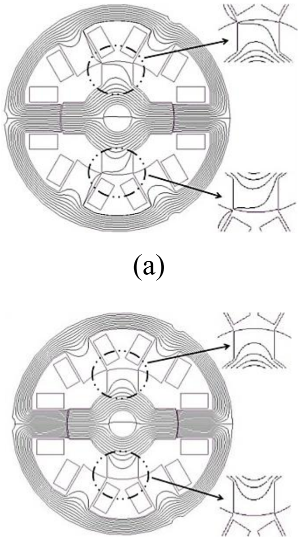

(a)

(b)

Fig. 11. Flux paths in eccentric motor under 30% fault: a) before compensation and b) after compensation.

B. 70% ECCENTRICITY

If the degree of eccentricity was more severe, suppose an extreme condition, a fault with 70% eccentricity has occurred. If the proposed strategy be applied to the given SRM, the outcome will be a reduction to 70 turns for turns number (state 7 in switching box) and an increase in current to 2.9 A. The results for UMF and torque in this compensated condition are shown in Figs. 13 and 14, respectively.

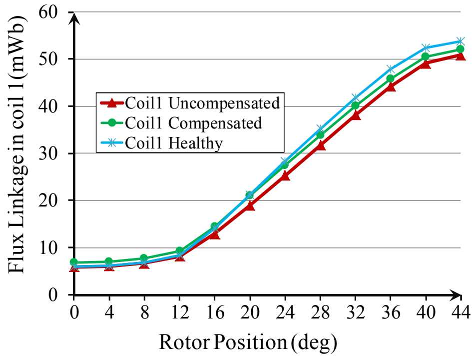

(a)

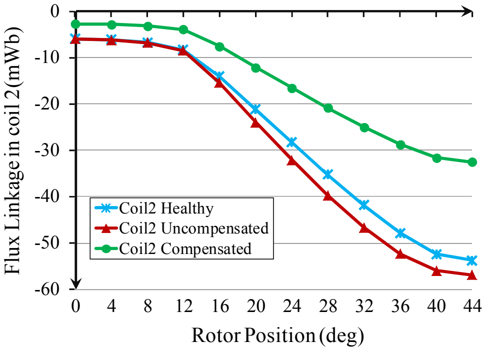

(b)

Fig. 12. Comparison between flux linkages in healthy motor, before and after compensation in case of 30 % eccentricity: a) coil 1 and b) coil 2.

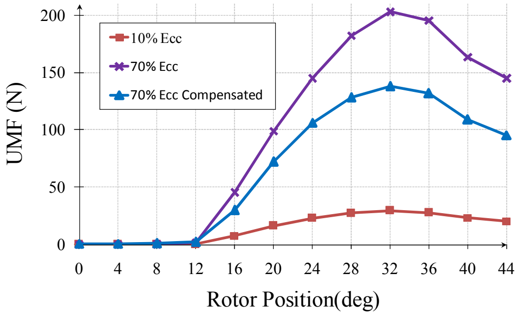

Fig. 13. UMF after implementation compensation strategy for 70 % fault.

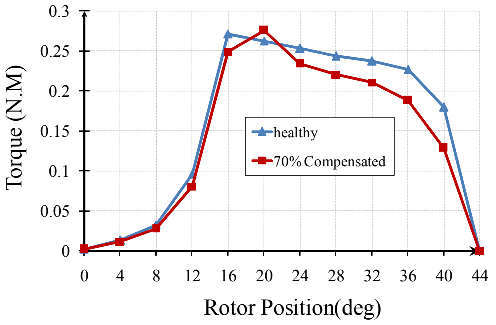

Fig. 14. Comparing torque for healthy condition and 70 % eccentricity compensated.

As it is seen in these figures despite employing the remedial strategy it is not possible to mitigate UMF below 10 % eccentricity level; however, it helps to lessen UMF at its peak value from 203 *N* to 137 *N*, which means more than 30 % reduction. In case of using the motor in critical operations this level of compensation might help the motor be able to continue its operation during the faults. Figure 14 shows the overall torque before and after compensation in case of 70 % eccentricity. One of the effects in eccentricities higher than 50 %, is the increase in overall torque which can be recognized here too. In this case the current is the same as in the case of 30 % eccentricity and also the number of turns is less than the previous case but the torque is kept around its level in healthy condition again. Figure 15 (a) and (b) shows the flux density in 70 % eccentricity before and after compensation, respectively. The explanations are similar to what was told for Fig. 16 (a) and (b) shows the flux paths in 70 % eccentricity before and after compensation, respectively. As it can be inferred, after compensation flux leakages in adjacent poles are diminished significantly, which leads to a more balanced flux distribution in the opposite poles which means reduction in UMF.

As it is inferred from the FEM results the proposed method by controlling the number of turns and stator current, has compensated the fault. In other words, applying the new strategy the RFs and motor torque are under control offering the possibility of operating even under fault condition.

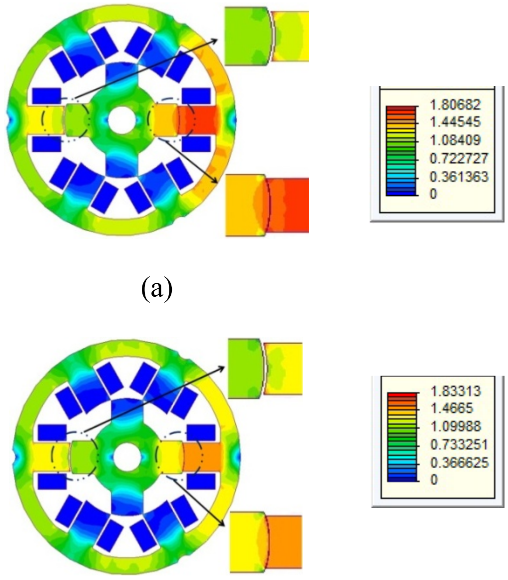

(a)

(b)

Fig. 15. Flux density in eccentric motor under 70% fault: a) before compensation and b) after compensation.

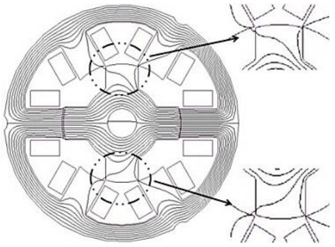

(a)

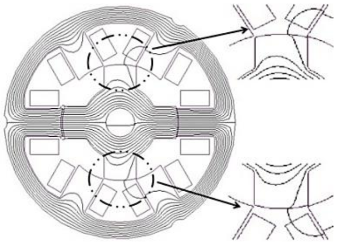

(b)

Fig. 16. Flux paths in eccentric motor under 70% fault: a) before compensation and b) after compensation.

VI. CONCLUSION

In this paper, a general method has been presented for compensating different degrees of eccentricity in SRMs. The proposed novel method is mathematically proven first and through FEM is simulated. It is found to be successful completely in compensating static eccentricities up to 40 % and mitigating the UMF up to 70 %. This strategy requires only one switching box to be able to decrease the number of turns (e.g. from 120 to 70 turns) and does not change winding structure. Thus, it is cost effective respect to changing fundamental structure of winding in motor assembly. Keeping the motor torque at its nominal value is accomplished via controlling the source current. Thereby, it can be claimed that the motor performance is not influenced at all. For instance; it is needed where the number of turns is decreased to 70 turns to nullify UMF the source current be increased from 2.5 A to 3 A to improve motor torque, which augments flux density around 5 % in 70 % eccentricity, which is not concerning. Simulations show that compensation strategy causes flux leakages in adjacent poles be diminished considerably.

ACKNOWLEDGMENT

This work was supported by vice-presidency of research and technology of Shahid Beheshti University.

REFERENCES

[1] C. Moron, A. Garcia, E. Tremps, and J. A. Somolinos, “Torque control of switched reluctance motors,” *IEEE Transactions on Magnetics,* vol. 48, no. 4, pp. 1661-1664, 2012.

[2] H. Torkaman, E. Afjei, and M. S. Toulabi, “New double-layer-per-phase isolated switched reluctance motor: concept, numerical analysis, and experimental confirmation,” *IEEE Transactions on Industrial Electronics,* vol. 59, no. 2, pp. 830-838, 2012.

[3] H. Torkaman, E. Afjei, A. Gorgani, N. Faraji, H. Karim, and N. Arbab, “External rotor SRM with high torque per volume: design, analysis, and experiments,” *Electrical Engineering, Springer*, pp. 1-9, 2012. DOI.10.1007/s00202-012-0265-3.

[4] N. K. Sheth and K. R. Rajagopal, “Variations in overall developed torque of a switched reluctance motor with airgap nonuniformity,” *IEEE Transactions on Magnetics,* vol. 41, no. 10, pp. 3973-3975, 2005.

[5] H. Torkaman and E. Afjei, “Comprehensive detection of eccentricity fault in switched reluctance machines using high frequency pulse injection,” *IEEE Transactions on Power Electronics,* vol. 28, no. 3, pp. 1382-1390, 2013.

[6] H. Torkaman, E. Afjei, and P. Yadegari, “Static, dynamic, and mixed eccentricity faults diagnosis in switched reluctance motors using transient finite element method and experiments,” *IEEE Transactions on Magnetics,* vol. 48, no. 8, pp. 2254-2264, 2012.

[7] E. Afjei and H. Torkaman, “Finite element analysis of SRG under fault condition oriented towards diagnosis of eccentricity fault,” *Applied Computational Electromagnetics Society (ACES) Journal,* vol. 26, no. 1, pp. 8-16, 2011.

[8] B. Fahimi, J. P. Johnson, and M. Ehsani, “Artificial intelligence approach to controlling SRM drives with manufacturing imperfections,” *IEEE Conference on Emerging Technologies and Factory Automation, EFTA*, pp. 623-628, 1996.

[9] J. Jinghua, S. Yukun, Z. Wenxiang, Z. Xiaoyong, and S. Chunxia, “Calculation and remedial strategy of radial force of switched reluctance motors with eccentricity,” *International Conference on Electrical Machines and Systems, ICEMS*, China, pp. 3932-3935, 2008.

[10] J. Li, D. Choi and Y. Cho, “Analysis of rotor eccentricity in switched reluctance motor with

parallel winding using FEM," *IEEE Transactions on Magnetics,* vol. 45, no. 6, pp. 2851-2854, 2009.

[11] T. J. E. Miller, "Faults and unbalanced forces in the switched reluctance machine," *IEEE Transactions on Industry Applications,* vol. 31, pp. 319-328, Mar./Apr., 1995.

[12] A. Burakov and A. Arkkio, "Comparison of the unbalanced magnetic pull mitigation by the parallel paths in the stator and rotor windings," *IEEE Transactions on Magnetics,* vol. 43, no. 12, pp. 4083-4088, 2007.

[13] M. Wallin, M. Ranlof, and U. Lundin, "Reduction of unbalanced magnetic pull in synchronous machines due to parallel circuits," *IEEE Transactions on Magnetics,* vol. 47, no. 12, pp. 4827-4833, 2011.

[14] H. Torkaman and E. Afjei, "Comprehensive magnetic field-based study on effects of static rotor eccentricity in switched reluctance motor parameters utilizing three-dimensional finite element," *Electromagnetics, Taylor and Francis,* vol. 29, no. 5, pp. 421- 433, 2009.

[15] H. Torkaman and E. Afjei, "Magnetostatic field analysis regarding the effects of dynamic eccentricity in switched reluctance motor," *Progress in Electromagnetics Research M, PIER,* vol. 8, pp. 163-180, 2009.

[16] H. Torkaman and E. Afjei, "Magnetostatic field analysis and diagnosis of mixed eccentricity fault in switched reluctance motor," *Electromagnetics, Taylor and Francis,* vol. 31, no. 5, pp. 368-383, 2011.

[17] H. Torkaman, E. Afjei, R. Ravaud, and G. Lemarquand, "Misalignment fault analysis and diagnosis in switched reluctance motor," *International Journal of Applied Electromagnetics and Mechanics,* vol. 36, no. 3, pp. 253-265, 2011.

[18] L. Qaseer, F. de León, and S. Purushothaman, "Combined field and circuit theories in squirrel-cage induction motors based on micro-T circuit model," *Applied Computational Electromagnetics Society (ACES) Journal,* vol. 26, no. 7, pp. 551-560, 2011.

[19] A. Sarikhani and O. A. Mohammed, "Coupled electromagnetic field computation with external circuit for the evaluation the performance of electric motor designs," *Applied Computational Electromagnetics Society (ACES) Journal,* vol. 26, no. 12, pp. 997-1006, 2011.

[20] J. H. Alwash and L. J. Qaseer, "Three-dimension finite element analysis of a helical motion induction motor," *Applied Computational Electromagnetics Society (ACES) Journal,* vol. 25, no. 8, pp. 703-712, 2010.

[21] S. Savin, S. Ait-Amar, D. Roger, and G. Vélu, "Prospective method for partial discharge detection in large AC machines using magnetic sensors in low electric field zones," *Applied Computational Electromagnetics Society (ACES) Journal,* vol. 26, no. 9, pp. 729-736, 2011.

[22] I. Husain, A. Radun, and J. Nairus, "Unbalanced force calculation in switched-reluctance machines," *IEEE Transactions on Magnetics,* vol. 36, no. 1, pp. 330-338, 2000.

[23] H. Torkaman, N. Arbab, H. Karim, and E. Afjei, "Fundamental and magnetic force analysis of an external rotor switched reluctance motor," *Applied Computational Electromagnetics Society (ACES) Journal,* vol. 26, no. 10, pp. 868-875, 2011.

[24] H. Torkaman and E. Afjei, "Sensorless method for eccentricity fault monitoring and diagnosis in switched reluctance machines based on stator voltage signature," *IEEE Transactions on Magnetics,* vol. 49, 2013, DOI:10.1109 / TMAG.2012.2213606.

2012 INSTITUTIONAL MEMBERS

DTIC-OCP LIBRARY
8725 John J. Kingman Rd, Ste 0944
Fort Belvoir, VA 22060-6218

AUSTRALIAN DEFENCE LIBRARY
Northcott Drive
Canberra, A.C.T. 2600 Australia

BEIJING BOOK CO, INC
701 E Linden Avenue
Linden, NJ 07036-2495

DARTMOUTH COLLEGE
6025 Baker/Berry Library
Hanover, NH 03755-3560

DSTO EDINBURGH
AU/33851-AP, PO Box 830470
Birmingham, AL 35283

SIMEON J. EARL – BAE SYSTEMS
W432A, Warton Aerodome
Preston, Lancs., UK PR4 1AX

ENGINEERING INFORMATION, INC
PO Box 543
Amsterdam, Netherlands 1000 Am

ETSE TELECOMUNICACION
Biblioteca, Campus Lagoas
Vigo, 36200 Spain

GA INSTITUTE OF TECHNOLOGY
EBS-Lib Mail code 0900
74 Cherry Street
Atlanta, GA 30332

TIMOTHY HOLZHEIMER
Raytheon
PO Box 1044
Rockwall, TX 75087

HRL LABS, RESEARCH LIBRARY
3011 Malibu Canyon
Malibu, CA 90265

IEE INSPEC
Michael Faraday House
6 Hills Way
Stevenage, Herts UK SG1 2AY

INSTITUTE FOR SCIENTIFIC INFO.
Publication Processing Dept.
3501 Market St.
Philadelphia, PA 19104-3302

LIBRARY – DRDC OTTAWA
3701 Carling Avenue
Ottawa, Ontario, Canada K1A OZ4

LIBRARY of CONGRESS
Reg. Of Copyrights
Attn: 407 Deposits
Washington DC, 20559

LINDA HALL LIBRARY
5109 Cherry Street
Kansas City, MO 64110-2498

MISSOURI S&T
400 W 14th Street
Rolla, MO 56409

MIT LINCOLN LABORATORY
Periodicals Library
244 Wood Street
Lexington, MA 02420

NATIONAL CHI NAN UNIVERSITY
Lily Journal & Book Co, Ltd
20920 Glenbrook Drive
Walnut, CA 91789-3809

JOHN NORGARD
UCCS
20340 Pine Shadow Drive
Colorado Springs, CO 80908

OSAMA MOHAMMED
Florida International University
10555 W Flagler Street
Miami, FL 33174

NAVAL POSTGRADUATE SCHOOL
Attn:J. Rozdal/411 Dyer Rd./ Rm 111
Monterey, CA 93943-5101

NDL KAGAKU
C/0 KWE-ACCESS
PO Box 300613 (JFK A/P)
Jamaica, NY 11430-0613

OVIEDO LIBRARY
PO BOX 830679
Birmingham, AL 35283

DAVID PAULSEN
E3Compliance
1523 North Joe Wilson Road
Cedr Hill, TX 75104-1437

PENN STATE UNIVERSITY
126 Paterno Library
University Park, PA 16802-1808

DAVID J. PINION
1122 E Pike Street #1217
SEATTLE, WA 98122

KATHERINE SIAKAVARA
Gymnasiou 8
Thessaloniki, Greece 55236

SWETS INFORMATION SERVICES
160 Ninth Avenue, Suite A
Runnemede, NJ 08078

YUTAKA TANGE
Maizuru Natl College of Technology
234 Shiroya
Maizuru, Kyoto, Japan 625-8511

TIB & UNIV. BIB. HANNOVER
DE/5100/G1/0001
Welfengarten 1B
Hannover, Germany 30167

UEKAE
PO Box 830470
Birmingham, AL 35283

UNIV OF CENTRAL FLORIDA
4000 Central Florida Boulevard
Orlando, FL 32816-8005

UNIVERSITY OF COLORADO
1720 Pleasant Street, 184 UCB
Boulder, CO 80309-0184

UNIVERSITY OF KANSAS – WATSON
1425 Jayhawk Blvd 210S
Lawrence, KS 66045-7594

UNIVERSITY OF MISSISSIPPI
JD Williams Library
University, MS 38677-1848

UNIVERSITY LIBRARY/HKUST
Clear Water Bay Road
Kowloon, Honk Kong

CHUAN CHENG WANG
8F, No. 31, Lane 546
MingCheng 2nd Road, Zuoying Dist
Kaoshiung City, Taiwan 813

THOMAS WEILAND
TU Darmstadt
Schlossgartenstrasse 8
Darmstadt, Hessen, Germany 64289

STEVEN WEISS
US Army Research Lab
2800 Powder Mill Road
Adelphi, MD 20783

YOSHIHIDE YAMADA
NATIONAL DEFENSE ACADEMY
1-10-20 Hashirimizu
Yokosuka, Kanagawa,
Japan 239-8686

APPLIED COMPUTATIONAL ELECTROMAGNETICS SOCIETY JOURNAL
http://aces.ee.olemiss.edu

INFORMATION FOR AUTHORS

PUBLICATION CRITERIA

Each paper is required to manifest some relation to applied computational electromagnetics. **Papers may address general issues in applied computational electromagnetics, or they may focus on specific applications, techniques, codes, or computational issues.** While the following list is not exhaustive, each paper will generally relate to at least one of these areas:

1. **Code validation.** This is done using internal checks or experimental, analytical or other computational data. Measured data of potential utility to code validation efforts will also be considered for publication.

2. **Code performance analysis.** This usually involves identification of numerical accuracy or other limitations, solution convergence, numerical and physical modeling error, and parameter tradeoffs. However, it is also permissible to address issues such as ease-of-use, set-up time, run time, special outputs, or other special features.

3. **Computational studies of basic physics.** This involves using a code, algorithm, or computational technique to simulate reality in such a way that better, or new physical insight or understanding, is achieved.

4. **New computational techniques** or new applications for existing computational techniques or codes.

5. **“Tricks of the trade”** in selecting and applying codes and techniques.

6. **New codes, algorithms, code enhancement, and code fixes.** This category is self-explanatory, but includes significant changes to existing codes, such as applicability extensions, algorithm optimization, problem correction, limitation removal, or other performance improvement. **Note: Code (or algorithm) capability descriptions are not acceptable, unless they contain sufficient technical material to justify consideration.**

7. **Code input/output issues.** This normally involves innovations in input (such as input geometry standardization, automatic mesh generation, or computer-aided design) or in output (whether it be tabular, graphical, statistical, Fourier-transformed, or otherwise signal-processed). Material dealing with input/output database management, output interpretation, or other input/output issues will also be considered for publication.

8. **Computer hardware issues.** This is the category for analysis of hardware capabilities and limitations of various types of electromagnetics computational requirements. Vector and parallel computational techniques and implementation are of particular interest.

Applications of interest include, but are not limited to, antennas (and their electromagnetic environments), networks, static fields, radar cross section, inverse scattering, shielding, radiation hazards, biological effects, biomedical applications, electromagnetic pulse (EMP), electromagnetic interference (EMI), electromagnetic compatibility (EMC), power transmission, charge transport, dielectric, magnetic and nonlinear materials, microwave components, MEMS, RFID, and MMIC technologies, remote sensing and geometrical and physical optics, radar and communications systems, sensors, fiber optics, plasmas, particle accelerators, generators and motors, electromagnetic wave propagation, non-destructive evaluation, eddy currents, and inverse scattering.

Techniques of interest include but not limited to frequency-domain and time-domain techniques, integral equation and differential equation techniques, diffraction theories, physical and geometrical optics, method of moments, finite differences and finite element techniques, transmission line method, modal expansions, perturbation methods, and hybrid methods.

Where possible and appropriate, authors are required to provide statements of quantitative accuracy for measured and/or computed data. This issue is discussed in “Accuracy & Publication: Requiring, quantitative accuracy statements to accompany data,” by E. K. Miller, *ACES Newsletter,* Vol. 9, No. 3, pp. 23-29, 1994, ISBN 1056-9170.

SUBMITTAL PROCEDURE

All submissions should be uploaded to ACES server through ACES web site (http://aces.ee.olemiss.edu) by using the upload button, journal section. Only pdf files are accepted for submission. The file size should not be larger than 5MB, otherwise permission from the Editor-in-Chief should be obtained first. Automated acknowledgment of the electronic submission, after the upload process is successfully completed, will be sent to the corresponding author only. It is the responsibility of the corresponding author to keep the remaining authors, if applicable, informed. Email submission is not accepted and will not be processed.

EDITORIAL REVIEW

In order to ensure an appropriate level of quality control, papers are peer reviewed. They are reviewed both for technical correctness and for adherence to the listed guidelines regarding information content and format.

PAPER FORMAT

Only camera-ready electronic files are accepted for publication. The term **“camera-ready” means that the material is neat, legible, reproducible, and in accordance with the final version format listed below.**

The following requirements are in effect for the final version of an ACES Journal paper:

1. The paper title should not be placed on a separate page.

The title, author(s), abstract, and (space permitting) beginning of the paper itself should all be on the first page. The title, author(s), and author affiliations should be centered (center-justified) on the first page. The title should be of font size 16 and bolded, the author names should be of font size 12 and bolded, and the author affiliation should be of font size 12 (regular font, neither italic nor bolded).

2. An abstract is required. The abstract should be a brief summary of the work described in the paper. It should state the computer codes, computational techniques, and applications discussed in the paper (as applicable) and should otherwise be usable by technical abstracting and indexing services. The word “Abstract” has to be placed at the left margin of the paper, and should be bolded and italic. It also should be followed by a hyphen (—) with the main text of the abstract starting on the same line.

3. All section titles have to be centered and all the title letters should be written in caps. The section titles need to be numbered using roman numbering (I. II. ….)

4. Either British English or American English spellings may be used, provided that each word is spelled consistently throughout the paper.

5. Internal consistency of references format should be maintained. As a guideline for authors, we recommend that references be given using numerical numbering in the body of the paper (with numerical listing of all references at the end of the paper). The first letter of the authors’ first name should be listed followed by a period, which in turn, followed by the authors’ complete last name. Use a coma (,) to separate between the authors’ names. Titles of papers or articles should be in quotation marks (“ ”), followed by the title of journal, which should be in italic font. The journal volume (vol.), issue number (no.), page numbering (pp.), month and year of publication should come after the journal title in the sequence listed here.

6. Internal consistency shall also be maintained for other elements of style, such as equation numbering. Equation numbers should be placed in parentheses at the right column margin. All symbols in any equation have to be defined before the equation appears or right immediately following the equation.

7. The use of SI units is strongly encouraged. English units may be used as secondary units (in parentheses).

8. Figures and tables should be formatted appropriately (centered within the column, side-by-side, etc.) on the page such that the presented data appears close to and after it is being referenced in the text. When including figures and tables, all care should be taken so that they will appear appropriately when printed in black and white. For better visibility of paper on computer screen, it is good to make color figures with different line styles for figures with multiple curves. Colors should also be tested to insure their ability to be distinguished after black and white printing. Avoid the use of large symbols with curves in a figure. It is always better to use different line styles such as solid, dotted, dashed, etc.

9. A figure caption should be located directly beneath the corresponding figure, and should be fully justified.

10. The intent and meaning of all text must be clear. For authors who are not masters of the English language, the ACES Editorial Staff will provide assistance with grammar (subject to clarity of intent and meaning). However, this may delay the scheduled publication date.

11. Unused space should be minimized. Sections and subsections should not normally begin on a new page.

ACES reserves the right to edit any uploaded material, however, this is not generally done. It is the author(s) responsibility to provide acceptable camera-ready files in pdf and MSWord formats. Incompatible or incomplete files will not be processed for publication, and authors will be requested to re-upload a revised acceptable version.

COPYRIGHTS AND RELEASES

Each primary author must execute the online copyright form and obtain a release from his/her organization vesting the copyright with ACES. Both the author(s) and affiliated organization(s) are allowed to use the copyrighted material freely for their own private purposes.

Permission is granted to quote short passages and reproduce figures and tables from and ACES Journal issue provided the source is cited. Copies of ACES Journal articles may be made in accordance with usage permitted by Sections 107 or 108 of the U.S. Copyright Law. This consent does not extend to other kinds of copying, such as for general distribution, for advertising or promotional purposes, for creating new collective works, or for resale. The reproduction of multiple copies and the use of articles or extracts for commercial purposes require the consent of the author and specific permission from ACES. Institutional members are allowed to copy any ACES Journal issue for their internal distribution only.

PUBLICATION CHARGES

All authors are allowed for 8 printed pages per paper without charge. Mandatory page charges of $75 a page apply to all pages in excess of 8 printed pages. Authors are entitled to one, free of charge, copy of the printed journal issue in which their paper was published. Additional reprints are available for $ 50. Requests for additional re-prints should be submitted to the managing editor or ACES Secretary.

Corresponding author is required to complete the online form for the over page charge payment right after the initial acceptance of the paper is conveyed to the corresponding author by email.

ACES Journal is abstracted in INSPEC, in Engineering Index, DTIC, Science Citation Index Expanded, the Research Alert, and to Current Contents/Engineering, Computing & Technology.